Copyright

by

Janice Adona Trinidad

2007

The Dissertation Committee for Janice Adona Trinidad
certifies that this is the approved version of the following dissertation:

Electrical Transport through One-Dimensional Metallic Nanoparticle Arrays

Committee:

Allan H. MacDonald, Supervisor

Chih-Kang Shih

Roger T. Bonnecaze

Zhen Yao

Brian A. Korgel

Electrical Transport through One-Dimensional Metallic Nanoparticle Arrays

by

Janice Adona Trinidad, B.S. Physics

Dissertation

Presented to the Faculty of the Graduate School of
The University of Texas at Austin
in Partial Fulfillment
of the Requirements
for the Degree of

Doctor of Philosophy

The University of Texas at Austin

August 2007

Acknowledgments

I have many people to thank for their direct and indirect support of the completion of this work.

I thank Dr. Allan Macdonald for being a very patient and enthusiastic advise. I am grateful that Allan inspired me by frequently asking me good questions. When I am tempted to only teach by telling in my next career, I will think of Allan to remind myself of better ways.

I thank Dr. Elena (Leni) Bascones for countless conversations and for research support throughout the course of this project. This project could not have been completed without her support. I am very lucky to have worked with someone who conducts research and lives life with amazing daring and exuberance.

I thank Dr. Samuel Wehrli for sharing his multipolar algorithm with me and Leni so we could overcome a technical challenge in our research. His ideas enabled us to calculate the full inverse capacitance matrices of systems of spheres that reasonably approximate the geometries of experimentally realized nanoparticle arrays.

I thank the members of the Physics Department staff, especially Becky Drake, Carol Noriega, and Dr. Udagawa for assisting me with signing up for coursework, planning meetings, and submitting all the paper work that enabled me to make it to this point.

I thank the members of my committee, Dr. Shih, Dr. Bonnecaze, Dr. Korgel,

and Dr. Yao for their patience and support.

I thank all the people from the UTeach department for helping me to embrace and achieve my dream of teaching high school science. Many thanks to Dr. Marder, Dr. Walker, Dr. Marshall, Dr. Lustig, Dr. Dickenson, Denise Eckberg, Pamela Powell, Pamela Quackenbush, Jane Mifsud, Stephanie Hart, and many others.

Finally, I thank my family: my mom, my dad, my two sisters, Jennilee and Janelle, and Summer Cacciotti for being my biggest fans throughout this process.

JANICE ADONA TRINIDAD

The University of Texas at Austin
August 2007

Electrical Transport through One-Dimensional Metallic Nanoparticle Arrays

Publication No. ____________________

Janice Adona Trinidad, Ph.D.
The University of Texas at Austin, 2007

Supervisor: Allan H. MacDonald

We analyzed the effects of long-range interactions and disorder on the transport properties of one-dimensional nanoparticle arrays. We described the Coulomb interactions using an inverse capacitance matrix which we computed to include the screening due to the nanoparticles and the leads. We calculated the threshold voltage and the current and we investigated how temperature and variations in the junction resistances affect these transport characteristics. We demonstrate that there are at least two linear regimes, at voltages close to threshold and at high voltages, with different slopes. We show that the low voltage linear regime persists over a very small range of voltages, probably too small to be relevant for experiments, and that the threshold voltage depends on how symmetrically the array is biased. At high voltage the linear conductance depends only on the resistances of the junctions and the current has an asymptotic offset voltage that depends on the charging energies of the nanoparticles.

Contents

Acknowledgments **iv**

Abstract **vi**

List of Tables **xi**

List of Figures **xiv**

Chapter 1 Introduction **1**

1.1 Metallic Nanoparticle Arrays: Tunable Quantum Solids 1

1.2 Orthodox Model of Single Charge Tunneling 6

1.3 Overview of our approach and the organization of this thesis 12

Chapter 2 Models of Electron Transport in Metallic Nanoparticle Arrays **15**

2.1 Background 15

2.1.1 Models of Electrostatic Interactions 15

2.1.2 Models of Disorder 21

2.2 Our Transport Model 26

2.2.1 Our Model for the Coulomb Interactions of 1-D Nanoparticle Arrays 26

2.2.2 Our Model for Disorder 33

2.3 Conclusions 39

Chapter 3 Threshold Voltage of 1-D Nanoparticle Arrays 42

3.1 Background 43

3.1.1 Zero Temperature Threshold 43

3.1.2 Finite Temperature Threshold 45

3.2 Zero Temperature Threshold Results 48

3.2.1 Clean Arrays with Onsite Interactions 48

3.2.2 Clean Arrays with Long Range Interactions 54

3.2.3 Disordered Arrays with Onsite Interactions 60

3.2.4 Disordered Arrays with Long Range Interactions 61

3.3 Static Potentials of Disordered Arrays 69

3.4 Finite Temperature Threshold 76

3.5 Conclusions 81

Chapter 4 Low Temperature Transport Characteristics 85

4.1 Background 86

4.2 Bottleneck Regime 87

4.2.1 Bottleneck regime for arrays with long range interactions . . 92

4.2.2 Bottleneck regime for arrays with onsite interactions 95

4.3 Linear Resistance regime 99

4.4 Intermediate regime 105

4.5 Conclusions 111

Chapter 5 Summary and Outlook 114

5.1 Summary 114

5.1.1 Models of Nanoparticle Arrays 114

5.1.2 Thresholds of Nanoparticle Arrays 115

5.1.3 Dynamics of Nanoparticle Arrays 119

5.2 Future Work 121

Chapter 6 Appendix **123**

6.1 Monte Carlo Simulations of Transport in Nanoparticle Arrays 123

6.2 Methods to Calculate the Inverse Capacitance Matrix 126

6.2.1 Image Charges Method 126

6.2.2 High-order multipoles method 128

6.3 Methods for Calculating Probability Distributions 132

Bibliography **134**

Vita **140**

List of Tables

2.1 *Comparison of our distributions,* $P(\Phi_i^{dis})$*, for 50-island arrays with the equivalent 1-D distributions in [17].* E_i^{e-h} and $P(0)$ were given by the distributions in Fig. 2.4. Φ_{max}^{dis} and $P(0)_{\text{1-D}}$ were calculated using expressions from [17]: Eq. 2.3 and Eq. 2.1.2 with $\gamma \equiv C_{24,24}^{-1}/C_{24,25}^{-1}$. γ equals 0 for onsite arrays and 0.08329 and 0.41206 for arrays with d/r^{isl} equal to 10 and 0.5 respectively. Although the expression used to calculate $P(0)_{\text{1-D}}$ is valid only for $\gamma < 1/3$, our numerical results, $P(0)$, were in reasonable agreement with $P(0)_{\text{1-D}}$ for all cases. The widths of our distributions (E^{e-h}) decrease at a slightly faster rate than Φ_{max}^{dis} as the spacing decreased. 39

3.1 *Estimates of thresholds predicted by Likharev, et al. [32] for arrays with no disorder.* These values were calculated using $V_S = 2V_T$ where V_T is given by Eq. 3.1.1 with $C_{eff}^{-1} \approx C_{25,25}^{-1}$ and M extracted from rows of our inverse capacitance matrices that correspond to islands in the middle of long arrays. See Fig. 3.5. Likharev, et al. predicted that symmetrically biased arrays without disorder would have thresholds that are independent of N given by V_S when $N > 2M$. Although the arrays in Fig. 3.4 are long enough that $N > 2M$, the thresholds continue to increase with N and are larger than the values tabulated here. Qualitatively, our results agree because the thresholds eventually saturate at large enough N to values that like V_S increase with decreasing spacing. 57

3.2 *Comparison of slopes of $\langle V_T(N)/E_c^{isl}\rangle$ for disordered arrays at several spacings, $d/r^{isl} = 10, 1, 0.5$.* The numerical slopes are the slopes of the linear fits to our numerical results in Fig. 3.8. $\langle E^{e-h}/2\rangle$ is from an estimate, Eq. 3.13, for the threshold that approximates the energy to overcome junctions with $\Phi_i^{dis} \geq 0$ as E_i^{e-h}. $C_{25,25}^{-1}$ is from the estimate made by Elteto, et al. to extend the MW onsite threshold to include interactions among neighboring nanoparticles, Eq. 3.1.2. α^{MW} was the form predicted by Middleton and Wingreen (1993) [35] in the limit of large soliton lengths. Fig. 3.5 shows how the soliton lengths, M, were extracted from our inverse capacitance matrices. M^{-2} is greater than the maximum value for $\alpha^{MW} = 1$ (in units of $E_c^{isl} = 0.5eC_0^{-1}$) at all the spacings. At all spacings, the soliton lengths are too short for the large M estimates to be valid and too long to be described by the onsite value, $\alpha^{MW} = 1$. 66

4.1 *Scaling exponents measured on 1-D and quasi-1-D arrays.* The reduced voltage is related to the applied voltage, V, and the threshold voltage, V_T, by $v = (V - V_T)/V_T$. Rimberg, et al.'s arrays consist of Al islands linked by Al/$\mathrm{Al}_x O_y/Al$ junction produced by e-beam lithography [42]. Bezryadin, et al.'s arrays consist of 1-D chains of carbon nanoparticles that are occasionally broken up by 2-D clusters of nanoparticles [4]. See Fig. 1.2(b). Elteto, et al.'s arrays are composed of gold nanoparticles that are approximately 60 nanoparticles long and 4 nanoparticles wide [18]. Jha & Middleton (2005) obtained their results numerically. DC (UC) correspond to arrays with random capacitance (uniform capacitances). 88

4.2 *Approximate sizes of voltage ranges near threshold with linear scaling.* Linear scaling appears for $\tilde{V} = V - V_T < \tilde{V}_{max}$ (in units of E_c^{isl}) or for $v = \tilde{V}/V_T < v_{max}$ (in units of reduced voltage). Linear scaling disappears at voltages smaller than the voltage ranges used to measure the scaling exponents in Table 4.1. 88

4.3 *Approximate minimum voltages for the linear resistance regimes of 50-island arrays with varied interaction strengths.* $v_{min,1}$ and $v_{min,2}$ are the reduced voltages, $v = (V - V_T)/V_T$, associated with $2V^0$ and $8V^0$. These values approximate the minimum voltages required to reach the linear resistance regime for arrays with equal resistances and for arrays with equal resistances except for one large resistance in the middle of the array. 111

List of Figures

1.1 Disordered and ordered 2-D arrays from [39] and [36]. (a) Disordered array with regions missing particles (voids) and with double layers (darkened regions). The mean spacing between the nanoparticles in the monolayer regions is $s = 0.85 \pm 0.1$ nm. (b) Ordered array with particle spacing, $s = 1.2 \pm 0.1$ nm. In (a) and (b), the mean radii of the nanoparticles varied between 2.2 nm to 2.9 nm from sample to sample. 4

1.2 *One-dimensional (1-D) and quasi-1-D nanoparticle arrays.* (a) A quasi-1-D array from [18] composed of 5.5 nm gold nanoparticles with 5-7% dispersity spaced 1.3 nm apart on average. The array spans a 30 nm gap between two planar Cr electrodes. (b) A chain of graphitized carbon nanoparticles with diameter, $d \approx 30$ nm, from [4]. The chain of length, $L \approx 1.2\mu$m, connects two Cr electrodes. (c) A 1-D array of 13 gold grains of mean radius, $r \approx 3nm$, between two electrodes from [8]. 6

1.3 1-D arrays of N spheres of radii, r_{isl}, sandwiched between two large spherical leads of radii, R_{lead} (not drawn to scale). 12

2.1 *Effective circuit model for 1-D nanoparticle array* C and C_0 are the mutual capacitance between nearest neighboring islands and the self-capacitance of the islands. islands. C_h is an infinite periodic network of capacitors. The effective capacitance of the network in Fig. 2.1(a) equals $C_{eff} = C_0 + 2C_h$. The periodic symmetry of C_h can be used to show that $C_h^{-1} = C^{-1} + (C_0 + C_h)^{-1}$. See Fig. 2.1(b). This figure is modeled after figures in [32] and [10]. 19

2.2 *Polarization potential differences,* Φ_i^{pol}*, across 1-D arrays with 50 islands.* In the top panel, the applied potentials at the source and drain leads equals $V_0 = -V_{N+1} = V/2$. In the bottom panel, the drain is grounded while the source lead potential equals $V_0 = V$. Both panels have the same applied bias difference, $V = V_0 - V_{N+1}$ and each show how modifying the spacing between sites changes how Φ_i^{pol} is distributed over the junctions. 31

2.3 *Elements of* $C_{i,j}^{-1}$ *and* $\tilde{C}_{i,j}^{-1}$ *for 50-island arrays at two spacings,* $d/r^{isl} = 10$ *and 0.5.* In both panels, C_0^{-1} is the self inverse capacitance of an isolated island; $C_{i,i}^{-1} = C_0^{-1}$ when interactions among sites are negligible. The top panel plots the rows of C^{-1} and $\tilde{C}^{-1}$ that correspond to the island closest to the source lead. The bottom panel plots the rows that correspond to the islands in the middle of array. The solid lines show C^{-1} and the symbols denote the modified inverse capacitance elements. $\tilde{C}^{-1}$ differs from C^{-1} because it includes the potentials due to induced charges on the leads. These induced charges introduce more screening such that $\tilde{C}_{i,j}^{-1} < C_{i,j}^{-1}$. These differences are small and most noticeable in terms that describe interactions among charges close to the leads. 32

2.4 Probability distributions of disorder potentials ϕ^{dis}, (a), and disorder potential differences Φ^{dis}, (b), due to disorder for 50-island arrays with purely onsite coupling and with long range Coulomb coupling at two spacings. $d/r^{isl} = 0.5$ and 10. Vertical lines are included as guidelines to emphasize the edges of the distributions. All potentials are displayed in units of $E_c^{isl} = 1/(2C^0)$. 37

2.5 Comparison of $< \phi_{25}^{dis} \phi_k^{dis} >$ normalized by $|\phi_{25}^{dis}|^2$ for 50-island arrays with onsite (top plot) versus long range (bottom plot) Coulomb interactions. $C_{k,25}^{-1}$ normalized by $C_{25,25}^{-1}$ is included in the long range case to show that correlations in the disorder potentials are related to, but decay faster than the C^{-1} elements. 40

3.1 Potentials and charges at sites in two arrays of different length ($N = 5$ and $N = 6$) at voltages just above the threshold. The filled bars, unfilled bars with solid borders, and unfilled bars with dashed borders represent the polarization potential, the total potential, and the total potential plus the excitonic energy respectively. The last quantity equals the potential seen at a site by a charge tunneling to the right unto that site. The arrows indicate possible tunneling events. The tick marks are spaced $2E_c^{isl}$ units apart. The insets show the charge at each island for each set of potentials. Filled (unfilled) circles represent positive (negative) charges. 51

3.2 *Threshold voltage of arrays in the limit of onsite interactions as a function of the biasing asymmetry factor, α.* The open (closed) symbols correspond to the thresholds of arrays without (with) charged disorder. The V_S and V_D curves are examples of the family of curves described by Eq. 3.6 and Eq. 3.7 that make up the threshold relationships for arrays without disorder. . . . 53

3.3 *Threshold voltage of clean arrays with onsite interactions as a function of array length, N, for several values of the biasing asymmetry factor, α.* . . 54

3.4 Threshold of symmetrically biased arrays, V_T, with no disorder as a function of number of islands, N, and of array spacing, d/r^{isl}. The dashed lines are estimates of the threshold that use a r^{-1} model to approximate the polarization potential drops across the contact junctions, Λ_1 and Λ_{N+1}. . 57

3.5 $C^{-1}_{25,i}/C^{-1}_{25,25}$ *for 50-island arrays spaced at* $d/r^{isl} = 0.5, 1$ *and 10.* 58

3.6 *Threshold voltage of clean arrays with long range Coulomb interactions as a function of* α*.* 59

3.7 *Means and rms fluctuations of the thresholds of disordered arrays with onsite interactions.* 62

3.8 *Average threshold,* $\langle V_T \rangle$ *of disordered arrays versus array length,* N*, at three different array spacings,* $d/r^{isl} = 10, 1$ *and 0.5.* The inset displays the rms fluctuations, δV_T, of the threshold. The dashed line in each graph shows how $\langle V_T \rangle$ and δV_T depend on N in the limit of onsite interactions. 63

3.9 *Comparison of Zero Temperature Threshold Results.* The threshold results of Delsing, et al. (1990) et al., Bezryadin, et al. [4], Elteto, et al. [17] were rescaled by $E_c^{isl} = e/(2C_0)$ equal to 0.3 meV, 0.05 eV, and 0.26 eV respectively. The dashed lines represent our results for arrays at different spacings, $d/r^{isl} = 0.5, 1$, and 10. The Delsing, et al. results compare well with our results because they measure thresholds on 1-D arrays whereas Bezryadin, et al. and Elteto, et al. measured the thresholds of quasi-1-D arrays. 67

3.10 *Threshold,* V_T*, versus biasing asymmetry factor,* α*, for 50-island arrays at two different spacings,* $d/r^{isl} = 0.5$ *and 10, in the presence and absence of charged disorder.* 68

3.11 *Probability distributions of bulk junctions in the onsite limit for* $V < V_T$. The distributions denoted by solid (dashed) lines average over 1 (100) configuration(s) of disorder on 50-island arrays. From left to right, the graphs correspond to $V = (0, 0.5, 1)V_T$ where $V_T = 46.5E_c^{isl}$ is the threshold voltage of the array represented by the solid curves. The graphs in the top row correspond to arrays with junctions of equal resistance, $R_i = R_0$. The bottom row corresponds to arrays with the same total resistance as the top ($R^{tot} = 51R_0$) and all resistances equal except for one bulk junction with $R_k = 30R_0$. 71

3.12 The sum of the distributions due to bulk junctions with down-steps ($\Phi^{dis} < 0$) and up-steps ($\Phi^{dis} > 0$) leads to the form of $P(\Delta E_i)$ at the threshold voltage in the limit of onsite interactions. At this voltage, the probability distributions due to up-steps and down-steps at $V = 0$ are shifted by $-2E_c^{isl}$ and 0. 71

3.13 *Probability distributions of the bulk junctions for 50-islands arrays and spacing* $d/r^{isl} = 10$ *for* $V \leq V_T$. The distributions denoted by solid (dashed) lines average over 1 (100) configuration(s) of disorder. From left to right, the graphs correspond to $V = (0, 0.5, 1)V_T$ where $V_T \approx 36.55E_c^{isl}$ is the threshold voltage of the array represented by the solid curves. The arrays in the top row have equal resistances ($R = 1$ in Eq. 3.14). The arrays in the bottom row have one junction with a very large resistance ($R = 30$ in Eq. 3.14). All the arrays have the same total resistance $R^{tot} = 51R_0$. . . . 73

3.14 *Probability distributions of the bulk junctions for 50-islands arrays and spacing* $d/r^{isl} = 0.5$ *for* $V \leq V_T$. The distributions denoted by solid (dashed) lines average over 1 (100) configuration(s) of disorder. From left to right, the graphs correspond to $V = (0, 0.5, 1)V_T$ where $V_T \approx 16.69 E_c^{isl}$ is the threshold voltage of the array represented by the solid curves. The graphs in the top (bottom) row have resistances described by *Eq.* 3.14 and $R = 1$ ($R = 30$). 74

3.15 *Comparison of* $P(\Phi_i)$ *and* $P(\Delta E_i)$ *across junctions with up-steps* ($\Phi^{dis} \geq 0$) *at the threshold voltage.* The thin lines correspond to the distributions of 50-island arrays in the onsite limit. The thick lines in the top (bottom) row correspond to 50-island arrays with $d/r^{isl} = 10$ ($d/r^{isl} = 0.5$). 76

3.16 *Comparison of* $P(\Phi_i)$ *and* $P(\Delta E_i)$ *across junctions with down-steps* ($\Phi^{dis} < 0$) *at the threshold voltage.* The thin lines correspond to the distributions of 50-island arrays in the onsite limit. The thick lines in the top (bottom) row correspond to 50-island arrays with $d/r^{isl} = 10$ ($d/r^{isl} = 0.5$). 77

3.17 *IV curves and thresholds of a 50-island array with disorder at finite temperatures.* The finite temperature threshold occurs at the peak in the second derivative of each IV curves shown in the inset. 78

3.18 *Average finite temperature thresholds versus temperature for 50-island arrays with disorder and spacing, $d/r^{isl} = 0.5$.* The closed circles are the average thresholds of 15 arrays. The error bars have lengths equal to the rms fluctuations of the thresholds. Each threshold was determined by locating the peak in $\partial^2 I/\partial V^2$. See Fig. 3.17. The dotted line is the prediction made by Elteto, et al. [17]: $Vt(T)/Vt(T=0) = 1 - 4.8P(0)kT$ where $P(0) = 0.66(E_c^{isl})^{-1}$ for 50-island arrays with $d/r^{isl} = 0.5$ 79

3.19 *IV curves for a 5-island array without (a) and with (b) charged disorder at several temperatures.* 80

4.1 Fraction of polarization potential that drops across array junctions, $|\Lambda_i|$, for 50-island and a 5-island arrays that are symmetrically biased. 90

4.2 *IV and $\partial I/\partial V$ curves of ordered arrays with long range Coulomb interactions.* In Fig. 4.2(a), decreasing N and increasing d/r^{isl} decreases the slope of the IV curves in the region close to the threshold. In Fig. 4.2(b), increasing the biasing asymmetry (increasing $|\alpha - 1/2|$) increases the slope in the low voltage regime with the exception of the perfectly symmetric case which has the largest slope because the symmetry between two bottlenecks doubles the current and its slope in this case. 93

4.3 *IV and $\partial I/\partial V$ curves of disordered arrays with long range Coulomb interactions.* Fig. 4.3(a) shows how varying the charged disorder configuration, $\{\Phi_i^{dis}\}$ changes the slopes and IV curves of 50-island arrays with spacing, $d/r^{isl} = 0.5$. Near the threshold voltage, changing $\{\Phi_i^{dis}\}$ changes the slope by changing the position of the bottleneck. Fig. 4.3(b) shows how varying only the biasing asymmetry (α) affects a disordered array. Increasing the biasing asymmetry does not always increase the slope of the low voltage regime because changing α can change the position of the bottleneck. 94

4.4 *IV and $\partial I/\partial V$ curves for arrays without disorder in the limit of on-site interactions.* In Fig. 4.4(a), the slope of the IV curves of symmetrically biased arrays near their thresholds equals $|\Lambda_1| = 1/2$ when N is even and $2|\Lambda_1| = 1$ when N is odd. The slope is halved when N is even because charges need to cross two bottlenecks (instead of one) before a net charge can be transferred between the leads at these small voltages. Fig. 4.4(b) shows how the slope near the threshold varies both smoothly and abruptly as the biasing asymmetry factor α is varied. The slope varies smoothly with α when modifying α only changes the potential drop across a bottleneck whose position is fixed at either one of the contact junctions. The slope varies abruptly when changing α changes the position of the bottleneck from one contact junction to the other contact junction. 97

4.5 *IV and $\partial I/\partial V$ curves of disordered arrays in the onsite limit.* Fig. 4.5(a) shows the IV and $\partial I/\partial V$ curves of several symmetrically biased arrays:two 5-island arrays with different disorder configurations and a 50-island array. Comparing their slopes near the thresholds shows the independence of the slope on N and $\{\Phi_i^{dis}\}$ when arrays are disordered and symmetrically biased. Fig. 4.5(b) shows how varying the biasing asymmetry (α) alone affects a disordered array. Just as in arrays without disorder, Fig. 4.4(b), the slopes vary smoothly and abruptly with α because varying α can modify the potential drops across the bottleneck(s) and also change the position of the bottleneck from one contact junction to the other contact junction. 98

4.6 *Normalized $i-v$ curves of 50-island arrays.* The resistances of the junctions are described by Eq. 3.14. At large voltages, the $i-v$ curves of arrays with onsite and long range ($d/r^{isl} = 10$ and $d/r^{isl} = 0.5$) interactions are the same and approach the linear resistance form for the current (i^0). The curves due to arrays with different interactions are not distinguished by color or line style because they overlap. 102

4.7 *Probability distribution of bulk junction hopping energies for 50-island arrays with equal junction resistances $R_i = R_0$.* The top, bottom and middle panels correspond to arrays with onsite interactions and with long range interactions and spacings, $d/r^{isl} = 10$ and $d/r^{isl} = 0.5$, respectively. The applied voltages for $P(\Delta E_i)$ in all the panels from left to right equal (8, 4, 2, 1, 0.5)V^0. V^0 equals $100.04E_c^{isl}$, $91.73E_c^{isl}$, and $55.94E_c^{isl}$ in the top, middle, and bottom arrays. When the distributions are centered at the guidelines, drawn for each voltage at $\Delta E_i = I^0 R_i$, the arrays are in the linear resistance regime. The x-axes are labeled in units of $E_c^{isl} = 1/2C_0$ and in units of $E^{e-h} = \sum_{i=1}^{N+1} E_i^{e-h}/(N+1)$. 103

4.8 *Probability distribution of bulk junction hopping energies for 50-island arrays with unequal junction resistances (Eq. 3.14 with* $R = 30$*).* The top, bottom and middle panel correspond to arrays with onsite interactions and with long range interactions and spacings, $d/r^{isl} = 10$ and $d/r^{isl} = 0.5$, respectively. The applied voltages for $P(\Delta E_i)$ in all the panels from right to left equal (8,4,2,1)V^0. V^0 equals $100.04 E_c^{isl}$, $91.73 E_c^{isl}$, and $55.94 E_c^{isl}$ in the top, middle, and bottom panels. The left and right panels focus on the part of $P(\Delta E_i)$ due to the junction with large resistances and the junctions with small resistances respectively. When the distributions are centered at the guidelines, drawn for each voltage at $\Delta E_i = I^0 R_i$, the arrays are in the linear resistance regime. 104

4.9 *IV curves for 50-island arrays with onsite interactions interactions and equal and unequal junction resistances.* The arrays with thin (thick) lines have junction junction resistances described by Eq. 3.14 with $R = 1$ ($R = 30$). The dashed line is a guideline that shows the form of the IV curves in the linear resistance regime (see Eq. 4.8). 105

4.10 *IV curves for 50-island arrays with long range interactions (*$d/r^{isl} = 10$*) and equal and unequal junction resistances.* The arrays with thin (thick) lines have junction junction resistances described by Eq. 3.14 with $R = 1$ ($R = 30$). The dashed line is a guideline that shows the form of the IV curves in the linear resistance regime (see Eq. 4.8). 106

4.11 *IV curves for 50-island arrays with long range interactions (*$d/r^{isl} = 0.5$*) and equal and unequal junction resistances.* The arrays with thin (thick) lines have junction junction resistances described by Eq. 3.14 with $R = 1$ ($R = 30$). The dashed line is a guideline that shows the form of the IV curves in the linear resistance regime (see Eq. 4.8). 107

4.12 *Evolution of* $P(\Delta E_i)$ *at intermediate voltages for a 50-island array with spacing* $d/r^{isl} = 0.5$. The applied voltages of the distributions from left to right are (4, 2, 1)V^0 where $V^0 \approx 55.94 E_c^{isl}$. The solid guidelines show the predicted mean for ΔE_i in the linear resistance regime. The dashed guidelines show the effective tunneling energy, Eq. 4.4 associated with the actual current flow through the arrays. 110

Chapter 1

Introduction

The question of how interactions connect local and global degrees of freedom is a question central to condensed matter research. Sec. 1.1 explains why metallic nanoparticle arrays provide exciting contexts for researching questions of this type. Experiments on these systems combine some control over the microscopic degrees of freedom of electrons with measurements of electronic properties that are the result of the collection motion (or lack of motion) of many electrons. Sec. 1.2 introduces the orthodox theory that has been used to model the electronic properties of these systems. The orthodox model also has the potential to provide illustrative connections between the local and global degrees of freedom of these systems. Sec. 1.3 gives an overview our approach for investigating the electronic properties of metallic nanoparticle arrays and summarizes the organization of this dissertation.

1.1 Metallic Nanoparticle Arrays: Tunable Quantum Solids

Metallic nanoparticle arrays are tunable crystalline solids consisting of nano-sized, typically spherical, metallic particles separated by insulators and arranged in periodic lattices. They are tunable solids because many parameters that affect the electronic proprieties of the arrays are subject to experimental control. These parameters include: the sizes of particles, the mean spacings between particles, the dimensionalities of the systems, and the degrees of disorder in the systems. In addition, the electronic properties of these arrays can be varied by changing the materials that compose the nanoparticles and spaces between them.

Metallic nanoparticle arrays are called quantum solids because the particles that comprise the arrays are small enough that single charge tunneling (SCT) effects are important. The motion between the nanoparticles is a quantum effect because charges move between nanoparticles by tunneling through the insulators that separate them. SCT effects occur when the size of the particles is small enough that the energy to add a single electron to a particle,

$$E_c^{isl} = \frac{e^2}{2C_0} ,$$

is large enough to create a significant feedback against the motion of charges between nanoparticles [12]. C_0 is the self-capacitance of the nanoparticle and is proportional to the radius of the spherical particles; its dependence on the size of the nanoparticle makes it a tunable parameter. The charging energy for typical nanoparticles with radii ranging from 1 to 10 nm is of order 0.1eV. When the temperature is very small compared to the charging energy,

$$E_c^{isl} \gg k_B T ,$$

the charging cost, E_c^{isl}, may block the flow of charge between particles. This is called Coulomb blockade. The theory that describes SCT effects will be discussed in the following section. The remainder of this section gives a brief (by no means exhaustive) overview of the fabrication techniques used to create the arrays that are discussed in this dissertation.

One method for creating nanoparticle arrays is to let a collection of sufficiently monodisperse nanocrystals in a coordinating solvent self-assemble into close-packed hexagonal arrays. Nanocrystals are nanoparticles made of crystalline clusters of atoms with diameters on the order of 1-10 nm. Because they are crystalline arrangements of atoms, it is reasonable to approximate the electronic properties of nanocrystals using the bulk electronic properties of the atoms that compose the nanocrystals. One method to create nanocrystals is to thermally decompose a metal precursor in the presence of a coordinating solvent (often toluene) and a capping ligand, [14, p. 1]. The capping ligands are typically alkanethiols which are organic molecules consisting of chains of methylene groups ($-\mathrm{CH}_2$). After the nanocrystals self-assemble, the capping ligands set the spacing between them. The spacing between the nanoparticles can be varied by using different alkanethiols; these molecules have been shown to vary the interparticle spacing by 1.25 $\mathring{A}$ per methylene group added to the alkanethiol [14, p. 2]. Another method is to reduce a metal (gold) salt inside a mixture of liquid toluene and inverse micelles (water bubbles). The gold atoms crystallize inside the micelles. The size of the nanocrystals is controlled by adding capping ligands that bind to the surfaces of the nanocrystals and discontinue their growth, [36, p. 6-7].

Close-packed hexagonal arrays can not form if the fluctuations in the nanocrystal diameters exceed 10%. Once the nanocrystals are formed, size-selective precipitation methods can be used to make sufficiently monodisperse collections of nanocrystals. In these methods, a chemical that lacks an affinity to the capping ligands is added to the nanocrystal dispersion causing the largest nanocrystals (also the ones coated with the most ligands) to precipitate out of the solution. This can be done repeatedly in order to separate nanocrystals that differ by one atomic layer of thickness, $t \approx 5 - 7\mathring{A}$, [14, p. 2].

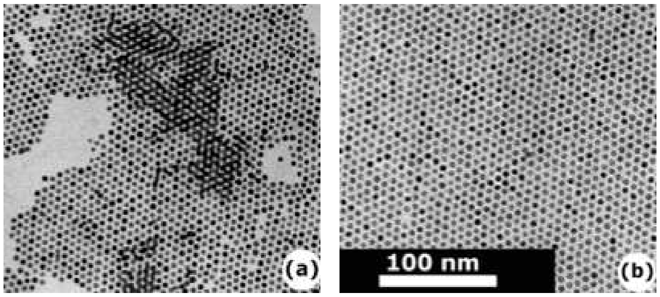

Figure 1.1: Disordered and ordered 2-D arrays from [39] and [36]. (a) Disordered array with regions missing particles (voids) and with double layers (darkened regions). The mean spacing between the nanoparticles in the monolayer regions is $s = 0.85 \pm 0.1$ nm. (b) Ordered array with particle spacing, $s = 1.2 \pm 0.1$ nm. In (a) and (b), the mean radii of the nanoparticles varied between 2.2 nm to 2.9 nm from sample to sample.

Parthasarathy, Lin, and Jaeger (2001) created 2-D arrays displaying long range and short range order in the positions of the gold nanoparticles comprising the arrays [39]. They fabricated the arrays by drop casting a solution of toluene and dodecanethiol-capped gold nanoparticles of mean diameter 5 nm on top of a Si substrate prepatterned with Cr leads. The nanoparticles were monodisperse to within 5 % of the mean size of the particles. They increased the size of the ordered regions by varying the evaporation rate of the toluene and by introducing more dodecanethiol. Slowing the evaporation rate increases the order of the samples by allowing the nanoparticles more time to arrange into close-packed formations. They decreased the evaporation rate by allowing the arrays to dry in a toluene-rich environment . Parthasarathy explained that adding excess capping ligand (dodecanethiol) increased the order in the samples by increasing the mobility of the dodecanethiol-capped gold nanoparticles [36, p. 16]. Particles with greater mobility are better able to arrange themselves into close-packed formations before the motion of nanoparticles stops when all the solvent has dried.

Quasi 1-D arrays can be formed by etching away sections of 2-D arrays. Elteto, Lin, and Jaeger (2005) created the quasi-1-D arrays shown in Fig. 1.2(a) from monolayers of gold nanocrystals [18]. After the monolayers dried, they drew lines in the monolayers using a focused electron beam (e-beam). The e-beam cross linked the capping ligands without affecting the positions and sizes of the nanoparticles thus enabling the treated ligands to resist dissolving in heated toluene. After the monolayers were washed in heated toluene, all the nanoparticles were removed except for the ones in the regions exposed to the e-beam.

Another way to create quasi-1-D and 1-D arrays is to let nanoparticles self assemble while they are dispersed in a dielectric fluid that is subject to an electric field. Bezryadin, Westervelt, and Tinkham (1999) used this technique to create the carbon nanoparticle chains shown in Fig. 1.2(b). They immersed a Si substrate prepatterned with Cr leads into a suspension of carbon nanoparticles in toluene. They applied a field between the electrodes until a jump in the current occurred indicating the formation of a chain of nanoparticles connecting the leads.

Another way to create 2-D and 1-D arrays is to combine e-beam lithography techniques with an ionized beam deposition method [7, 8]. This technique can be used to make very narrow 2-D arrays and 1-D arrays. In this technique, an e-beam is used to draw a thin line in photoresist. Then, AuPd atoms are evaporated through an electron beam while an accelerating voltage is applied to the sample. The atoms nucleate into small islands after being deposited on top of the sample. After liftoff, only the grains lying on the resist region remain. This technique can be used to fabricate channels of grains that are only one grain thick. See Fig. 1.2(c).

This selection of techniques illustrates how nanoparticle arrays are tunable systems that can be used to enhance our understanding of electronic transport. The barriers that single electrons face as they move through nanoparticles can be actively varied by changing the sizes and spacings between nanoparticles and by varying the degree of disorder in the arrangements of the nanoparticles. The measured responses of charges to electric fields applied across nanoparticle arrays are collective effects caused by the motion of many electrons that influence each other via long range

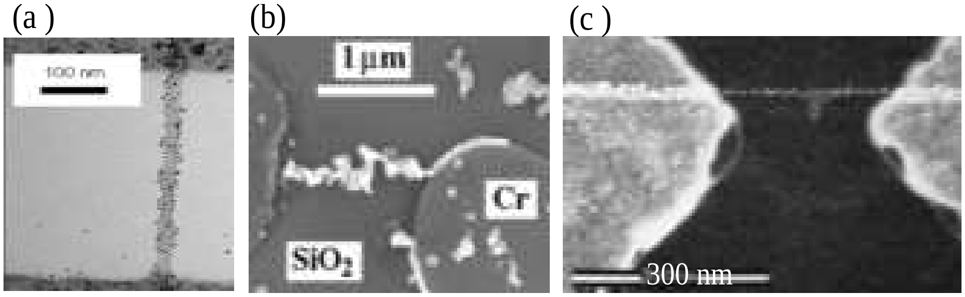

Figure 1.2: *One-dimensional (1-D) and quasi-1-D nanoparticle arrays.* (a) A quasi-1-D array from [18] composed of 5.5 nm gold nanoparticles with 5-7% dispersity spaced 1.3 nm apart on average. The array spans a 30 nm gap between two planar Cr electrodes. (b) A chain of graphitized carbon nanoparticles with diameter, $d \approx 30$ nm, from [4]. The chain of length, $L \approx 1.2\mu$m, connects two Cr electrodes. (c) A 1-D array of 13 gold grains of mean radius, $r \approx 3nm$, between two electrodes from [8].

Coulomb interactions. The ability to tune the barriers faced by single electrons while measuring the currents and fields created by many electrons allows us to investigate how interactions mediate microscopic and mesoscopic degrees of freedom. The following section discusses a standard model for single electron tunneling that can be used to predict the flow of charges through nanoparticle arrays as functions of the tunable parameters discussed in this section.

1.2 Orthodox Model of Single Charge Tunneling

The orthodox model is a quasiclassical description of single electron tunneling through tunneling barriers with large resistance, R_T, and very small capacitance, C. The model is quasiclassical because charges are allowed to tunnel through barriers that are classically forbidden, yet the numbers of charges on each conductor and the interactions among the charges are treated as classical variables. The orthodox expression for the average probability that a single electron will tunnel through a barrier separating two *adjacent* conductors is given by

$$\Gamma_{i\rightarrow i\pm 1} = \frac{1}{e^2 R_T}\frac{\Delta E}{1-\exp\left(\frac{\Delta E}{k_B T}\right)} \ .$$

$\Delta E = E_f - E_i$ is the difference between the values of the total electrostatic energy of the system before and after the tunneling event. This section discusses the main assumptions of the orthodox model and the length scales of systems of conductors that are well described by this model. It concludes with a discussion of how the orthodox model can be used to model the electronic properties of nanoparticle arrays.

The charges are approximately localized on each nanoparticle when the energy fluctuations due to the typical lifetime of a state are very small compared to the typical energy cost of adding a single charge to a nanoparticle, $E_c^{isl} = e^2/(2C)$ [12]:

$$\begin{aligned} \delta E \delta t &\geq \frac{\hbar}{2} \\ \delta E &\geq \frac{\hbar}{2\delta t} = \frac{\hbar}{2\left(R_T C\right)} \ll \frac{e^2}{2C} \ . \end{aligned} \tag{1.1}$$

In Eq. 1.1, the typical duration of an excess charge on a nanoparticle is taken to be the RC time, $\delta t \approx R_T C$, where R_T is the resistance of the tunnel barrier surrounding the nanoparticle. Resistance values that satisfy Eq. 1.1 are very large compared to the quantum resistance R_Q,

$$R_T \gg R_Q = \hbar/e^2 \approx 25.8\Omega \ .$$

When Eq. 1.2 is satisfied, the tunneling of charges between two adjacent nanoparticles can be treated as a perturbation. The Fermi golden rule approximation for the average tunneling rate between two adjacent sites within an array with N sites is given by [30]

$$\begin{aligned}\Gamma^{\pm} &= \frac{2\pi}{\hbar}\sum_{i,f}|T_k|^2_{i,f}f(\epsilon_i)[1-f(\epsilon_f)] \\ &\times \delta\left\{(E(n_1,\ldots,n_i,\ldots,n_N)+\epsilon_i)-(E(n_1,\ldots,n_f\pm 1,\ldots,n_N)+\epsilon_f)\right\}\ .\end{aligned} \tag{1.2}$$

$f(\epsilon_i)$ and $f(\epsilon_f)$ are the Fermi functions of the initial and final sites of the tunneling event and $\{n_1\ldots n_N\}$ are the number of excess charges on each site. The product involving the Fermi functions determines the probability of finding an occupied state on the initial site and an empty state on the final site of the same energy . The initial and final states are assumed to be equilibrium states. This is true when the time between hops, t_{hop}, is large compared to the time for the charges to relax to their electrostatic equilibrium positions, t_{relax}:

$$t_{hop} \gg t_{relax}\ .$$

Eq. 1.2 describes elastic collisions. Inelastic collisions that exchange energy between the system and its environment are not included. E_i and E_f are the initial and final free energies of the system due to the electrostatic interactions among the charges in the system. These interactions create a relative shift in the Fermi energies of the two sites that can enable or prohibit tunneling depending on whether or not occupied states align with vacant states of the same energy.

Metals can be treated in the continuum limit when the spacing between energy levels near the Fermi level is small relative to the charging energy:

$$\Delta \ll \frac{e^2}{2C}\ .$$

In this limit, Eq. 1.2 can be integrated and the result is the orthodox tunneling rate:

$$\begin{aligned}\Gamma_j^{\pm} &= \frac{1}{e^2 R_T}\int d\epsilon_i d\epsilon_f f(\epsilon_i)[1-f(\epsilon_f)] \\ &\times\ \delta\left\{(E(n_1,\ldots,n_i\ldots,n_N)+\epsilon_i)-(E(n_1,\ldots,n_f\pm 1,\ldots,n_N)+\epsilon_f)\right\} \\ &= \frac{1}{e^2 R_T}\frac{\Delta E_{i\to i\pm1}}{1-\exp\left(\frac{\Delta E_{i\to i\pm1}}{k_B T}\right)} \text{ where } \Delta E_{i\to i\pm1} = E_f - E_i\ . \end{aligned} \tag{1.3}$$

The tunneling matrix elements and the density of states are included in the tunneling resistance, $R_T^{-1} = 4\pi N\tau R_Q^{-1}$. The tunneling matrix elements are assumed to be very small and nearly equal to a constant near the Fermi level such that $\sum |T_k|_{i,j}^2 \to N\tau$. The tunneling resistance can be defined phenomenologically for a specific tunnel junction by measuring the current, I, across the junction when the junction is biased by a unit potential: $I \approx e\Gamma = (R_T)^{-1}$ [12]. The orthodox tunneling rate, Eq. 1.3, does not include cotunneling events that involve the motion of more than one electron at one time through different barriers as a result of a single coherent process. The rates of these processes are roughly a factor of $(R_Q/R_T)^{N-1}$ smaller than the orthodox tunneling rates where N is the number of charges that move as a result of a cotunneling process [31]. Systems that are well described by Eq. 1.3 have large enough tunneling resistances (Eq. 1.2) that cotunneling effects are negligible.

Eq. 1.3 expresses the average tunneling rate as a function of temperature, T, and the change in the total electrostatic energy of the system before and after the tunneling event, ΔE. Raising the temperature increases the tunneling probability because thermal fluctuations create occupied (vacant) states above (below) the Fermi levels of the nanoparticles. The tunneling probability increases as ΔE decreases. When the temperature is very small compared to the charging energy, $kT << E_c^{isl}$, the tunneling probability is only finite when tunneling lowers the free energy of the system:

$$\Gamma_{i\to i\pm1} \approx \begin{cases} \frac{1}{e^2R_T}|\Delta E_{i\to i\pm1}| & \text{when } \Delta E_{i\to i\pm1} < 0 \ . \\ 0 & \text{when } \Delta E_{i\to i\pm1} \geq 0 \ . \end{cases}$$

Eq. 1.2 is exact when the temperature is at absolute zero. Coulomb blockade occurs when charging costs ($\Delta E > 0$) inhibit the ability of charges to tunnel between neighboring sites. Coulomb blockade can be overcome by applying currents or potentials that modify the potentials across junctions such that $\Delta E < 0$.

The orthodox tunneling rate is the tunneling probability associated with a single charge tunneling through a singe tunnel barrier. When currents flow through nanoparticles arrays, many charges tunnel through many tunnel barriers. Two ways to extend the orthodox model to these systems is to use a master equation approach and to conduct Monte Carlo simulations. The master equations for systems that involve multiple junctions become too complex to make analytical predictions for arrays with more than a few tunnel junctions.

Monte Carlo methods can be used to simulate the motion of charges through many junctions. These methods iteratively simulate the stochastic tunneling events that underly the values of time-averaged quantities such as the average current through the array, the average current through a junction, the average potential across a junction, etc. During each iteration of the simulation, a tunneling event is selected, the charge state of the arrays is modified to reflect the selected tunneling event, and the average time interval between successive tunneling events,t_{hop}, is calculated. The iterations are repeated until the time-averages of the quantities of interest have converged.

During each iteration, the orthodox tunneling expression is used to select the tunneling event and to calculate t_{hop}. One begins by calculating the energy costs, ΔE_i, associated with every possible tunneling event that can occur across the N_j

junctions in the array. Since the charge at each nanoparticle is known at all times, ΔE_i can be determined using an appropriate model for the electrostatic interactions among the charges on the array. A discussion of the various models of electrostatic interactions that have been used to model transport through nanoparticle arrays is included in Sec. 2.1. Using ΔE_i and Eq. 1.3, one calculates the probabilities associated with every possible tunneling event and then maps these probabilities on to a number line comprised of segments of lengths proportional to all the tunneling events. During each iteration of the simulation, a random number generator selects a random number that falls inside a bin on the weighted number line that corresponds to a specific tunneling event between sites i and $i \pm 1$. The selected event is used to modify the charges on the array such that $Q_i \rightarrow Q_i - 1$ and $Q_{i\pm1} \rightarrow Q_{i\pm1} + 1$. The total tunneling probability due to all the possible events,

$$\Gamma_{tot} = \sum_{i=1}^{N_j} \Gamma_i^{\pm} \, ,$$

is related to the probability, P, that any process will occur in a time interval, t_{hop}, by

$$P = \exp\left(-\Gamma_{tot} t_{hop}\right) \, .$$

Whether or not a process occurs in any time interval is a stochastic process. To model the average time, t_{hop}, associated with this process, one can select a random number between 0 and 1 and use this number and Eq. 1.2 to determine t_{hop}.

Monte Carlo simulations powered by the orthodox tunneling rate have been used in many works to model the the electronic properties of metallic nanoparticle arrays. See for example [32, 35, 33, 9, 2, 29, 26, 24]. The convergence between theory and experiments has been complicated by the complexity of the Coulomb interactions among charges occupying actual nanoparticle arrays and by the complexity of the disorder in the arrays. A variety of different predictions have been

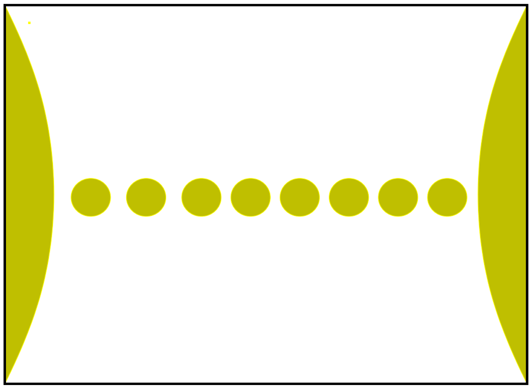

Figure 1.3: 1-D arrays of N spheres of radii, r_{isl}, sandwiched between two large spherical leads of radii, R_{lead} (not drawn to scale).

made by different works that use different models for disorder and for the Coulomb interactions among charges. These models are discussed in Sec. 2.1. The threshold predictions that have been made using these models are discussed in Sec. 3.1. The current-voltage characteristics that have been predicted and justified using these models are discussed in Sec. 4.1.

1.3 Overview of our approach and the organization of this thesis

We have investigated how realistic models of Coulomb interactions and of disorder affect the electronic properties of 1-D nanoparticle arrays. We modeled long range Coulomb interactions that include the screening due to proximity of other conductors (the nanoparticles and the leads) by determining the inverse capacitance matrices of systems of N spheres of radii, r_{isl}, representing the nanoparticles sandwiched between two large spheres of radii, $R_{lead} = 100r_{isl}$, that represent the leads. See Fig. 1.3. To investigate the effects of array length, particle size, and spacing on Coulomb interactions, we calculated the inverse capacitance matrices for several N and several d, the spacing between the closest surfaces of adjacent spheres. Along with including the leads in our inverse capacitance calculations, we developed a method for describing the leads as non-ideal voltage sources that have potentials that fluctuate in the response to changes in the charge states of the arrays. Ch. 2 discusses the models that have been used to describe disorder and Coulomb interactions in nanoparticle arrays. This chapter also discusses how we model these effects and compares our approach to other models.

We use the orthodox model coupled with this description of the Coulomb interactions to model electronic transport through the 1-D arrays. Ch. 3 focuses on the work we did to understand the static states of the arrays. We investigated how disorder, particle size, particle spacing, and long range Coulomb interactions affect the state of the arrays at their threshold voltages and at voltages smaller than the threshold voltages. At zero temperature, the threshold voltage is the minimum applied voltage that allows a current to pass through an array. To better understand how the local characteristics of arrays relate to the characteristics of the arrays taken as a whole, we calculate the probability distributions of the static potential gradients across individual junctions between neighboring spheres at the threshold voltage and voltages leading up to the threshold. To investigate the effects of long range Coulomb interactions, we analyzed and compared the static states of systems with spacings comparable to experiments, $d/r^{isl} = 0.5$, with systems with very short range Coulomb interactions. To investigate the effects of disorder, we analyzed and compared the properties of systems with and without disorder.

Ch. 4 discusses our work on the dynamic states of the arrays. Similar to our approach in Ch. 3, we compared the behavior of systems with and without disorder and with and without long range Coulomb interactions. We studied how the scaling of IV curves is affected by applied voltage, particle size and spacing, and the presence and absence of disorder. As in Ch. 3, we investigate how these array characteristics relate to the characteristics of individual array junctions by calculating the probability distributions of the time-averaged potential gradients across array junctions.

Ch. 5 summarizes our results and conclusions and discusses avenues for future work.

Chapter 2

Models of Electron Transport in Metallic Nanoparticle Arrays

Single charge tunneling (SCT) effects, long range Coulomb interactions, and disorder complicate models of transport through nanoparticle arrays. This chapter discusses methods for incorporating these effects into the orthodox model discussed in Sec. 1.2. Sec. 2.1 reviews a selection of theoretical models that describe Coulomb interactions among charges on nanoparticle arrays and that model different types of disorder. In Sec. 2.2, I discuss our model for transport. The new features of our model include a realistic treatment of the biasing leads and expressions for the free energy that make the interactions among the charges on the array and the leads more transparent.

2.1 Background

2.1.1 Models of Electrostatic Interactions

According to the orthodox model, the probability of tunneling between two neighboring conductors is a function of the change in the electrostatic energy of the system, ΔE, as a result of the tunneling event. The model treats the charges at each conductor as well-defined quantities that can be used to determine ΔE prior to each hop. At any given time between tunneling events, the total electrostatic energy of a nanoparticle array composed of N nanoparticles and a source and drain lead is given by

$$E = \frac{1}{2}\sum_{i=1}^{N} Q_i\phi_i + \text{ terms involving the leads } .$$

Most models divide the total electrostatic energy between terms that describe interactions among charges on the nanoparticles and terms that describe interactions that involve charges on the leads. The nanoparticles and the leads are treated differently for several reasons. One reason is that the leads and the nanoparticles have very different capacitances because the leads tend to be much larger than the nanoparticles. Another reason is that the leads are either voltage or current biased. They are connected to batteries that either maintain or effectively maintain their potential values, whereas the nanoparticle potentials vary each time the charge configuration of the array changes. Because the leads are connected to batteries, the charges on the leads can vary discretely and continuously; the charges on the nanoparticles only vary discretely in integer amounts of e. In both cases, the discrete changes are a result of tunneling events. The lead charges vary continuously because the batteries bias the leads by transferring charge to and from the leads and by polarizing the charge on the leads.

In general, the charges and the potentials of N conductors are related by the capacitance matrix and its inverse:

$$Q_i = \sum_{j=1}^{N} \phi_i C_{i,j} \tag{2.1}$$

$$\phi_i = \sum_{j=1}^{N} C_{i,j}^{-1} Q_j \ . \tag{2.2}$$

The capacitance matrix is a function of the relative positions and sizes of the conductors. When this matrix is determined exactly, its elements describe all the *screened* interactions among the charges on the N conductors. The matrix element $C_{i,j}$ is the induced charge at conductor i when all the conductors are grounded except conductor j which has a unit potential. $C_{i,j}$ is positive when $i = j$ and negative otherwise because conductors with positive unit potentials induce positive charges on themselves and negative charges on nearby grounded conductors. Similarly, the matrix element $C^{-1}_{i,j}$ is the induced potential at conductor i due to a unit charge at conductor j while the remaining conductors are neutral. $C^{-1}_{i,j}$ is always positive. When screening is negligible, $C^{-1}_{i,j}$ varies with $r_{i,j}$, the distance between conductors i and j, in the same way that the potential of a point charge varies with distance, $C^{-1}_{i,j} \propto r^{-1}_{i,j}$. When screening is important, $C^{-1}_{i,j}$ is a more complicated function of $r_{i,j}$.

Likharev, Bakhalov, Kazach, and Serdyukova (1989) [32, 10] used an infinite periodic array of capacitors (Fig. 2.1) to model one-dimensional (1D) nanoparticle arrays. The capacitors in the network are of two types, C and C_0, where C is the mutual capacitance between nearest neighboring conductors and C_0 is the self capacitance of a nanoparticle. They do not include capacitors that model the capacitative coupling between conductors that are not nearest neighbors. In terms of C and C_0, they estimate the capacitance matrix of the 1-D array in the following way [1]:

$$C_{i,j} = \begin{cases} C_0 + 2C & \text{when } i = j \\ -C & \text{when } i = j \pm 1 \\ 0 & \text{otherwise} \end{cases} .$$

---

[1] Eq. 2.1.1 is consistent with equation (7) in [32], but inconsistent with equation (2) in the same reference. In the limit of $C_0 \ll C$, the capacitance elements in equation (2) in [32], $C_{i,i} = C_0$ and $C_{i,j\pm1} = C$, are unphysical because the definition of $C_{i,j}$ requires that $|C_{i,i}| > |C_{i,j\neq i}|$. In general, the diagonal elements of capacitance matrices of this form equal $C_0 + nC$ where n is the number of nearest neighbors surrounding a conductor.

The inverse of this matrix has off-diagonal elements that decay exponentially over a characteristic length, M:

$$C_{i,j}^{-1} = \frac{1}{C_{eff}} \exp\left(-|i-j|/M\right)$$

where M and C_{eff} are given by

$$M^{-1} = \ln\left(\frac{C_{eff} + C_0}{C_{eff} - C_0}\right) \approx \sqrt{\frac{C_0}{C}} \text{ when } C \gg C_0$$

and

$$C_{eff} = \sqrt{C_0^2 + 4CC_0}\ .$$

C_{eff} is the effective capacitance of the network of capacitors shown in Fig. 2.1(a). Fig. 2.1(b) shows how the periodic symmetry of the network can be used to determine C_{eff}. Unlike the capacitance matrix in Eq. 2.1.1, the inverse capacitance matrix, Eq. 2.1.1, has many off-diagonal elements that are finite-valued. Despite the form of the capacitance matrix, Coulomb interactions in this model are not restricted to onsite and nearest neighbor interactions unless $M < 1$. By definition, Eq. 2.1.1 is the potential distribution that is induced by a single excess charge. Likharev, et al. call this distribution a soliton, and M, a soliton length, because the potential distribution maintains its shape as long as the charge carrier is far from the edges of the array [32].

Likharev, et al. [32] numerically determined the DC characteristics of the array using a Monte Carlo simulation and the orthodox expression for the tunneling rate between two neighboring conductors, Eq. 1.3. At each instance, the charges on the N nanoparticles, $Q_1.Q_2.\ldots,Q_N$, are known and the charges on the source and drain leads are given by

$$Q_+ \quad = \quad C\left(\phi_1 - \phi_0\right) - em_+$$

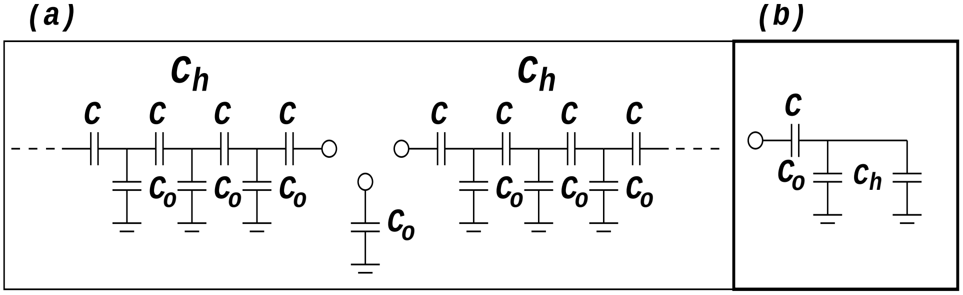

Figure 2.1: *Effective circuit model for 1-D nanoparticle array* C and C_0 are the mutual capacitance between nearest neighboring islands and the self-capacitance of the islands. islands. C_h is an infinite periodic network of capacitors. The effective capacitance of the network in Fig. 2.1(a) equals $C_{eff} = C_0 + 2C_h$. The periodic symmetry of C_h can be used to show that $C_h^{-1} = C^{-1} + (C_0 + C_h)^{-1}$. See Fig. 2.1(b). This figure is modeled after figures in [32] and [10].

$$Q_- \quad = \quad C\left(\phi_{N+1} - \phi_N\right) + em_-$$

where m_+ (m_-) is the number of electrons that tunnel through the junction closest to the source (drain) lead. They use the inverse capacitance matrix, Eq. 2.1.1, and Eq. 2.2 to solve for the charges on the leads and the potentials at each nanoparticle given the numbers of charges at each nanoparticle, the number of charges that have tunneled into and off the array (m_+ and m_-), and the applied potentials at the source and drain, V_+ and V_-. They express the total electrostatic energy as

$$E = \frac{C_0}{2}\sum_{i=1}^{N}\phi_i^2 + \frac{C}{2}\sum_{i=1}^{N+1}\left(\phi_i - \phi_{i-1}\right)^2 - V_+Q_+ - V_-Q_- \; .$$

The potentials on the source and drain leads are treated as constants because the leads are connected to batteries and because they are assumed to have infinite capacitance. Prior to each tunneling event, they calculate the tunneling probabilities of each possible hop using the orthodox tunneling rate, Eq. 1.3, and $\Delta E = E_f - E_i$ where E_f (E_i) is determined by using Eq. 2.1.1 and the charges on the array after (before) each possible hop. The Monte Carlo method used to model the average current through the array is described in detail in Sec. 6.1.

Many works [11, 35, 34, 4, 9, 2, 3, 29, 26, 24, 28, 47] have applied the approach pioneered by Likharev, et al. to model the interactions and dynamics of 1-D arrays because the simple form of Eq. 2.1.1 and Eq. 2.1.1 allows for a ready calculation of $C_{i,j}$ and $C^{-1}_{i,j}$ for very large arrays. Some works [34, 26] focus on Coulomb interactions where M is much larger than the size N of the array. Other works focus on the opposite where the soliton length is very small compared to the length of the array, [35, 24, 3, 47].

Middleton and Wingreen (1993) [35] added charged background disorder to the soliton model. They used Eq. 2.1.1 for their inverse capacitance matrix and they numerically found transport and threshold results over a wide range of soliton lengths. They also obtained analytical results in the onsite limit:

$$C^{-1}_{i,j} = C_0 \delta_{i,j} \ .$$

They justified the onsite limit by including a large grounded back gate to their model to screen out long range Coulomb interactions. They expressed the total free energy of N nanoparticles sandwiched between a source and drain lead and adjacent to a large back gate as

$$E = \sum_{i,j=1}^{N} (Q_i + q_i) C^{-1}_{i,j} (Q_j + q_j) + V_L Q_L + V_R Q_R + \sum_{i=1}^{N} V_i^{ext} Q_i$$

where

$$V_i^{ext} = \sum_{x} C_x \sum_{j}^{x} C^{-1}_{i,j} V_x \ .$$

Q_i are the excess changes on the N nanoparticles and q_i are offset charges that model random background disorder. The following section discusses disorder models in more detail. In Eq. 2.1.1, C_x is the mutual capacitance C and the sum over x

is a sum that includes the source and drain leads with potentials V_L and V_R and the grounded back gate with potential $V_G = 0$. The sum over j in Eq. 2.1.1 is a sum over the charges that are adjacent to each lead. The leads were assumed to have infinite self capacitances and potentials fixed to bias values. Including disorder led to new results on the relationship between the threshold voltage and the lengths of nanoparticles arrays. The threshold voltage is the smallest applied voltage that overcomes the Coulomb blockade that prevents the flow of current across nanoparticle arrays. Likharev, et al. predicted that the threshold voltage is largely independent of the array length measured in the numbers of nanoparticles, N. Middleton and Wingreen found the threshold voltage is proportional to N. These threshold results and other predictions are discussed in Sec. 3.1.2.

2.1.2 Models of Disorder

Nanoparticle arrays can be fabricated that exhibit periodic symmetry over many nanoparticles. Despite this symmetry, there are several types of disorder that keep arrays from being perfectly symmetric. The main types of disorder are structural disorder and charged disorder. Structural disorder includes fluctuations in the sizes of and spacings between the nanoparticles. It also includes voids, regions of the lattice that are missing one or more nanoparticles. Charged disorder is due to randomly scattered, charged impurities lodged in the materials surrounding the nanoparticles. This section discusses how disorder of different types has been incorporated into models of nanoparticle arrays.

Middleton and Wingreen (MW) [35] were the first to incorporate charged disorder in models of charge transport through one-dimensional (1-D) and two-dimensional (2-D) nanoparticle arrays. They included offset charges to each nanoparticle that represented the induced charges due to charged impurities in the substrate. These charges assumed random values between 0 and e. The values vary continuously in this interval because they are the result of the polarization of each island by the potentials created by nearby charged impurities. They are constrained within this interval because mobile charges lying on the nanoparticles tunnel when the potential difference between a pair of neighboring particles becomes larger than the charging energy $E_c^{isl} = e^2/2C_0$. Including these charges leads to a linear relationship between the threshold voltages of arrays and their lengths. This threshold dependence is discussed in more detail in Sec. 3.1.2.

Kaplan, Sverdlov, and Likharev (2003) [26] developed a numerical algorithm to determine the offset charges when interactions among charges are long range. The algorithm determines the equilibrium configuration for the mobile charges that screen out the induced charges due to charged impurities in the substrate. They add charge to each island until doing so no longer lowers the total electrostatic energy, E_{tot}, of the system. Then they let mobile charges hop between neighboring sites until E_{tot} stops decreasing. They alternate between adding charges and letting them move until E_{tot} assumes its minimum value. The final result is the annealed state of the mobile charges after the system has relaxed to its global equilibrium state. This approach finds offset charges whose values are influenced by interactions with other offset charges. They statistically analyzed the distribution of energies to add charge to each site, E^{add}, when arrays are in their annealed states in order to determine the density of states of the arrays. They defined the density of states as the derivative, $\delta P(E^{add})/\delta E^{add}$, where $P(E^{add})$ is the distribution of probabilities associated with each value of E^{add}. They found a suppression of the density of states at small values of E^{add}. They called this a Coulomb gap and remarked that this gap is the sequential tunneling (ST) version of the Efros-Schlovskii (ES) Coulomb gap. The main differences between ST and ES Coulomb gaps are that the former only include hops between adjacent sites whereas the ES model is a variable range hopping model. Also, the ES model uses an unscreened form for the Coulomb interactions among charges ($\phi \propto r^{-1}$) whereas the ST model includes screened interactions among charges. They calculated the temperature dependence of the zero bias conductance, $G_0(T)$, and found that it did not have the Efros-Schlovsii dependence: $G_0(T) \propto \exp(-(T_0/T)^{1/2}$. Instead, for both the 1-D and 2-D cases, they found that $G_0(T)$ followed an Arrhenius dependence: $G_0(T) \propto \exp(-U_0/(k_B T))$ where U_0 is an energy barrier that thermally activated charges overcome to generate current. They determined U_0 for arrays of varied length; for each length, they averaged over many configurations of disorder. They called U_0 a soft barrier because they found that it was smaller than E^{add}_{max}, the maximum value of E^{add}, for all arrays. They expected U_0 to equal E^{add}_{max} if disorder created a hard profile of energy barriers because in this case E^{add}_{max} equals the largest barrier charges must overcome to enable current flow. They attributed the small size of U_0 to thermally injected charges modifying the distribution of array potentials away from the annealed distribution [26].

Elteto, Antonyan, Nguyen, and Jaeger (2005) [17] analytically found the probability distributions associated with the potential differences due to disorder for 1-D and 2-D arrays with onsite interactions, Eq. 2.1.1, and with nearest neighbor interactions:

$$C^{-1}_{i,j} = \begin{cases} C_0^{-1} & \text{when } i = j \\ C^{-1} & \text{when } i = j \pm 1 \\ 0 & \text{otherwise} \end{cases} .$$

Unlike the soliton model (Eq. 2.1.1), Eq. 2.1.2 is truncated to exclude interactions among charges on nanoparticles that are spaced farther than one site apart. Like Middleton and Wingreen, they modeled charged disorder using offset charges, q_i. They allow the offset charges to vary stochastically between $\pm e/2$. They expressed the potential differences across each junction in terms of the offset charges, q_i. For example for 1-D arrays, the potential difference across the junction between sites i

and $i-1$ equals

$$\Phi_i^{dis} = 2E_c^{isl}(1-\gamma)(q_i - q_{i-1}) = \Phi_{max}^{dis}(q_i - q_{i-1}) \tag{2.3}$$

where $\gamma = C_0/C$. They used properties of random numbers to derive analytical expressions for the distribution of probabilities, $P(\Phi^{dis})$, associated with each value of Φ^{dis} between $\pm\Phi_{max}^{dis}$ for 1-D and 2-D arrays. In the limit of onsite interactions ($\gamma = 0$), they found that this distribution equals

$$P(\Phi^{dis}) = \frac{1}{\Phi_{MAX}^{dis}}\left(1 - \frac{|\Phi^{dis}|}{\Phi_{MAX}^{dis}}\right) .$$

For $\gamma \neq 0$, they focus on the shape of $P(\Phi^{dis})$ near small values of Φ^{dis} because junctions with small disorder potentials are most sensitive to thermal fluctuations. They use $P(\Phi^{dis} = 0)$ to approximate the shape of the distribution for small values of Φ^{dis}. For 1-D arrays, they found $P(0)$ to equal [2]

$$P(0) = \frac{1}{2E_c^{isl}}\frac{1-4\gamma/3}{(1-\gamma)^2} \text{ for } \gamma < 1/3 .$$

They use these distributions to predict how the threshold of arrays respond to increases in temperature. These threshold predictions are discussed in more detail in Sec. 3.1.2. Sec. 2.2.2 compares Elteto, et al.'s results to our disorder results.

The works previously discussed in this section investigated the effects of charged disorder while ignoring the effects of structural disorder. The remaining works discussed in this section focus either on structural disorder or a combination of charged and structural disorder.

Cordan, Goltzene, Herve, Mejias, Vieu, and Launois (1998) [8] numerically investigated how variations in the spacings between nanoparticles affect transport through nanoparticle arrays. They did not include charged disorder in their model. They derived approximate analytical expressions for the mutual capacitance, C, of a pair of nanoparticles and the tunneling resistance, R_T, of the barrier between them in terms of the radii of the nanoparticles, r, and their spacing, d. They used these expressions to include variations of R_T and C into their numerical model due to particles of equal radii,r, with randomly varied spacings, d, whose size relative to r and acceptable range were justified by their experimental parameters: $\langle d\rangle/r \approx 1/3$ and $\langle d\rangle = 2.5 \pm 0.2$ nm. They investigated how variations in d affect the total array resistance and the zero temperature threshold of 1-D and 2-D nanoparticle arrays. In later works [38, 9], they used the same model of structural disorder to investigate the temperature dependence of 1-D and 2-D array thresholds.

---

[2] Eq. 2.1.2 and Eq. 2.3 are written in units of E_c^{isl} for easier comparison with our results. In [17], the same expressions are written in units of $e^2C_0^{-1} = 2E_c^{isl}$.

Jha & Middleton (2005) [24] expanded the Middleton & Wingreen model by including some types of structural disorder. They focused on the limit of onsite Coulomb interactions, Eq. 2.1.1. They used the same model for charged disorder as Middleton & Wingreen. In addition, they randomly varied the onsite capacitances, C_0, of the nanoparticles in Eq. 2.1.1. These fluctuations model changes to the charging energies of the islands due to variations in the sizes of the islands and variations in their coupling to the back gate. They also treated the tunneling resistances as a log normal distribution. This models fluctuations in the spacings between nanoparticles since the sizes of the tunnel barriers are exponentially related to the tunneling resistances. They found that charged disorder was the major factor in determining the relationships between the threshold and array length, N, and between the current and applied voltage. Their threshold results are discussed in more detail in Sec. 3.1.2 and their IV results are discussed in Sec. 4.1.

2.2 Our Transport Model

We model the dynamics and the static states of a one-dimensional system of nanoparticles using the orthodox theory for the tunneling rates. The details of the Monte Carlo algorithm we used to simulate this system are discussed in Sec. 6.1. Our main innovations to this standard technique are the methods we use to include the interactions among charges situated on the nanoparticles and the leads. In Sec. 2.2.1, I describe how we write the total free energy and the relevant change in the free energy that appears in the orthodox tunneling rate equation. In Sec. 2.2.2, I discuss how we include disorder in our model.

2.2.1 Our Model for the Coulomb Interactions of 1-D Nanoparticle Arrays

We model one-dimensional arrays of N nanoparticles sandwiched between a source and drain lead as N spheres of radius, r_{isl}, in between two larger spheres of radius, R_{lead}. In this section, we call the spheres of radii, r_{isl}, *islands* or nanoparticles. The word, *site*, is used to denote any conductor in the system and includes spheres of radii, r_{isl} and R_{lead}. The surface to surface distance between every pair of adjacent sites equals d. We numerically determined the inverse capacitance matrix, $C_{i,j}^{-1}$, of several arrays with different N and d in order to determine how array length and spacing affects the electrical properties of nanoparticles arrays. For the smallest spacings, we determined $C_{i,j}^{-1}$ using a multipole method. This method is discussed in Sec. 6.2.2. We include the leads in our systems so that we can study how their proximity modifies the electrostatic coupling among charges on the nanoparticles. We also include the leads to see how the islands affect the way that the applied bias is distributed over the junctions in the array.

In the absence of charged disorder, we write the total electrostatic energy of a system of charges residing on N nanoparticles and two leads as

$$E = \frac{1}{2} \sum_{\alpha=0}^{N+1} Q_\alpha \phi_\alpha$$

where

$$\phi_\alpha = \sum_{\beta=0}^{N+1} C^{-1}_{\alpha,\beta} Q_\beta \ .$$

Indices 1 through N represent the nanoparticles and indices 0 and $N+1$ label the source and drain leads respectively. According to Eq. 2.2.1, the potentials of all the conductors, including all the islands and both leads, are affected by all the charges on the conductors. We model the leads as non-ideal voltage sources that have potentials that fluctuate in response to the motion of charges in our system.

Unlike the nanoparticles, the leads are connected to a battery that continuously modifies the charges on the source and drain, Q_0 and Q_{N+1}, in order to maintain their bias values: $\phi_0 = V_0$ and $V_{N+1} = V_{N+1}$. Using Eq. 2.2.1. one can determine that

$$\begin{aligned} Q_0 &= C^2_{gen} \left[C^{-1}_{N+1,N+1} V_0 - C^{-1}_{N+1,0} V_{N+1} - \sum_{i=1}^{N} Q_i \left(C^{-1}_{N+1,N+1} C^{-1}_{i0} - C^{-1}_{N+1,0} C^{-1}_{i,N+1} \right) \right] \\ Q_{N+1} &= C^2_{gen} \left[C^{-1}_{0,0} V_{N+1} - C^{-1}_{N+1,0} V_0 - \sum_{i=1}^{N} Q_i \left(C^{-1}_{00} C^{-1}_{iN+1} - C^{-1}_{N+1,0} C^{-1}_{i0} \right) \right] \end{aligned}$$

with

$$C^2_{gen} = \left[C^{-1}_{00} C^{-1}_{N+1,N+1} - (C^{-1}_{N+1,0})^2 \right]^{-1}$$

when $\phi_0 = V_0$ and $\phi_{N+1} = V_{N+1}$. The sums in Eq. 2.4 and Eq. 2.4 describe the induced charges on the source and drain leads due to the charges on each island. The first and second terms in each sum equal the charges that are directly and indirectly induced on each lead by the charges on the islands. The charges on the islands directly induce charges of opposite sign relative to themselves on each lead.

The directly induced charges on each lead induce more charges on the opposing lead. These are the indirectly induced charges and they have the same sign as the original island charges. Every time a charge tunnels the potentials on the leads fluctuate, even when the charge does not originate from or arrive at a lead, because the new charge configuration changes the net induced charge on each lead. The battery restores the leads to their bias values by resetting Q_0 and Q_{N+1} to the values given by Eq. 2.4 and Eq. 2.4.

We separate the work done by the battery from the work done by the charges in our system by introducing a new time scale $t_{battery}$. $t_{battery}$ is the RC time of the external circuit that supplies charge to the source and drain leads. $t_{battery}$ is related to the other orthodox time scales, t_{hop} and t_{relax}, by

$$t_{relax} \ll t_{battery} \ll t_{hop} \; .$$

When a tunneling event between sites i and $i \pm 1$ occurs, the charge configuration changes such that the final charge configuration is given by $Q_i \rightarrow Q_i - e$ and $Q_{i\pm1} \rightarrow Q_{i\pm1} + e$. After the new charge configuration equilibrates the conductors are equipotentials whose values are given by Eq. 2.2.1. t_{relax} characterizes the time for a charge to tunnel and for the system to relax to electrostatic equilibrium. Because $t_{relax} \ll t_{battery}$, the charge states that pertain to the change in energy, $\Delta E = E_f - E_i$, that determine the probability for a tunneling event,

$$\Delta E = \left(\sum_{\alpha=1}^{N+1} Q_\alpha \phi_\alpha \right)_f - \left(\sum_{\beta=1}^{N+1} Q_\beta \phi_\beta \right)_i$$

involve charges that cause the potentials at the source and drain leads, ϕ_0 and ϕ_{N+1}, to deviate away from their applied values, V_0 and V_{N+1}. Because $t_{relax} \ll t_{hop}$, the battery has time to restore the leads to V_0 and V_{N+1} prior to the next tunneling event. Before we recalculate the tunneling rates to determine the next tunneling event, we model the battery by using Eq. 2.4 and Eq. 2.4 to reset the charges on each lead to the values that restore the applied bias potentials. We do not calculate the work done by the battery to recharge the leads because charges do not tunnel between the battery and the leads in this process. The energy needed to restore the potentials is provided by an external circuit that we do not include as a part of our system when we determine the tunneling rates through barriers in the array.

The energy cost of hopping across the i-th junction, ΔE_i, can by found by simplifying Eq. 2.2.1 after substituting into this equation the relationships for the charges on the source and drain (Eq. 2.4 and Eq. 2.4) and the relationship between the charges and potentials at each site (Eq. 2.2.1). In the following form for ΔE_i, we let $e = 1$ and the top (bottom) signs refer to hops to the right (left) between sites $i - 1$ and i:

$$\Delta E_i^{\pm} = E_i^{e-h} \pm \Phi_i$$

where

$$E_i^{e-h} = \frac{1}{2}\left(C_{i,i}^{-1} + C_{i-1,i-1}^{-1}\right) - C_{i,i-1}^{-1}$$

and

$$\Phi_i = \phi_i - \phi_{i-1} \ .$$

We call E_i^{e-h}, the excitonic energy of the i-th junction, because it equals the energy cost of adding an electron and a hole to the pair of sites on either side of the junction. Decreasing the spacing between sites decreases the excitonic energy by decreasing the repulsive terms and increasing the attractive term in Eq. 2.2.1. Φ_i is the potential difference across the i-th junction due to charges on the leads, charges on the islands, and induced charges created by background charged disorder:

$$\Phi_i = \Phi_i^{pol} + \Phi_i^{ch} + \Phi_i^{dis} \ .$$

When all the islands are uncharged and the source and drain leads are biased at potentials, V_0 and V_{N+1}, the leads polarize the charge densities of the surrounding islands while keeping the net charge at each site equal to zero. We call the potential differences across the junctions due to this effect, the polarization potential differences:

$$\begin{aligned} \Phi_i^{pol} &= C_{gen}^2 \left[C_{i0}^{-1} C_{N+1,N+1}^{-1} - C_{i,N+1}^{-1} C_{N+1,0}^{-1} \right] V_0 \\ &+ C_{gen}^2 \left[C_{iN+1}^{-1} C_{00}^{-1} - C_{i0}^{-1} C_{N+1,0}^{-1} \right] V_{N+1} \ . \end{aligned} \tag{2.4}$$

Fig. 2.2 shows how Φ_i^{pol} is distributed over the junctions of an array with 50 islands when the sites are close together ($d/r^{isl} = 0.5$) and far apart ($d/r^{isl} = 10$). This figure shows how this distribution changes when the total applied bias $V = V_0 - V_{N+1}$ is split evenly between the two leads compared to when it is concentrated at one lead. The applied bias V does not drop linearly, i.e. $\Phi^{pol} \neq V/(N+1)$, in either case.

The potential differences across each junction due to the charges on each island are given by

$$\Phi_i^{ch} = \sum_{j=1}^{N} Q_j \left(\tilde{C}_{j,i}^{-1} - \tilde{C}_{j,i-1}^{-1} \right)$$

where

$$\begin{aligned} \tilde{C}_{i,j}^{-1} &= C_{i,j}^{-1} + C_{gen}^2 C_{0,N+1}^{-1} \left(C_{i,N+1}^{-1} C_{j,0}^{-1} + C_{i,0}^{-1} C_{j,N+1}^{-1} \right) \\ &- C_{gen}^2 \left(C_{0,0}^{-1} C_{N+1,i}^{-1} C_{j,N+1}^{-1} + C_{N+1,N+1}^{-1} C_{i,0}^{-1} C_{j,0}^{-1} \right) \ . \end{aligned} \tag{2.5}$$

In Eq. 2.5, the constant C_{gen}^2 is given by Eq. 2.2.1. The modified inverse capacitance matrix, $\tilde{C}_{i,j}^{-1}$, describes how the leads change the potentials created at each site per unit charge at each island. The leads introduce extra potentials at each island that are generated by the directly-induced and indirectly-induced charges on each

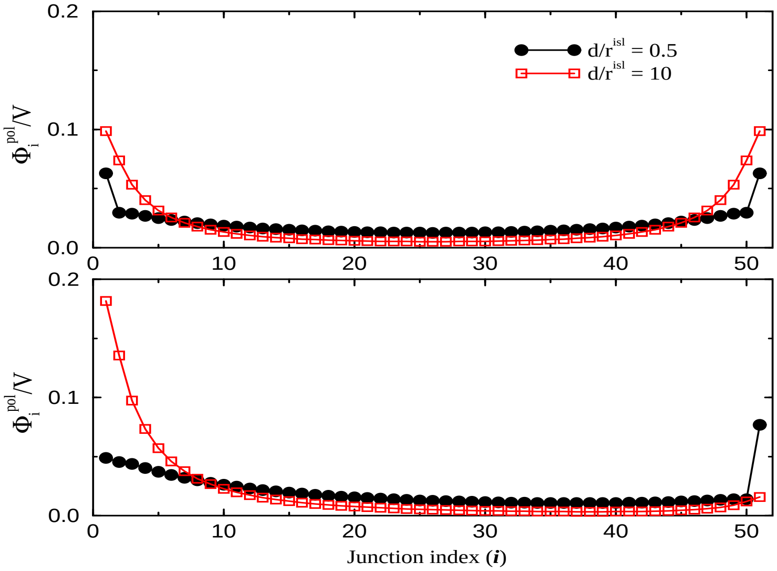

Figure 2.2: *Polarization potential differences, Φ_i^{pol}, across 1-D arrays with 50 islands.* In the top panel, the applied potentials at the source and drain leads equals $V_0 = -V_{N+1} = V/2$. In the bottom panel, the drain is grounded while the source lead potential equals $V_0 = V$. Both panels have the same applied bias difference, $V = V_0 - V_{N+1}$ and each show how modifying the spacing between sites changes how Φ_i^{pol} is distributed over the junctions.

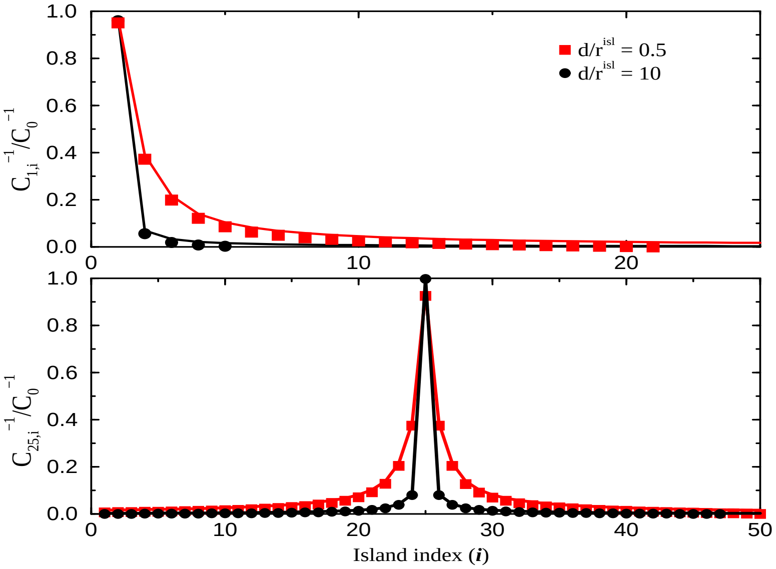

Figure 2.3: *Elements of $C^{-1}_{i,j}$ and $\tilde{C}^{-1}_{i,j}$ for 50-island arrays at two spacings, $d/r^{isl} = 10$ and 0.5.* In both panels, C_0^{-1} is the self inverse capacitance of an isolated island; $C^{-1}_{i,i} = C_0^{-1}$ when interactions among sites are negligible. The top panel plots the rows of C^{-1} and $\tilde{C}^{-1}$ that correspond to the island closest to the source lead. The bottom panel plots the rows that correspond to the islands in the middle of array. The solid lines show C^{-1} and the symbols denote the modified inverse capacitance elements. $\tilde{C}^{-1}$ differs from C^{-1} because it includes the potentials due to induced charges on the leads. These induced charges introduce more screening such that $\tilde{C}^{-1}_{i,j} < C^{-1}_{i,j}$. These differences are small and most noticeable in terms that describe interactions among charges close to the leads.

lead. These induced charges are created by charges on the islands. See Eq. 2.4 and Eq. 2.4. Fig. 2.3 illustrates how induced charges on the leads slightly modify the interactions among charges at the edges and in the middle of an array with 50 islands. The modified inverse capacitance elements do not appear in the definitions of the excitonic energy, E^{e-h}, and the polarization potential gradients, Φ_i^{pol}, because both quantities are associated with the energy costs of arrays in the absence of any excess charges on the nanoparticles. The methods we used to determine the potential differences due to charged disorder, Φ^{dis} are discussed in the following section.

It is important to note that we define Φ_i^{ch} and Φ_i^{pol} such that Φ_i^{ch} depends on the set of charges occupying the islands whereas Φ_i^{pol} does not. The parts of the lead potentials, ϕ_0 and ϕ_{N+1}, that fluctuate as charges move between sites are described by the terms in Φ^{ch} due to the induced charges on the leads. The contributions due to the leads that remain in Φ_i^{pol} are fixed in time so long as the applied potentials, V_0 and V_{N+1}, are unchanged. Separating these dynamic and static contributions to the total potential difference across each junction, Φ_i, enables us to study how these potential gradients are modified by varying the size of the applied bias, $V = V_0 - V_{N+1}$. At large enough V, Coulomb blockade is unimportant and the distribution of potential gradients is set by current conservation which requires that the average currents through every array junction equal the average current through the entire array, I_0. Current conservation leads to a potential difference across each junction proportional to its junction resistance, R_i. Neither Φ_i^{ch} nor Φ_i^{pol} depend directly on the junction resistances, however the time-averaged potential differences due to the island charges, $\langle\Phi_i^{ch}\rangle$, depend on R_i through the orthodox tunneling rates, Eq. 1.3. The tunneling rates are proportional to R_i^{-1}; these rates determine the time-averaged charge, $\langle Q_i\rangle$, at each island which in turn determine $\langle\Phi_i^{ch}\rangle$.

When the applied bias V is too small to overcome Coulomb blockade, the potential differences are independent of the junction resistances. Instead, the potential differences are determined by the electrostatic interactions among the charges occupying the islands and the leads. In this limit, it is important to avoid the assumption that the applied bias V is distributed evenly over the array junctions. Our definitions of Φ_i^{ch} and Φ_i^{pol} enable us to model the potential gradients without this assumption.

2.2.2 Our Model for Disorder

Charged impurities trapped in the substrate underlying the nanoparticle array create random potentials at the nanoparticles. In molecularly assembled arrays, charge transfer to the organic molecules surrounding the nanoparticles results in non-integer random charges at the islands. We include charged disorder in our model using a random potential at each island ϕ_i^{dis}. We characterize clean arrays that have no charged disorder by setting $\phi^{dis} = 0$ for every i. In the case of disordered arrays, the bare disorder potentials due to the charges in the substrate and in the ligands surrounding the nanoparticles can, in principle, take values larger than the charging energy E_c^{isl}. However, charges flow to compensate large fluctuations in the disorder potentials. As a result, the screened disorder potentials are constrained within intervals smaller than $\pm E_c^{isl}$. The size of this interval depends on the interactions among charges; it decreases as the strength and range of Coulomb interactions increases.

We use a variation of the algorithm in [26] to determine the screened disorder potentials. In [26], Kaplan, Sverdlov, and Likharev (2003) use offset charges to model disorder. They find the screened values of the offset charges by numerically modeling the motion of mobile charges that screen out disorder until the entire system relaxes to a global electrostatic equilibrium state. This algorithm was described in Sec. 2.1.2. We use this algorithm to find the set of charges, $\{Q_i^{sc}\}$, that screen out a set of random bare disorder potentials, $\{\phi_i^{dis-bare}\}$, lying within an interval of width, $\pm W$. In each iteration of the annealing algorithm, we add charges to islands and move charges between sites whenever these processes lower the total electrostatic energy of the system. Adding charge to an island decreases the energy of the system when the energy to add a charge to an island, $E_i^{add} < 0$, where

$$E_i^{add,\pm} = \frac{1}{2} C_{i,i}^{-1} \pm \sum_{j=1}^{N} Q_j C_{j,i}^{-1} \pm \phi_i^{dis-bare} \ .$$

The top (bottom) signs refer to the energy to add a positive (negative) charge to an island. Similarly moving charges decreases the energy of the system when $\Delta E_i < 0$:

$$\Delta E_i^{pm} = E_i^{e-h} \pm \Phi_i^{ch} \pm \Phi_i^{dis-bare}$$

where Φ_i^{ch} is given by Eq. 2.2.1 and the potential gradient across a junction due to disorder is given by

$$\Phi_i^{dis-bare} = \phi_i^{dis-bare} - \phi_{i-1}^{dis-bare} \; .$$

The top (bottom) signs in Eq. 2.2.2 correspond to hops to the right (left) between sites $i-1$ and i. Eq. 2.2.2 differs from the more general expression for the hopping energy, Eq. 2.2.1, because it is missing the polarization term, Φ^{pol}. This term is omitted because the leads are grounded, $V_0 = V_{N+1} = 0$, when the system anneals. When adding charge and moving charge no longer decreases the energy of the system, the set of charges that occupy the array islands are the annealed charges, $\{Q^{sc}\}$, we use to define the screened disorder potentials, ϕ_i^{dis}:

$$\phi_i^{dis} = \sum_{j=1}^{N} \tilde{C}_{ij}^{-1} Q_j^{sc} + \phi_i^{dis-bare} \; . \tag{2.6}$$

Following the redefinition of the disorder potentials, we find that the disorder potentials $\{\phi_i^{dis}\}$ and the disorder potential drops $\{\Phi_i^{dis}\}$ between adjacent islands are independent of the interval, $\pm W$, that originally bound the bare disorder values. Instead the values of island disorder potentials and the junction disorder potential gradients are bound by

$$|\phi_i^{dis}| \leq \frac{1}{2} C_{i,i}^{-1} \tag{2.7}$$

$$|\Phi_i^{dis}| \leq E_i^{e-h} \; . \tag{2.8}$$

These bounding values arise from the fact that the total energy of the system is at a global minimum when the original disorder configuration $\{\phi_i^{dis-bare}\}$ is screened out by the charges $\{Q_j^{sc}\}$. While the array is in this state, all charge moves increase the energy of the system:

$$E_i^{add,\pm} \geq 0 \quad (2.9)$$

$$\Delta E_i^{\pm} \geq 0\,. \quad (2.10)$$

Using Eq. 2.2.2, Eq. 2.2.2, and Eq. 2.6, one can simplify the above inequalities and arrive at the inequalities that describe the ranges of the screened disorder values, Eq. 2.7 and Eq. 2.8.

Fig. 2.4(a) and (b) compare $P(\phi_i^{dis})$ and $P(\Phi_i^{dis})$ for arrays with purely onsite interactions,

$$C_{i,j}^{-1,ons} = C_0^{-1}\delta_{i,j}\ ,$$

with arrays with long range interactions ($C_{i\neq j}^{-1} \neq 0$) at two spacings, $d/r^{isl} = 0.5$ and $d/r^{isl} = 10$. In all cases, ϕ_i^{dis} and Φ_i^{dis} are calculated for arrays with 50 islands in between two grounded leads. The histograms average the values of the potentials of all islands and the values of the potential drops between all adjacent islands over many realizations of disorder ($O(> 10^4)$). The smaller spacing, $d/r^{isl} = 0.5$, is typical of chemically assembled nanoparticle arrays. The larger spacing, $d/r^{isl} = 10$, is atypical of arrays in experiments but is included as a pedagogical example because it has interactions among islands that are finite yet comparable to the onsite case that is often used to describe experiments [35, 39, 37, 17].

Fig. 2.4(a) shows how the distributions of disorder potentials , $P(\phi_i^{dis})$, change as the range of interactions increases (d/r^{isl} decreases). In the limit of onsite interactions (Eq. 2.2.2), $P(\phi_i^{dis})$ is a flat distribution because the disorder potentials vary in a purely stochastic way in this case. When interactions extend over several nanoparticles, the disorder potentials do not vary stochastically because Coulomb interactions induce correlations among the potentials. The correlations make it more it more likely for the disorder potentials to have values close to zero. This effect be-

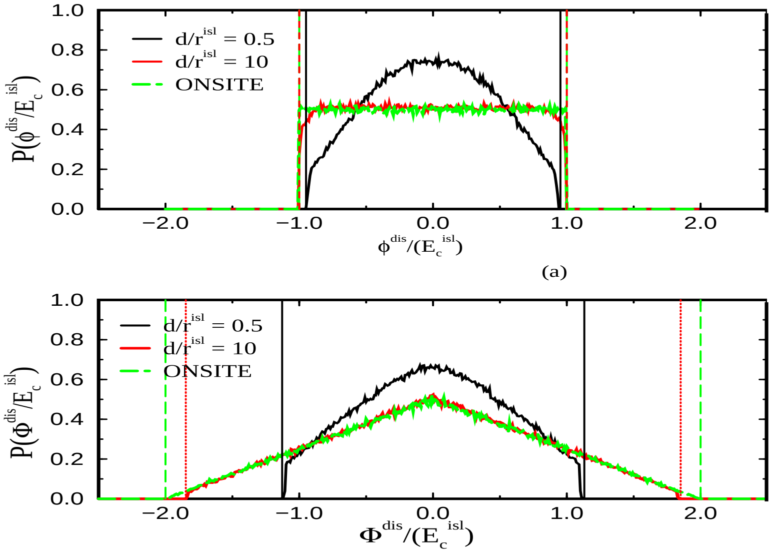

(b)

Figure 2.4: Probability distributions of disorder potentials ϕ^{dis}, (a), and disorder potential differences Φ^{dis}, (b), due to disorder for 50-island arrays with purely onsite coupling and with long range Coulomb coupling at two spacings. $d/r^{isl} = 0.5$ and 10. Vertical lines are included as guidelines to emphasize the edges of the distributions. All potentials are displayed in units of $E_c^{isl} = 1/(2C^0)$.

comes more pronounced as the spacing, d/r^{isl}, between nanoparticles decreases. In addition, decreasing d/r^{isl} decreases the width of distributions according to Eq. 2.7. $P(\phi_i^{dis})$ are bound by $\pm(1/2)C_{i,i}^{-1}$ which is the screened version of $E_c^{isl} = (1/2)C_0^{-1}$. Decreasing d/r^{isl} reduces the cost of adding a single excess charge to an island because induced charges on nearby sites partially screen out the added charge.

Fig. 2.4(b) shows how the distributions of disorder potential gradients, $P(\Phi_i^{dis})$, are modified by Coulomb interactions. Similar to the trends in Fig. 2.4(a), as the spacing between nanoparticles decreases, the width of the distribution decreases and the probability of small (large) $|\Phi_i^{dis}|$ values increases (decreases). The increased probabilities of small $|\Phi_i^{dis}|$ are due to Coulomb correlations that make it more likely for the disorder potentials of neighboring islands to have similar values. Increasing the range of Coulomb interactions leads to a greater reduction in the width of this distribution because the disorder potential gradients are bound by $\pm E_i^{e-h}$ (Eq. 2.8). Whereas the disorder potentials were bound by the energy to add a single charge to an island, the disorder potential gradients are bound by the excitonic cost of creating an electron and a hole on a pair of adjacent islands. When a bare disorder potential gradient exceeds this energy, an electron screens this gradient by hopping across the junction and creating an electron (hole) on the destination (origin) site. Decreasing the spacing decreases E_i^{e-h} because these changes increase screening and increase the attractive term in E_i^{e-h} (Eq. 2.2.1).

Elteto, Antonyan, Nguyen, and Jaeger (2005) analytically characterized the distribution of disorder potential gradients, $P(\Phi_i^{dis})$, using a nearest-neighbor interaction model (Eq. 2.1.2) for the Coulomb interactions [17]. Table 2.1 compares our numerical and their analytical results. Our distributions have the same shape as their distributions in the onsite limit; the onsite distribution is given by Eq. 2.1.2. When long range interactions are included, our results start to diverge. The heights of our distributions ($P(0)$) are in reasonable agreement with $P(0)_{\text{1-D}}$ (Eq. 2.1.2). At the smallest spacing ($d/r^{isl} = 0.5$), the near agreement between our results is surprising because Eq. 2.1.2 is only valid when $\gamma \equiv C_0^{-1}/C^{-1}$ is less than 1/3. When $d/r^{isl} = 0.5$, γ for our 50-island arrays approximately equals, $\gamma \approx 0.412$. At the smallest spacing, our distribution is narrower than their distribution: $E^{e-h} < \Phi_{max}^{dis}$. At this spacing, interactions among particles further apart than nearest neighbors cease to be negligible. See for example $C_{i,j}^{-1}$ for arrays spaced at $d/r^{isl} = 10$ versus $d/r^{isl} = 0.5$ in Fig. 2.3.

In Fig. 2.5, we plot $< \phi_i^{dis} \phi_k^{dis} >$ to illustrate how interactions among charges affect the correlations among disorder potentials. When the potentials are completely uncorrelated, $< \phi_i^{dis} \phi_k^{dis} >$ is finite valued only when $i = k$. This is true for the arrays with only onsite interactions. In the case of long-range interactions with $d/r^{isl} = 0.5$, correlations are maximal when $i = k$, but they do not vanish for $i \neq k$.

d/r^{isl}	E^{e-h}/E_c^{isl}	$\Phi^{dis}_{max}/E_c^{isl}$	$P(0)/(E_c^{isl})^{-1}$	$P(0)_{\text{1-D}}/(E_c^{isl})^{-1}$
onsite	2	2	0.5	0.5
10	1.83332	1.83334	0.51	0.53
0.5	1.10198	1.17581	0.66	0.65

Table 2.1: *Comparison of our distributions, $P(\Phi_i^{dis})$, for 50-island arrays with the equivalent 1-D distributions in [17].* E_i^{e-h} and $P(0)$ were given by the distributions in Fig. 2.4. Φ^{dis}_{max} and $P(0)_{\text{1-D}}$ were calculated using expressions from [17]: Eq. 2.3 and Eq. 2.1.2 with $\gamma \equiv C^{-1}_{24,24}/C^{-1}_{24,25}$. γ equals 0 for onsite arrays and 0.08329 and 0.41206 for arrays with d/r^{isl} equal to 10 and 0.5 respectively. Although the expression used to calculate $P(0)_{\text{1-D}}$ is valid only for $\gamma < 1/3$, our numerical results, $P(0)$, were in reasonable agreement with $P(0)_{\text{1-D}}$ for all cases. The widths of our distributions (E^{e-h}) decrease at a slightly faster rate than Φ^{dis}_{max} as the spacing decreased.

$< \phi_i^{dis}\phi_k^{dis} >$ is finite for at least $|i-k| \leq 3-4$. Correlations of disorder decay faster than the interactions as is seen in the figure. The correlations between ϕ_i^{dis} and its nearest neighbors $\phi_{i\pm1}^{dis}$ make it more likely for the disorder potential differences Φ_i^{dis} to have small magnitudes.

2.3 Conclusions

We developed a model for the Coulomb interactions among charges occupying both the nanoparticles and the biasing leads in nanoparticle arrays. We described these interactions using an inverse capacitance matrix that includes the nanoparticles and the leads. We used this inverse capacitance matrix to derive expressions for the potential gradients across junctions due to the applied potentials at the leads, Φ_i^{pol}, and due to excess charges residing on the nanoparticles, Φ_i^{ch}. See Eq. 2.4 and Eq. 2.2.1. While deriving these expressions, we modeled the leads as non-ideal voltage sources, i.e. we allowed the potentials of the leads to fluctuate away from their applied values in response to changes in the charge configurations on the array. Grouping these induction effects into Φ_i^{ch} led to a renormalized description for the interactions among array charges, Eq. 2.5, that includes the effects of induced charges on the leads created by charges on the nanoparticles.

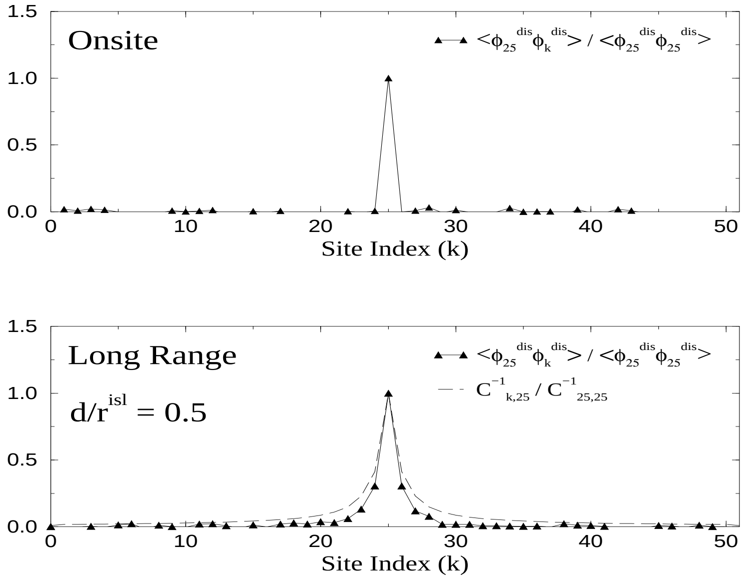

Figure 2.5: Comparison of $< \phi_{25}^{dis}\phi_k^{dis} >$ normalized by $|\phi_{25}^{dis}|^2$ for 50-island arrays with onsite (top plot) versus long range (bottom plot) Coulomb interactions. $C_{k,25}^{-1}$ normalized by $C_{25,25}^{-1}$ is included in the long range case to show that correlations in the disorder potentials are related to, but decay faster than the C^{-1} elements.

We modeled charged disorder by simulating the annealing of the system to a global electrostatic equilibrium state while both leads were grounded. We used the charges associated with this equilibrium state to define the potentials at each nanoparticle due to random charged background disorder, ϕ_i^{dis}. The properties of the global equilibrium state set natural limits on the disorder potentials, ϕ_i^{dis}, and on the disorder potential gradients, Φ_i^{dis}. See Eq. 2.7 and Eq. 2.8. Our description of the Coulomb interactions among the annealing charges led to correlations among the disorder potentials Our probability distributions for the disorder potential gradients across junctions were in reasonable agreements with the distributions calculated analytically by Elteto, et al. [17].

Chapter 3

Threshold Voltage of 1-D Nanoparticle Arrays

Coulomb blockade suppresses the current across nanoparticle arrays at small temperatures and small applied voltages. At zero temperature, no current flows at voltages below a well defined threshold voltage. At small finite temperatures, the threshold is less well defined because the current is finite at all voltages. Disorder and Coulomb interactions complicate how the threshold depends on temperature and the length of the array. Sec. 3.1 discusses several threshold predictions that were made using the models for Coulomb interactions and disorder discussed in Sec. 2.1.

Sec. 3.2 discusses our results for the threshold voltage. To better understand the effects of disorder and long range Coulomb interactions, we determined the thresholds of arrays in the presence and absence of disorder using two different models for Coulomb interactions. In one model (the onsite model), charges only interact if they occupy the same site. This model is easy to understand analytically but does not describe all the interactions that influence charges in actual nanoparticle arrays. The other model (long range model) includes all the interactions among the charges that occupy all the nanoparticles and the biasing leads. The thresholds of arrays described by this model can not be predicted analytically. We found thresholds numerically by simulating the arrays using the orthodox model and a Monte Carlo algorithm and by by defining the threshold as the smallest applied voltage with finite current at zero temperature.

Sec. 3.3 gives a statistical description of how the local energy costs of hopping across junctions of disordered arrays evolve as the applied voltage approaches the threshold. We compare the evolution of distributions of static local potentials for the cases of onsite and long range interactions. This comparison illustrates how long range interactions overcome barriers to current flow due to disorder and large charging energies. Sec. 3.4 discusses how the threshold changes in response to finite temperatures.

3.1 Background

3.1.1 Zero Temperature Threshold

Likharev, Bakhalov, Kazach, and Serdyukova (1989) [32, 10] derived an analytical form for the threshold voltage in the absence of charged disorder:

$$V_T = \frac{e}{2C_{eff}}\left(1 + e^{-1/M}\right) = \frac{e}{C_{eff} + C_0}$$

where M is the soliton length (Eq. 2.1.1) and C_{eff} is the effective capacitance of an infinite periodic 1-D array of capacitors (Eq. 2.1.1 and Fig. 2.1). When the array is symmetrically biased ($V_0 = -V_{N+1} = V/2$), the threshold voltage equals

$$V_S = 2V_T \approx \frac{e}{\sqrt{CC_0}}\ .$$

The approximation in Eq. 2.1.1 is valid when the soliton length is very long ($M \approx \sqrt{C/C_0} \gg 1$) and the array is very long ($N > 2M$). When the array is much longer than the soliton length, the threshold is independent of the array length. In their model, the applied bias potential at each lead penetrates into the array a distance approximately equal to M. As the array length decreases below $N = 2M$, the threshold decreases due to interactions between the source and drain leads. These interactions enable each lead to create potential gradients on the opposite edge of the array that help overcome the costs of adding a new charge to the array.

Middleton and Wingreen (1993) extended Likharev, et al.'s model by adding charged disorder in the form of random offset charges at each nanoparticle [35]. They found that in the limit of very long arrays, the threshold voltage depends linearly on array length, N, in number of nanoparticles for 1-D and 2-D arrays. For 1-D arrays, they found that the thresholds have means,

$$\lim_{N\to\infty} \frac{\langle V_T\rangle}{N(e/C_0)} = \alpha^{MW} = \begin{cases} 1/2 & \text{when } C/C_0 \to 0 \\ M^{-2} \approx (C/C_0)^{-1} & \text{when } C/C_0 \to \infty \end{cases},$$

and rms fluctuations, $\delta V_T \propto N^{1/2}$. In the limit of extremely short range (onsite) interactions ($C/C_0 = 0$), the mean threshold is given by

$$\langle V_T\rangle = (e/C_0)\langle N_{up}\rangle = (e/C_0)(N/2)$$

because the average number of junctions with positive potential gradients (up-steps) due to charged disorder, $\langle N_{up}\rangle$, equals $N/2$. Below the threshold, charges accumulate on the array and create charge gradients, $\delta Q_i = -1$, across junctions that are up-steps. For every charge gradient, a charge must be added to an island at the edge of the array and the cost of adding that charge equals (e/C_0) in the onsite limit. When enough charge gradients build up to compensate for all the up-steps, the next charges that are added to the array create potential gradients that enable charges to tunnel across the entire length of the array. In the opposite limit of extremely long soliton lengths, they argued that $\alpha \approx M^{-2}$ because the maximum static charge density prior to current flow equals e/M^{-2} which corresponds to charges spaced M apart. They numerically determined that α^{MW} goes to 0.1 in the limit of very large soliton lengths.

Jha and Middleton (2005) extended the Middleton and Wingreen model when interactions are short range by including disorder in the sizes of the nanoparticles [24] by letting C_0 vary randomly. They obtained the same relationship for the threshold, Eq. 3.1.1, except that the cost of adding a charge, e/C_0, is replaced by the average cost of adding a charge to islands of varied sizes, $\langle e/C_0 \rangle$. They also found that the rms fluctuations, estimated up to leading order, continue to scale as $\delta V_T \propto N^{1/2}$.

Melsen, Hanke, Muller, and Chao (1997) also used Likharev, et al.'s model for Coulomb interactions (Eq. 2.1.1 and Eq. 2.1.1) and added charged disorder using offset charges [34]. Instead of focusing on the limit of extremely short range interactions, they focused on the case of very large soliton lengths. They found that the average threshold is proportional to $N^{1/2}$ when the soliton length is large compared to the array length, $N < 2.5C/C_0 \approx 2.5M^2$. For smaller soliton lengths, $N > 2.5M^2$, they found that the mean threshold is proportional to N. For all values of the soliton length, they found that the rms fluctuations of the threshold scale with $N^{1/2}$.

$$V_T \propto \begin{cases} N^1/2 & \text{when } N < 2.5C/C_0 \approx 2.5M^2 \\ N & \text{when } N > 2.5C/C_0 \approx 2.5M^2 \end{cases},$$

3.1.2 Finite Temperature Threshold

Elteto, Antonyan, Nguyen, and Jaeger (2005) extended Middleton and Wingreen's (MW) model for the zero temperature threshold to finite temperatures [37, 17].

From this model, they adopted the idea that the threshold is a sum of uniform potential steps, e/C_0, that each overcome an energy barrier due to disorder (an up-step) regardless of the size and position of that barrier. This extended this picture of the threshold that is valid for onsite interactions to the case of interactions of longer range by estimating the threshold in the following way:

$$\langle V_T \rangle = eC_{1,1}^{-1} \langle N_{up} \rangle \; .$$

This is the same as the MW expression, Eq. 3.1.1, except that bare energy for adding a charge to a contact island, eC_0^{-1}, is replaced by the energy of adding a charge to the same island when screening due to neighboring islands is included into the the definition of $C_{1,1}^{-1}$. They argued that raising the temperature decreases the threshold because thermal fluctuations reduce the number of junctions that need to be prepared for current flow with an applied potential. They found that the zero temperature threshold, $V_T(0)$, drops linearly with increasing temperature,

$$V_T(T) = V_T(0) \left(1 - \frac{p(T)}{p_c}\right)$$

where $p(T)$ is the fraction of junctions with small enough energy barriers that thermal fluctuations allow charges to tunnel across these barriers in the absence of a applied potentials. p_c is a critical fraction of junctions that need to be overcome to allow charges to move along a path that spans the array. For 1-D arrays, p_c equals 1; for 2-D arrays, p_c depends on the lattice structure of the array. For square lattices, Middleton and Wingreen found that $p_c = 0.338$ and for triangular lattices, Elteto, et al. found that $p_c = 0.226$ [35, 17]. They estimated $p(T)$ in the following way:

$$p(T) \quad = \quad \int_{-bk_BT}^{bk_BT} P(\Phi^{dis}) d(\Phi^{dis})$$

$$\approx \quad 2bk_BTP(0) \tag{3.1}$$

where $P(\Phi^{dis})$ is the probability distribution of the disorder potential gradients across junctions and bk_BT is the mean energy that charges gain when they hop between occupied and vacant energy states created by finite temperatures. They determined that $b \approx 2.4$. They estimated $P(\Phi^{dis})$ as a flat distribution with a height equal to the value of $P(\Phi^{dis})$ at $\Phi^{dis} = 0$ because $P(\Phi^{dis})$ is nearly flat over the region of temperatures that bring the threshold voltage to zero. They analytically determined the shapes of these distributions using random offset charges and a near neighbor model for the inverse capacitance matrix, Eq. 2.1.2. They found that as interactions increase in strength $P(0)$ increases, Eq. 2.1.2, and $P(\Phi^{dis})$ becomes more flat in this region. We calculated these distributions using inverse capacitance matrices that describe the interactions among all the sites in the array, not just neighboring sites, and our results reasonably agreed with their results. See Table 2.1 and Fig. 2.4.

Cordan, Leroy, Goltzene, Pepin, Vieu, and Launois (2000) studied how temperature affects the thresholds of arrays without charged disorder [9]. They included disorder in the spacings between nanoparticles by varying the resistance of the junctions. They determined the finite temperature threshold numerically using the orthodox model and a definition for the threshold that equals the smallest voltage that makes the current larger than a minimum value that corresponds to a noise threshold. They found that the rate at which the threshold decreases with increasing temperature is sensitive to the resistances of the junctions. Multiple values for the resistances can lead to multiple slopes for $V_T(T)$.

3.2 Zero Temperature Threshold Results

3.2.1 Clean Arrays with Onsite Interactions

In the limit of onsite interactions, we found that the threshold of 1-D arrays with N nanoparticles in the absence of charged disorder ($\Phi^{dis} = 0$) has the following form,

$$V_T = \begin{cases} 2E_c^{isl} N = eC_0^{-1} N & \text{when } N \text{ is odd} \\ 2E_c^{isl}\,(N-1) = eC_0^{-1}(N-1) & \text{when } N \text{ is even} \end{cases} , \tag{3.2}$$

when the array is symmetrically biased such that $V_0 = -V_{N+1} = V/2$. When the length of the array is fixed, we found that varying the biasing asymmetry by distributing the total voltage drop, V, in different ways between the two leads, causes the threshold to fluctuate within an continuous interval defined by the two values for the threshold in Eq. 3.2. This section discusses these two results in detail.

In the limit of onsite interactions, $C_{i,j}^{-1} = 2E_c^{isl}\delta_{i,j}$, the applied bias voltage, $V = V_0 - V_{N+1}$, does not directly affect the bulk junctions (junctions between neighboring islands) because the bias potentials, V_0 and V_{N+1}, do not extend beyond the leads. The potential gradients across the array junctions due to these potentials are given by

$$\Phi_i^{pol} = \phi_i^{pol} - \phi_{i-1}^{pol} = \begin{cases} -\alpha V & \text{when i = 1} \\ (\alpha - 1)V & \text{when i = N+1} \\ 0 & \text{otherwise} \end{cases} .$$

Φ_i^{pol} is only finite across the junctions in between the islands at the edges of the array and the leads (contact junctions). α is a biasing asymmetry factor that varies between 0 and 1; it equals 1/2 when the array is symmetrically biased and 1 (0) when the applied bias potential is concentrated at the source (drain) lead. Although $\Phi_i^{pol} = 0$ across all bulk junctions, the applied bias voltage indirectly affects these junctions by injecting charges across one or both of the contact junctions. These charges accumulate on the array and create potential gradients across the bulk and contact junctions. Eventually, increasing the bias voltage allows enough charges to build up on the array that the next injected charge(s) are able to tunnel across all the array junctions. The threshold voltage occurs at this minimum voltage that allows charge transfer between the two leads.

The value of the threshold voltage and the charge state of the array at this value can be determined by studying the energy costs for hopping across the bulk junctions and the contact junctions. The energy costs for hopping across the bulk junctions equal

$$\begin{aligned}\Delta E_i &= E_i^{e-h} + \Phi_i^{ch} \\ &= 2E_c^{isl}\left(1 + \delta Q_i\right) \ , \end{aligned} \tag{3.3}$$

where $\delta Q_i = Q_i - Q_{i-1}$ is the charge gradient across the junction. Onsite interactions simplify the excitonic energy, E_i^{e-h}, and the potential gradient across each junction due to charges on the array, Φ_i^{ch} , because the potentials due to all charges do not extend beyond the sites that the charges occupy. The general forms for E_i^{e-h} and Φ_i^{ch} are given by Eq. 2.2.1 and Eq. 2.2.1 respectively. The energy costs of tunneling across the contact junctions next to the source and drain leads equal

$$\begin{aligned}\Delta E_1 &= E_1^{e-h} + \Phi_1^{pol} + \Phi_1^{ch} \\ &\approx E_c^{isl}\left(1 - \alpha V + 2Q_1\right) \end{aligned} \tag{3.4}$$

$$\begin{aligned}\Delta E_{N+1} &= E_{N+1}^{e-h} + \Phi_{N+1}^{pol} + \Phi_{N+1}^{ch} \\ &\approx E_c^{isl}\left(1 + (\alpha - 1)V - 2Q_N\right) \end{aligned} \tag{3.5}$$

respectively. In Eq. 3.4 and Eq. 3.5, the approximations arise from assuming that the self inverse capacitances of the leads approximately equal zero, $C_{0,0}^{-1} = C_{N+1,N+1}^{-1} \approx 0$. These terms add a very small contribution to the equations when the leads are much larger than the nanoparticles. [1] These terms are omitted to simplify the discussion in this section.

When the array is unbiased, the numbers of excess charges at each island equal zero and δQ_i equals 0 across all bulk junctions. When the applied bias becomes large enough to inject a charge across one or both of the contact junctions, the charge gradient(s) across the bulk junction(s) next to the contact junction(s) decrease to -1. At zero temperature, this charge gradient is too small to allow the inject charge(s) to penetrate further into the array because the energy to hop across the bulk junctions equals 0 when $\delta Q = -1$ (see Eq. 3.3 and Eq. 1.2). In nearly all cases, current can not flow until enough charges accumulate at the contact islands, Q_1 and Q_N, such that the charge gradients across all bulk junctions equal -1. In this case, the next charges that are injected across the contact junctions modify the charge gradients across each bulk junction to values ($\delta Q_i = -2$) that allow a single net charge to tunnel across each bulk junction. The exception to this rule occurs at threshold voltages that allow two charges of opposite sign to enter the array, one from each lead, and meet somewhere in the middle of the array at the islands on either side of a bulk junction. The charge gradient created by these two charges equals $\delta Q_i = -2$ prior to prepping this bulk junction with a charge gradient $\delta Q_i = -1$. In this case, current flows when all but one bulk junction is prepared for current flow by an accumulated charge gradient, $\delta Q_i = -1$. As a result of these two cases, the relationship between the charges on the islands closest to the leads at the threshold voltage is given by

$$Q_1 - Q_N = -\sum_{i=2}^{N} \delta Q_i = \begin{cases} N_{bulk} = N - 1 & \text{when } N \text{ is odd} \\ N_{bulk} - 1 = N - 2 & \text{when } N \text{ is even} \end{cases}$$

---

[1] Numerically, we used the exact values for these terms when the radii of the leads, R_{lead}, and the nanoparticles, r_{isl}, are related by $R_{lead} = 50 r_{isl}$. In this case, $C^{-1}_{0,0} = C^{-1}_{N+1,N+1} = (0.02)(2E_c^{isl})$ where $2E_c^{isl} = e^2 C_0^{-1}$ equals the self inverse capacitance elements that correspond to the nanoparticles.

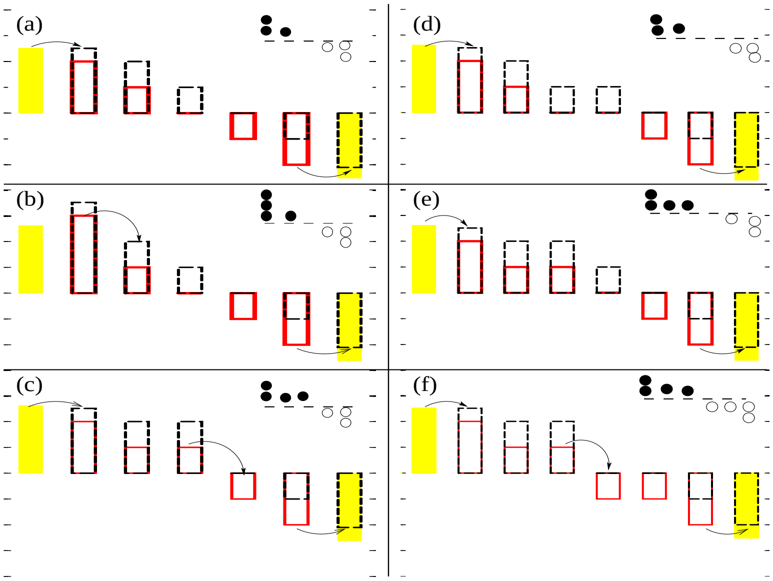

Figure 3.1: Potentials and charges at sites in two arrays of different length ($N = 5$ and $N = 6$) at voltages just above the threshold. The filled bars, unfilled bars with solid borders, and unfilled bars with dashed borders represent the polarization potential, the total potential, and the total potential plus the excitonic energy respectively. The last quantity equals the potential seen at a site by a charge tunneling to the right unto that site. The arrows indicate possible tunneling events. The tick marks are spaced $2E_c^{isl}$ units apart. The insets show the charge at each island for each set of potentials. Filled (unfilled) circles represent positive (negative) charges.

when the array is symmetrically biased. These values along with $\Delta E_1 = \Delta E_{N+1} = 0$ in Eq. 3.4 and Eq. 3.5 simplify to the threshold voltages given in Eq. 3.2. Fig. 3.1 illustrates these two cases.

These two cases also affect the value of the threshold when the biasing asymmetry factor, α, is varied while the array length in number of nanoparticles, N, is fixed. The threshold dependence of the threshold on α is given by $V_T = \min(V_S, V_D)$ where

$$V_S = E_c^{isl}(2Q_1 + 1)/\alpha \tag{3.6}$$

$$V_D = E_c^{isl}(2Q_N - 1)/(\alpha - 1) \ . \tag{3.7}$$

Eq. 3.6 and Eq. 3.7 equal the threshold voltage when current carrying sequences of tunneling events begin with single charges entering the array from the source and the drain respectively. As the biasing asymmetry is varied, the threshold voltage is alternately determined by the cost of injecting a charge unto the array from the source and the drain and the threshold values vary continuously between maximum and minimum values equal to the values in Eq. 3.2. The minimum value for the threshold is due to the entrance of two charges of opposite sign from the two leads meeting in the middle of the array; this is the same process that made the thresholds of arrays with even numbers of nanoparticles smaller than their odd-numbered counterparts when the array was symmetrically biased. At all other values of the threshold shown in Fig. 3.2, one charge from one lead starts each sequence of tunneling events that transfer charge between the leads at the threshold voltage. When the inverse self capacitance of the leads is negligible, the intervals in terms of α between adjacent minimum and maximum thresholds are given by N^{-1} and $(N-1)^{-1}$ respectively.

Fig. 3.3 shows how the threshold varies with array length for several values of α. When the array is symmetrically biased ($\alpha = 1/2$), the threshold voltage has a dependence on N that resembles a staircase due to the two cases in Eq. 3.2. When the bias voltage is completed distributed on one lead ($\alpha = 0$ or $\alpha = 1$), the differences between arrays with even and odd numbers of islands disappear because charges can only enter the array from one lead at the threshold voltage. At intermediate values of α between the symmetric and completely asymmetric cases, the threshold dependence on N again has linear regions and flat regions but these are spaced differently than similar regions in the symmetric case. For all values of α, the lines that pass through the thresholds when they increase linearly with N have slopes equal to $(2E_c^{isl})\alpha^{-1}$. The flat regions are due to arrays that differ in length by one nanoparticle; the longer length has a threshold value determined by

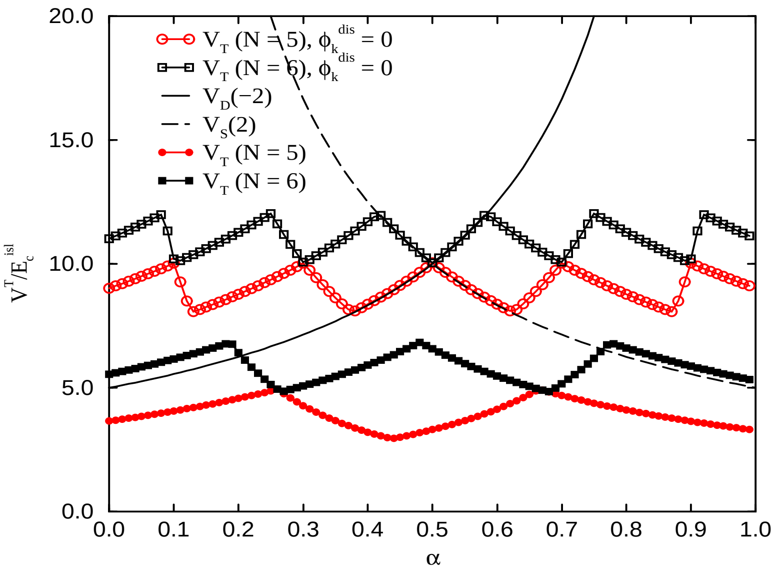

Figure 3.2: *Threshold voltage of arrays in the limit of onsite interactions as a function of the biasing asymmetry factor, α.* The open (closed) symbols correspond to the thresholds of arrays without (with) charged disorder. The V_S and V_D curves are examples of the family of curves described by Eq. 3.6 and Eq. 3.7 that make up the threshold relationships for arrays without disorder.

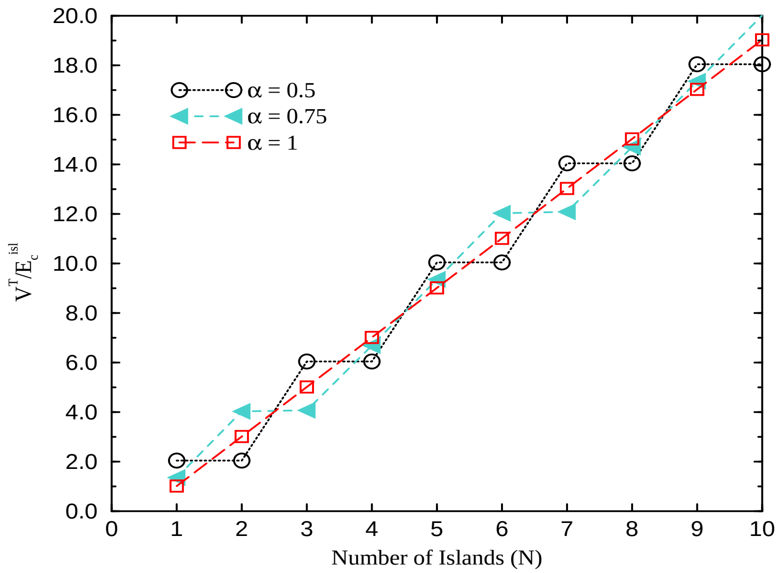

Figure 3.3: *Threshold voltage of clean arrays with onsite interactions as a function of array length, N, for several values of the biasing asymmetry factor, α.*

the entrance of two charges of opposite sign from the two leads.

3.2.2 Clean Arrays with Long Range Interactions

When interactions among sites are long range, we found that no charges need to accumulate on the array prior to flow of current when there is no charged disorder ($\Phi_i^{dis} = 0$). The threshold voltage occurs at the minimum voltage that allows a charge to tunnel across one of the contact junctions. When the surface-to-surface distance between adjacent nanoparticles, d, is not very large compared to the radii of the nanoparticles, r_{isl}, the threshold increases as the array length in numbers of nanoparticles, N, increases. When N is very large, decreasing the spacing between nanoparticles increases the threshold. This section discusses in more detail how the threshold of arrays with long range interactions vary with respect to N and d/r^{isl} in the absence of disorder.

Prior to the entrance of any excess charge into the array, the energies to tunnel across all array junctions are given by

$$\Delta E_i = E_i^{e-h} + \Phi_i^{pol} = E_i^{e-h} + \Lambda_i V$$

with the excitonic energy, E_i^{e-h}, given by Eq. 2.2.1 and $\Lambda_i = \Phi_i^{pol}/V$ given by

$$\Lambda_i = \frac{\alpha\left(C_{i,0}^{-1}C_{N+1,N+1}^{-1} - C_{i,N+1}^{-1}C_{N+1,0}^{-1}\right) + (\alpha-1)\left(C_{i,N+1}^{-1}C_{0,0}^{-1} - C_{i,0}^{-1}C_{N+1,0}^{-1}\right)}{C_{0,0}^{-1}C_{N+1,N+1}^{-1} - (C_{N+1,0}^{-1})^2} \ . \quad (3.8)$$

By setting Eq. 3.2.2 equal to zero, one can define a local threshold, V_i^{Th}, for each junction equal to the minimum applied bias voltage V that enables a charge to hop across each junction when it is uncharged,

$$V_i^{Th} = -\frac{E_i^{e-h}}{\Lambda_i} \ .$$

V_i^{Th} tends to be smallest across one of the contact junctions because the fraction of the total applied bias that drops across each junction, $|\Lambda_i|$, tends to be the largest at either of the contact junctions. In the long range case, once a charge hops across one of the contact junctions a net charge can move between the two leads because the polarization potential gradient, Φ_i^{pol}, is negative across all array junctions; this potential drop allows the injected charge to move across all the junctions in the array. In this case, the array threshold equals the minimum local threshold,

$$V_T = \min\left(V_i^{Th}\right) \ .$$

Eq. 3.2.2 was not valid in the case discussed in the previous section because there are no polarization potential drops to facilitate charge flow across the bulk junctions when interactions only occur among charges that occupy the same site.

Fig. 3.4(a) shows how the threshold relates to array length, N, at several different array spacings, $d/r^{isl} = 0.5, 1, 10$, when the array is symmetrically biased

($\alpha = 1/2$ in Eq. 3.8). All the threshold values in this figure correspond to the local threshold, V^{Th}, of a contact junction. The symbols indicate thresholds we determined numerically. The dotted lines are analytical estimates of these thresholds calculated using Eq. 3.2.2, Eq. 2.2.1, and Eq. 3.8 with $C_{i,j}^{-1} \approx (2E_c^{isl})d_{ij}^{-1}$ where d_{ij} is the center-to-center distance between spheres i and j. [2] For a given spacing, the main source of variation in V_T when N is varied is the fraction of the polarization potential that drops across either contact junction, $|\Lambda_1| = |\Lambda_{N+1}|$. As the separation between the leads increases (increasing N), the fraction of the polarization potential that drops across the contact junctions decreases and as a result the threshold increases according to Eq. 3.2.2. $|\Lambda_1|$ and $|\Lambda_{N+1}|$ stop decreasing with increasing distance between the leads when this distance becomes large enough that the interactions between the leads are negligible. This is why the threshold values of the arrays with the largest spacing ($d/r^{isl} = 10$) shown in Fig. 3.4(a) begin to saturate with increasing N. Due to the same reason, the threshold values of the arrays with the smaller spacings ($d/r^{isl} = 0.5$ and 1) in the figure eventually saturate at values of N larger than the ones shown in this figure. Likharev, et al. [32] predicted that the threshold of arrays without disorder are independent of N when N is large compared to the soliton length, $N > 2M$. Table 3.1 shows estimates of the values predicted by Likharev, et al. (Eq. 3.1.1) that correspond to the spacings shown in Fig. 3.4. Our thresholds are larger than these predicted values and they continue to increase with N when $N > 2M$. Qualitatively, our results agree because eventually our thresholds become independent of N and these values decrease as the spacings between islands increase.

Fig. 3.4(b) shows how the clean threshold varies with array spacing for sev-

---

[2] This approximation is close to the actual value of threshold in this case because it is a function of inverse capacitance elements that involve that leads. The leads are large enough that their inverse capacitance elements, $\{C_{i,0}^{-1}\}$ and $\{C_{i,N+1}^{-1}\}$, approximately equal the unscreened potentials due to unit charges located at their centers when the leads are far enough apart that their screening of each other's potentials does not significantly alter $\{C_{i,0}^{-1}\}$ and $\{C_{i,N+1}^{-1}\}$.

d/r^{isl}	$C^{-1}_{25,25}$	M	$V_S/E^{isl}_c \approx 2C^{-1}_{eff}(1+\exp(-M^{-1}))$
10	0.999	0.42	2.18
1	0.970	1.1	2.70
0.5	0.937	1.4	2.72

Table 3.1: *Estimates of thresholds predicted by Likharev, et al. [32] for arrays with no disorder.* These values were calculated using $V_S = 2V_T$ where V_T is given by Eq. 3.1.1 with $C^{-1}_{eff} \approx C^{-1}_{25,25}$ and M extracted from rows of our inverse capacitance matrices that correspond to islands in the middle of long arrays. See Fig. 3.5. Likharev, et al. predicted that symmetrically biased arrays without disorder would have thresholds that are independent of N given by V_S when $N > 2M$. Although the arrays in Fig. 3.4 are long enough that $N > 2M$, the thresholds continue to increase with N and are larger than the values tabulated here. Qualitatively, our results agree because the thresholds eventually saturate at large enough N to values that like V_S increase with decreasing spacing.

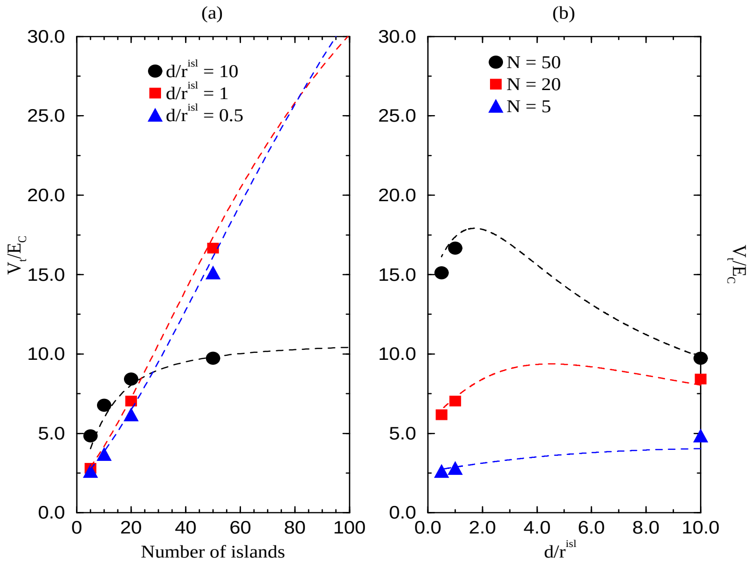

Figure 3.4: Threshold of symmetrically biased arrays, V_T, with no disorder as a function of number of islands, N, and of array spacing, d/r^{isl}. The dashed lines are estimates of the threshold that use a r^{-1} model to approximate the polarization potential drops across the contact junctions, Λ_1 and Λ_{N+1}.

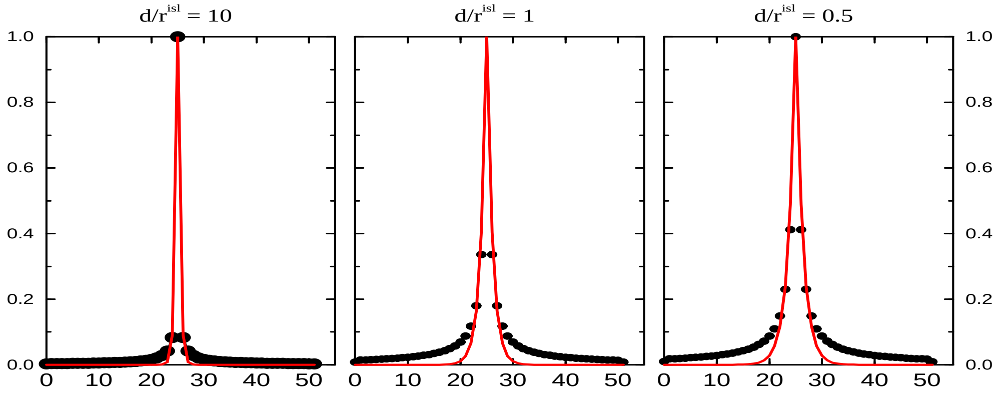

Figure 3.5: $C^{-1}_{25,i}/C^{-1}_{25,25}$ *for 50-island arrays spaced at* $d/r^{isl} = 0.5, 1$ *and 10.* The closed circles show our numerical results for these inverse capacitance elements. The solid lines show fits of the soliton form, $y = \exp(-|25-x|M^{-1})$, where $M^{-1} =$ 0.716, 0.906, and 2.407 for spacings, $d/r^{isl} = 0.5$, 1, and 10 respectively. These correspond to $M \approx 1.4$, 1.1, and 0.42 for the same spacings. Our inverse capacitance matrices do not conform to the soliton shape for $C^{-1}_{i,j}$, Eq. 2.1.1, because our matrices are the inverses of fully populated capacitance matrices, not the tridiagonal matrices (Eq. 2.1.1) used to derive the soliton form for $C^{-1}_{i,j}$.

eral array lengths. In the limit of extremely large array spacings, the polarization potential drops are concentrated at the contact junctions. As the spacing decreases, the polarization potential drops tend to be more homogeneously distributed over more array junctions. As a result, decreasing the array spacing tends to decrease the polarization potential drops across the contact junctions and therefore increase the threshold voltage according to Eq. 3.2.2. When the distance between the opposing leads becomes small enough that each lead significantly contributes to the polarization potential drop across the contact junction on the other side of the array, decreasing d/r^{isl} increases the polarization potential drops across the contact junctions and the threshold decreases according to Eq. 3.2.2. Thus, the positive (negative) correlations between the threshold and the array spacing shown in Fig. 3.4(b) are due to dependence of Eq. 3.2.2 on array spacing in the presence (absence) of significant interactions between the opposing leads.

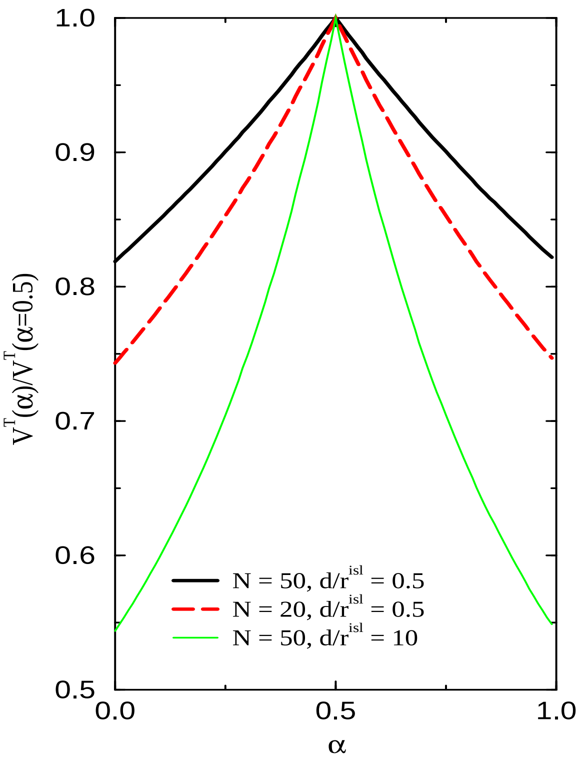

Figure 3.6: *Threshold voltage of clean arrays with long range Coulomb interactions as a function of* α*.*

Varying the biasing asymmetry factor, α, of arrays with long range interactions does not cause the threshold to fluctuate up and down as it did for arrays with onsite interactions. Instead, increasing the asymmetry between the leads (increasing $|1/2 - \alpha|$) always decreases the threshold by increasing the amount of the applied bias that drops across the contact junction that sets the threshold. Fig. 3.6 shows how varying the biasing symmetry, α, modifies the threshold of a few arrays of varied length and spacing.

3.2.3 Disordered Arrays with Onsite Interactions

Charged disorder complicates the threshold voltage by introducing a random potential difference to each bulk junction, Φ_i^{dis}. In the limit of onsite interactions, we found in agreement with Middleton and Wingreen, Ref. [35], that the average threshold equals

$$\langle V_T \rangle = (eC_0^{-1})\langle N_{up} \rangle = (2E_c^{isl})(N/2)$$

where the average is over many configurations of disorder and N_{up} is the number of bulk junctions with non-negative disorder potential differences, $\Phi^{dis} \geq 0$. For an array with a specific configuration of disorder, we found that modifying the biasing asymmetry factor, α, causes the threshold to fluctuate between two values. Similar to the case of arrays without disorder, this range of values is due to the dependence of the threshold on α and on two possibilities for the net excess charge on the array at the threshold voltage,

$$Q_1 - Q_N = -\sum_{i=2}^{N} \delta Q_i = \begin{cases} N_{up} & \text{or} \\ N_{up} - 1 & \end{cases} .$$

In Eq. 3.2.3, the net charge gradient is a sum over charge gradients across bulk junctions with values equal to

$$\delta Q_i = \begin{cases} -1 & \text{when } \Phi_i^{dis} \geq 0 \\ 0 & \text{when } \Phi_i^{dis} < 0 \end{cases} .$$

The smaller value for the total charge gradient in Eq. 3.2.3 is allowed when two injected charges of opposite sign meet at a junction with an up-step and create a potential gradient that allows charge to tunnel across that junction. Thus, the two injected charges eliminate the need for accumulated charges to prepare one bulk junction for current flow with a charge gradient, $\delta Q_i = -1$.

Fig. 3.2 shows how varying the biasing asymmetry factor, α, affects the thresholds of arrays with and without disorder. Similar to the clean case, the threshold dependence on α for disordered arrays is given by $\min\left(V_S^{dis}, V_D^{dis}\right)$ where

$$\begin{aligned} V_S &= E_c^{isl}(2Q_1 + \phi_1^{dis} + 1)/\alpha \qquad (3.9) \\ V_D &= E_c^{isl}(2Q_N + \phi_N^{dis} - 1)/(\alpha - 1)\ . \qquad (3.10) \end{aligned}$$

ϕ_1^{dis} and ϕ_N^{dis} are the potentials due to disorder at each contact island and Q_1 and Q_N are the charges on the contact islands given by Eq. 3.2.3. Compared to the clean arrays, the threshold curves, $V_T(\alpha)$, of the disordered array have smaller values and less peaks because the disordered arrays have less bulk junctions that require negative charge gradients, $\delta Q_i = -1$, to prepare them for current flow. This tends to be true for any given configuration of disorder because the number of up-steps (junctions with $\Phi^{dis} \geq 0$) tends to be less than the number of bulk junctions.

Fig. 3.7 shows how the mean values and rms fluctuations of the thresholds averaged over many configurations of disorder vary with array length. The cost of overcoming the mean number of up-steps, $N_{bulk}/2$, along with the cost of charging the contact junctions leads to the mean threshold dependence in Eq. 3.2.3. This agrees with Middleton and Wingreen's threshold results for arrays with onsite interactions [35]. The inset of Fig. 3.7 shows that we also recovered Middleton and Wingreen's results for the rms fluctuations of the threshold, $\delta V_T \propto N^{1/2}$. This dependence is the same as the rms fluctuations of a 1-D random walk because the number of up-steps varies stochastically [24].

3.2.4 Disordered Arrays with Long Range Interactions

We numerically found that the average threshold voltage of arrays with charged disorder continues to vary linearly with respect to array length when charges interact via long range Coulomb interactions. Fig. 3.8 plots the means of the thresholds for

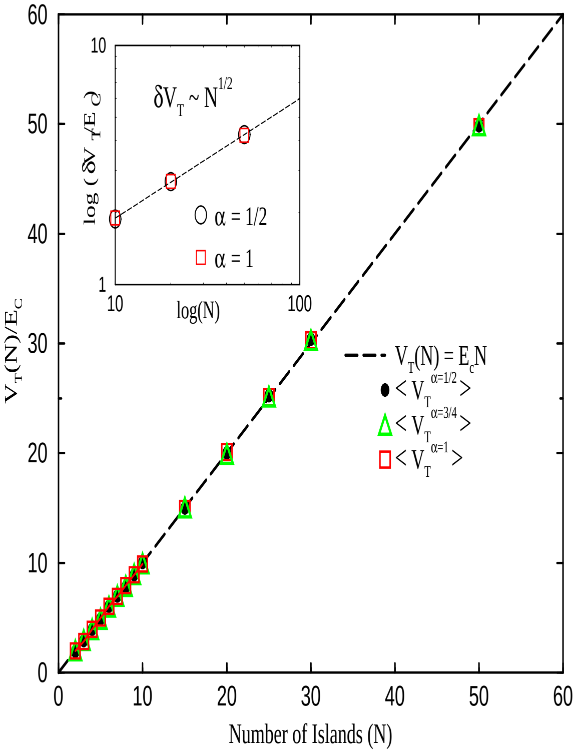

Figure 3.7: *Means and rms fluctuations of the thresholds of disordered arrays with onsite interactions.*

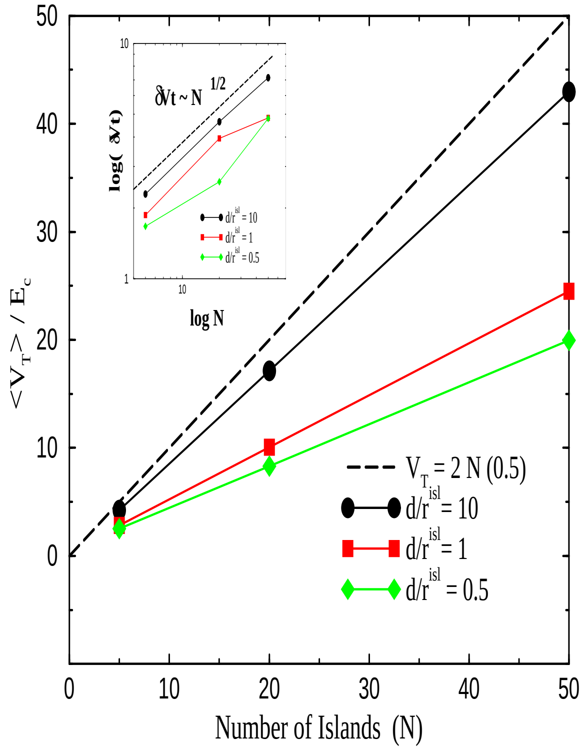

Figure 3.8: *Average threshold,* $\langle V_T \rangle$ *of disordered arrays versus array length,* N*, at three different array spacings,* $d/r^{isl} = 10, 1$ *and 0.5.* The inset displays the rms fluctuations, δV_T, of the threshold. The dashed line in each graph shows how $\langle V_T \rangle$ and δV_T depend on N in the limit of onsite interactions.

arrays at different spacings, $d/r^{isl} = 10, 1$ and 0.5. Decreasing the spacing (d/r^{isl}) between sites decreases the rate at which the threshold changes with respect to increasing array length. The inset of this figure plots the rms fluctuations, δV_T, of the thresholds at the three spacings. At the largest spacing, $d/r^{isl} = 10$, interactions among distant charges are minimal and δV_T depends on N like a 1-D random walk. At the smaller spacings, stronger interactions among distant charges cause the rms fluctuations to deviate away from the random walk relationship.

The exact thresholds of disordered arrays with long range interactions can not be analytically predicted because interactions complicate how the potential gradients across junctions respond to variations in the applied bias. The applied bias can modify these potential differences directly through the polarization potential gradients, Φ_i^{pol}, and indirectly by injecting charges on the array that create potential gradients across the junctions, Φ_i^{ch}. An upper limit for the threshold can be estimated by making an analogy to the onsite case. Similar to the onsite case, the applied voltage prepares the array junctions for current flow by adjusting Φ_i^{pol} and Φ_i^{ch} until the energy cost to hop across one junction is less than zero while the energy costs to tunnel across the rest of the junctions lie between 0 and $|\Phi_i^{add}|$,

$$0 \leq \Delta E_i \leq |\Phi_i^{add}|$$

$\Phi^{add} < 0$ describes an additional potential drop that occurs across junctions when injected charge(s)s approach the junctions. Φ^{add} can be conservatively estimated by assuming that only one injected charge modifies the potential gradients across any one junction. The effect of this charge on any junction is greatest when the charge arrives at the junction. At this point, its potential difference is given by

$$\begin{aligned} \Phi_i^{add} &= \sum_{j=1}^{N} \delta_{j,i} \left(\tilde{C}_{j,i}^{-1} - \tilde{C}_{j,i-1}^{-1} \right) \\ &= \tilde{C}_{i,i}^{-1} - \tilde{C}_{i,i-1}^{-1} \qquad (3.11) \\ &\approx -E_i^{e-h} \ . \end{aligned}$$

The approximation in Eq. 3.11 was made by using Eq. 2.2.1 and assuming that $\tilde{C}_{i,j}^{-1} \approx C_{i,j}^{-1}$ [3]. At zero applied bias, the energies to hop across down-steps and up-steps fall within the following ranges,

---

[3] The renormalized inverse capacitance matrix includes the screening of Coulomb interactions due to charges induced on the leads by charges on the array. The excitonic energy (by definition) does not include these effects because it is the energy of charging a junction in the absence of any charge on the array.

$$\begin{aligned} 0 &\leq \Delta E_i < E_i^{e-h} &\quad \text{when } \Phi_i^{dis} < 0 \\ E_i^{e-h} &\leq \Delta E_i \leq 2E_i^{e-h} &\quad \text{when } \Phi_i^{dis} \geq 0 \,. \end{aligned} \tag{3.12}$$

To bring these energies within a range, Eq. 3.2.4 and Eq. 3.11, that enables the next injected charges to hop in sequences that transfer charge between the leads, the applied bias voltage, V, can create the following the potential gradients across the junctions

$$\Phi_i^{ch} + \Phi_i^{pol} = \begin{cases} 0 & \text{when } \Phi_i^{dis} < 0 \\ -E_i^{e-h} & \text{when } \Phi_i^{dis} \geq 0 \end{cases} .$$

Because $V = V_0 - V_{N+1} = \sum_{i=1}^{N+1} \left(\Phi_i^{ch} + \Phi_i^{pol}\right)$ at all applied voltages [4] , Eq. 3.2.4 can be used to estimate the threshold:

$$\begin{aligned} \sum_{i=1}^{N+1} \left(\Phi_i^{ch} + \Phi_i^{pol}\right) &= -N_{up}(E_i^{e-h}) = -V_T \\ \Rightarrow < V_T > &\approx (N/2) < E_i^{e-h} > \,. \end{aligned} \tag{3.13}$$

Table 3.2 compares this estimate for the threshold with our numerical results for $\langle V_T(N) \rangle$ shown in Fig. 3.8 and two other estimates for the threshold: the long soliton length estimate for the threshold,Eq. 3.1.1, given by Middleton and Wingreen [35] and the near-neighbor estimate for the threshold, Eq. 3.1.2, by Elteto, et al. [17]. Our numerical results for $\langle V_T(N) \rangle$ are the smaller than all these estimates and closest to Eq. 3.13.

Fig. 3.9 compares our numerical results for $\langle V_T(N) \rangle$ to thresholds measured in experiments with 1-D and quasi-1-D arrays. The numerical results for arrays

---

[4] This statement is true because adding the applied potential gradient across each junction to the potential at one edge of the array, V_0, gives the value of the applied potential at the opposite edge of the array, V_{N+1}, i.e. $V_0 + \sum_{i=1}^{N+1} \left(\Phi_i^{ch} + \Phi_i^{pol}\right) = V_{N+1}$.

d/r^{isl}	Numerical Slope of $\langle V_T(N)\rangle$	$\langle E^{e-h}/2\rangle$	$C^{-1}_{25,25}/2$	$\alpha^{MW} \approx M^{-2}$
10	0.86	0.90	1.00	11.59
1	0.49	0.64	0.97	11.64
0.5	0.40	0.55	0.94	1.02

Table 3.2: *Comparison of slopes of* $\langle V_T(N)/E_c^{isl}\rangle$ *for disordered arrays at several spacings,* $d/r^{isl} = 10, 1, 0.5$. The numerical slopes are the slopes of the linear fits to our numerical results in Fig. 3.8. $\langle E^{e-h}/2\rangle$ is from an estimate, Eq. 3.13, for the threshold that approximates the energy to overcome junctions with $\Phi_i^{dis} \geq 0$ as E_i^{e-h}. $C^{-1}_{25,25}$ is from the estimate made by Elteto, et al. to extend the MW onsite threshold to include interactions among neighboring nanoparticles, Eq. 3.1.2. α^{MW} was the form predicted by Middleton and Wingreen (1993) [35] in the limit of large soliton lengths. Fig. 3.5 shows how the soliton lengths, M, were extracted from our inverse capacitance matrices. M^{-2} is greater than the maximum value for $\alpha^{MW} = 1$ (in units of $E_c^{isl} = 0.5eC_0^{-1}$) at all the spacings. At all spacings, the soliton lengths are too short for the large M estimates to be valid and too long to be described by the onsite value, $\alpha^{MW} = 1$.

with spacings comparable to spacings in experiments, $d/r^{isl} = 0.5$, are in reasonable agreement with experimental measurements of the threshold on 1-D arrays. Our numerical results overestimate the thresholds of quasi-1-D arrays. It is possible for the thresholds of quasi-1-D arrays to be smaller than the thresholds of 1-D arrays because charges can access pathways in these arrays that are absent in the 1-D case that enable them to avoid some barriers to current flow.

Fig. 3.10 shows how the threshold of 50-island arrays with different spacings, $d/r^{isl} = 0.5$ and 10, respond to varying the way the applied voltage is distributed between the two leads. The threshold curves, $V_T(\alpha)$, for the disordered arrays have more peaks than the equivalent curves for the arrays without disorder. The arrays without disorder vary smoothly as the asymmetry increases (increasing $|\alpha - 1/2|$) because the threshold of these arrays is only determined by a single type of process, a charge hop from a lead to a site at the edge of the array when no excess charges reside at any nanoparticle of the array. The irregular features in $V_T(\alpha)$ for the disordered arrays are due to multiple processes. Varying α can change the set of charges that accumulate on the arrays below threshold and also change the position

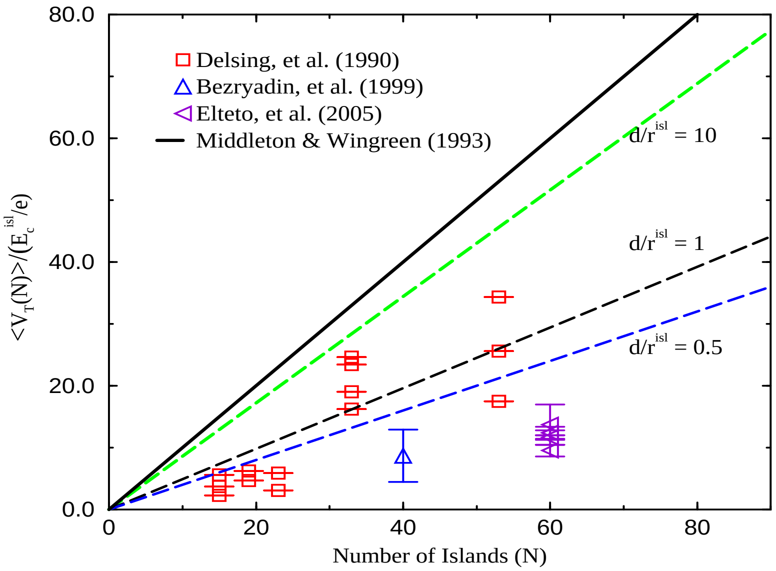

Figure 3.9: *Comparison of Zero Temperature Threshold Results.* The threshold results of Delsing, et al. (1990) et al., Bezryadin, et al. [4], Elteto, et al. [17] were rescaled by $E_c^{isl} = e/(2C_0)$ equal to 0.3 meV, 0.05 eV, and 0.26 eV respectively. The dashed lines represent our results for arrays at different spacings, $d/r^{isl} = 0.5, 1$, and 10. The Delsing, et al. results compare well with our results because they measure thresholds on 1-D arrays whereas Bezryadin, et al. and Elteto, et al. measured the thresholds of quasi-1-D arrays.

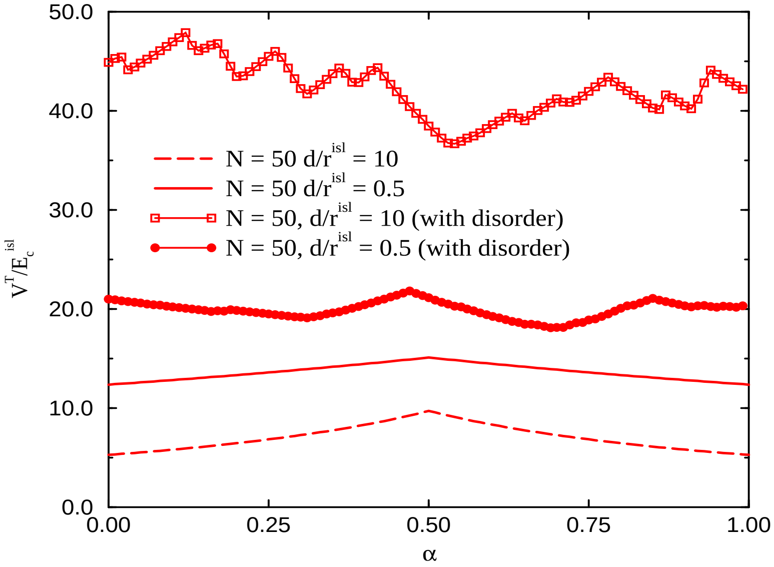

Figure 3.10: *Threshold, V_T, versus biasing asymmetry factor, α, for 50-island arrays at two different spacings, $d/r^{isl} = 0.5$ and 10, in the presence and absence of charged disorder.*

of the tunneling event that initiates the first sequences of hops that enable charge transfer to occur between the leads. Decreasing the spacing between the islands decreases the number of peaks and the sizes of the fluctuations in the threshold with respect to the biasing asymmetry factor, α. The thresholds of arrays with onsite interactions (Fig. 3.2) vary more regularly with α because the processes that set the threshold only occur at the contact junctions. In the long range case, the threshold process can occur at any junction on the array. In contrast to the onsite case, the thresholds of disordered arrays tend to be larger than the thresholds of clean arrays because more (as opposed to less) charges need to accumulate on disordered arrays compared to the clean arrays before current can flow.

3.3 Static Potentials of Disordered Arrays

This section provides a more detailed comparison of the ways that interactions affect the thresholds of arrays with charged disorder. As the applied voltage approaches the threshold, the energy costs of hopping across junctions, ΔE_i, tend to decrease because of voltage drops across junctions due to the potentials at the leads, $\Phi_i^{pol} < 0$, and due to charges that accumulate on the array, $\Phi_i^{ch} < 0$. This section shows how probability distributions of tunneling energies, $P(\Delta E_i)$, for arrays averaged over many configurations of disorder, respond to applied voltages as they approach the thresholds of the arrays. We compare how $P(\Delta E_i)$ evolves for arrays with onsite interactions and for arrays with long range interactions at two spacings, $d/r^{isl} = 10$ and 0.5. The smaller spacing is comparable to spacings realized in experiments and the larger spacing is included as a pedagogical example because it has interactions that are both long range and comparable to the onsite case. For each case, we compare arrays with different sets of junction resistances given by

$$R_i = [a + \delta_{i,k}(R - a)]R_0 \tag{3.14}$$

where $a = \frac{N+1-R}{N}$, N is the number of islands, and R_0 is a unit of resistance large enough for charging effects to be relevant. We compare arrays with resistances that are all equal, $R = 1$, with arrays that have one large resistance in the middle of the array, $R > 1$ in Eq. 3.14. The total series resistance of all these cases are the same and given by $\sum_{i=1}^{N+1} R_i = (N + 1)R_0$.

Fig. 3.11 shows how the probability distributions of the bulk tunneling energies, $P(\Delta E_i)$, of arrays with only onsite interactions change as the applied voltage approaches the threshold voltage The similarities of the graphs in Fig. 3.11 that correspond to different sets of resistances, R_i, illustrate how the evolution of $P(\Delta E_i)$ at these voltages is independent of R_i. These features are independent of the junction resistances because the zero temperature threshold is an electrostatic effect. At zero applied bias, all the bulk junctions are uncharged ($\delta Q_i = 0$) and $P(\Delta E_i)$ is the distribution for the potential differences due to disorder (Eq. 2.1.2) offset by the excitonic energy. As the voltage increases, charges enter the array and create charge gradients, Eq. 3.2.3, that decrease (do nothing to) the energies to tunnel across junctions with up-steps (down-steps). At the threshold voltage, the energy costs of hopping across the bulk junctions fall within a range,

$$0 \leq \Delta E \leq |\Phi^{add}| \, ,$$

where Φ^{add} is an extra potential drop that occurs across a junction when new injected charge(s) arrive at that junction. For arrays with onsite interactions, Φ^{add} equals $-2E_c^{isl}$ ($-4E_c^{isl}$) when one (two) injected charge(s) arrive at a junction. The latter case is rare for disordered arrays because the disorder potentials at the contact islands tend to break the symmetry between the costs of hopping across the contact junctions. This makes it unlikely for two charges of opposite sign to enter the array from opposing leads at the threshold voltage of disordered arrays. Because the applied voltage only modifies the potential drops across the up-steps, $P(\Delta E_i)$ is a flat distribution at $V = V_T$ with height $(E^{e-h})^{-1}$ lying between 0 and $2E_c^{isl}$. See Fig. 3.11 and Fig. 3.12.

Fig. 3.13 and Fig. 3.14 show how the energy costs of hopping across bulk junctions at two spacings, $d/r^{isl} = 10$ and 0.5, evolve as the applied voltage approaches the threshold for arrays with different sets of resistances. The similarities of the probability distributions, $P(\Delta E_i)$, of arrays with different resistances show that the zero temperature threshold is independent of the resistances because it is an electrostatic effect. At $V = 0$, the probability distribution of these energies, $P(\Delta E_i)$, equals the probability distribution of the disordered potential drops, $P(\Phi^{dis})$, offset by E_i^{e-h}. As the applied voltage increases, the distributions shift toward smaller

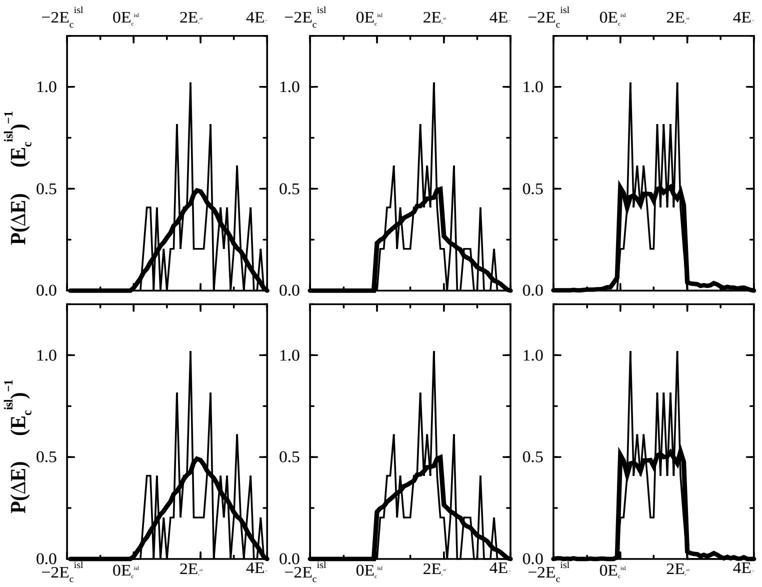

Figure 3.11: *Probability distributions of bulk junctions in the onsite limit for* $V < V_T$. The distributions denoted by solid (dashed) lines average over 1 (100) configuration(s) of disorder on 50-island arrays. From left to right, the graphs correspond to $V = (0, 0.5, 1)V_T$ where $V_T = 46.5E_c^{isl}$ is the threshold voltage of the array represented by the solid curves. The graphs in the top row correspond to arrays with junctions of equal resistance, $R_i = R_0$. The bottom row corresponds to arrays with the same total resistance as the top ($R^{tot} = 51R_0$) and all resistances equal except for one bulk junction with $R_k = 30R_0$.

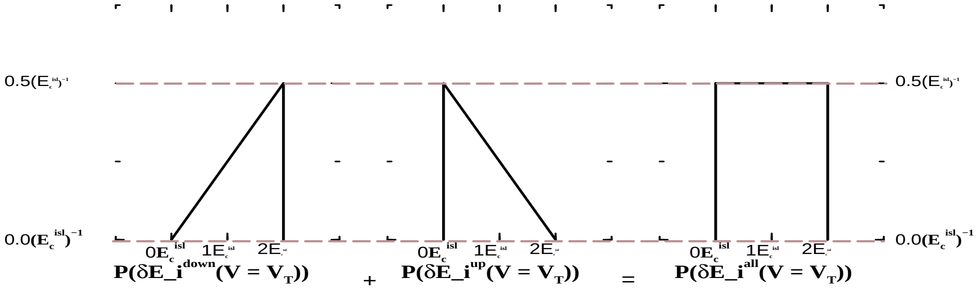

Figure 3.12: The sum of the distributions due to bulk junctions with down-steps ($\Phi^{dis} < 0$) and up-steps ($\Phi^{dis} > 0$) leads to the form of $P(\Delta E_i)$ at the threshold voltage in the limit of onsite interactions. At this voltage, the probability distributions due to up-steps and down-steps at $V = 0$ are shifted by $-2E_c^{isl}$ and 0.

values of ΔE_i. At the threshold voltage, the probability distributions are bound by 0 and $|\Phi_i^{add}|$. Unlike the onsite case, the high energy side of $P(\Delta E_i)$ does not drop abruptly at one value. This suggests that the additional energy that junctions gain due to the introduction of new charges at the threshold (E_i^{add}) varies from junction to junction. This is consistent with the long range model because the potential gradients across the junctions are sensitive to all the charges on the array. The actual values for $|\Phi_i^{add}|$ are larger than the estimate in Eq. 3.11 because multiple charges reduce the energies to hop across junctions at the threshold. Similar to the onsite case, $P(\Delta E_i)$ is larger within the region defined by $0 \leq \Delta E_i \leq E_i^{e-h}$ than it is within $E_i^{e-h} \leq \Delta E_i \leq 2E_i^{e-h}$. This means that a majority of the junctions allow tunneling to occur after one additional charge arrives at (or within the vicinity of) the junctions. Bulk junctions with ΔE_i between E_i^{e-h} and $2E_i^{e-h}$ at the threshold require more than one additional charge to move within the vicinity of the junction before charges can hop across them. In the extreme case that $\Delta E_i = 2E_i^{e-h}$, two charges of opposite sign must arrive at the islands on either side of the junction before tunneling can occur.

Long range interactions modify the charge gradients that accumulate across junctions at voltages leading up the threshold. In the onsite case, the charge gradients equaled $\delta Q_i = 0$ across down-steps and $\delta Q_i = 0$ or -1 across up-steps. At finite voltage, the polarization potential gradients across bulk junctions, $(\Phi_i^{pol})^{LR} < 0$, are always smaller than the onsite polarization drop across bulk junctions, $(\Phi_i^{pol})^{ONS} = 0$. As a result, the charge gradients across the bulk junctions, δQ_i^{LR}, are always greater than or equal to the charge gradients across junctions in the onsite case, δQ_i^{ONS}:

$$(\Phi_i^{pol})^{LR} < (\Phi_i^{pol})^{ONS} = 0 \Rightarrow \delta Q_i^{LR} \geq \delta Q_i^{ONS} \ . \tag{3.15}$$

For example, some junctions with up-steps ($\Phi^{dis} \geq 0$) will not require negative charge gradients at $V = V_T$ because the polarization voltage drops plus the negative

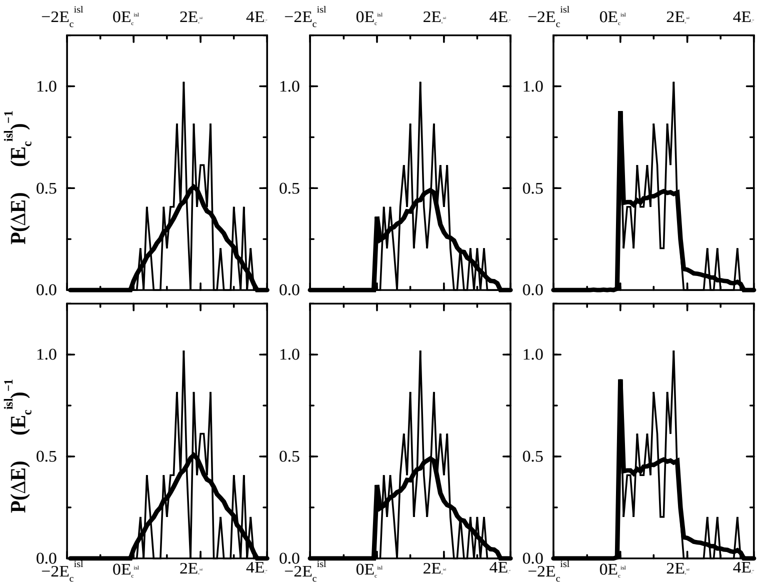

Figure 3.13: *Probability distributions of the bulk junctions for 50-islands arrays and spacing* $d/r^{isl} = 10$ *for* $V \leq V_T$. The distributions denoted by solid (dashed) lines average over 1 (100) configuration(s) of disorder. From left to right, the graphs correspond to $V = (0, 0.5, 1)V_T$ where $V_T \approx 36.55E_c^{isl}$ is the threshold voltage of the array represented by the solid curves. The arrays in the top row have equal resistances ($R = 1$ in Eq. 3.14). The arrays in the bottom row have one junction with a very large resistance ($R = 30$ in Eq. 3.14). All the arrays have the same total resistance $R^{tot} = 51R_0$.

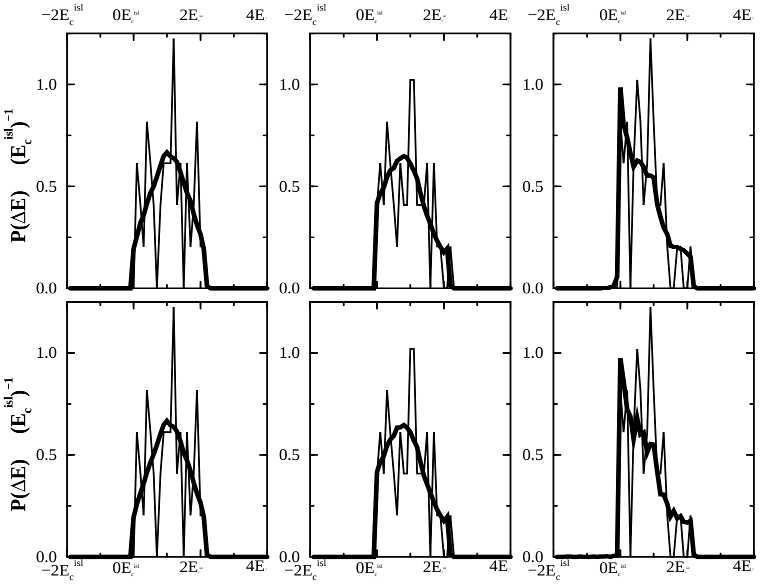

Figure 3.14: *Probability distributions of the bulk junctions for 50-islands arrays and spacing* $d/r^{isl} = 0.5$ *for* $V \leq V_T$. The distributions denoted by solid (dashed) lines average over 1 (100) configuration(s) of disorder. From left to right, the graphs correspond to $V = (0, 0.5, 1)V_T$ where $V_T \approx 16.69E_c^{isl}$ is the threshold voltage of the array represented by the solid curves. The graphs in the top (bottom) row have resistances described by $Eq.$ 3.14 and $R = 1$ ($R = 30$).

contributions in Φ_i^{ch} due to charges at other junctions are large enough to overcome the energy barriers at these junctions without these negative charge gradients. The charge gradients over some down-steps (junctions with $\Phi^{dis} < 0$) may be positive in order to compensate for the polarization voltage drops that make $\Delta E_i < 0$ at voltages smaller than the threshold.

Fig. 3.15 and Fig. 3.16 show how greater charge gradients across junctions contribute to the total voltage difference across junctions when interactions are long range. To make the effects of terms not included in the onsite model more clear, these figures include the distributions due to $\Phi_i^{ch,ONSITE}$, Φ_i^{ch}, and $\Phi_i^{ch} + \Phi_i^{pol}$. $\Phi_i^{ch,ONSITE}$ is the potential difference across junctions due only to onsite interactions ($\tilde{C}_{ij}^{-1} = \delta_{i,j}\tilde{C}_{i,i}^{-1}$). The different peaks in these distributions are caused by different charge gradients. Across up-steps, δQ_i can equal 0 and +1 in addition to the only value for up-steps in the onsite limit, $\delta Q_i = -1$. Across down-steps, δQ_i can equal 1 and 2 in addition to the onsite value for down-steps, $\delta Q_i = 0$. Φ_i^{ch} is the potential difference across junctions due to interactions among all charges on the array. Comparing $P(\Phi_i^{ch,ONSITE})$ and $P(\Phi_i^{ch})$ shows how long range interactions screen out the potentials due to onsite interactions. The degree to which long range interactions pull Φ_i^{ch} toward values close to 0 indicates how effectively charges screen each other's potentials. In the onsite case, $P(\Phi_i^{ch,ONSITE}) = P(\Phi_i^{ch})$ because charges can not screen the potentials of charges at other sites. Comparison of the smaller ($d/r^{isl} = 0.5$) and larger ($d/r^{isl} = 10$) spacings show that Coulomb interactions that occur in arrays at the smaller spacing are more effective at screening out the potential differences due to large charge gradients. The distributions of $\Phi_i^{ch} + \Phi_i^{pol}$ show how polarization potentials affect the potential differences. The addition of Φ_i^{pol} shifts the distributions to lower energies (except the onsite case) because Φ_i^{pol} is negative across all junctions that interact with the leads. Adding Φ_i^{pol} does not maintain the shape of the distributions because Φ_i^{pol} is *not* a constant across all

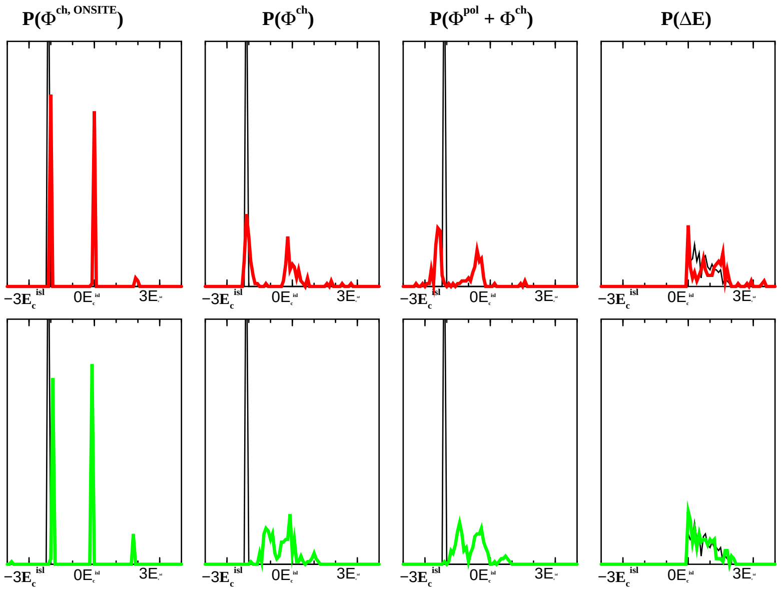

Figure 3.15: *Comparison of* $P(\Phi_i)$ *and* $P(\Delta E_i)$ *across junctions with up-steps* ($\Phi^{dis} \geq 0$) *at the threshold voltage.* The thin lines correspond to the distributions of 50-island arrays in the onsite limit. The thick lines in the top (bottom) row correspond to 50-island arrays with $d/r^{isl} = 10$ ($d/r^{isl} = 0.5$).

junctions. Its magnitude tends to decrease as the distance between the junction and the leads increases. Due to all of these effects, the tunneling energies of more bulk energies approach zero at smaller applied voltages as the range and strength of Coulomb interactions increase.

3.4 Finite Temperature Threshold

At finite temperature, the threshold voltage is less well defined because the current is finite valued at all applied voltages. At small enough temperatures, the current continues to be exponentially suppressed at voltages smaller than a threshold. We define the finite temperature threshold using the second derivative of the IV curves, $\partial^2 I/\partial V^2$. The threshold occurs at the first large peak in $\partial^2 I/\partial V^2$; at this voltage, the IV curve changes from an Arrhenius form to a different scaling relationship.

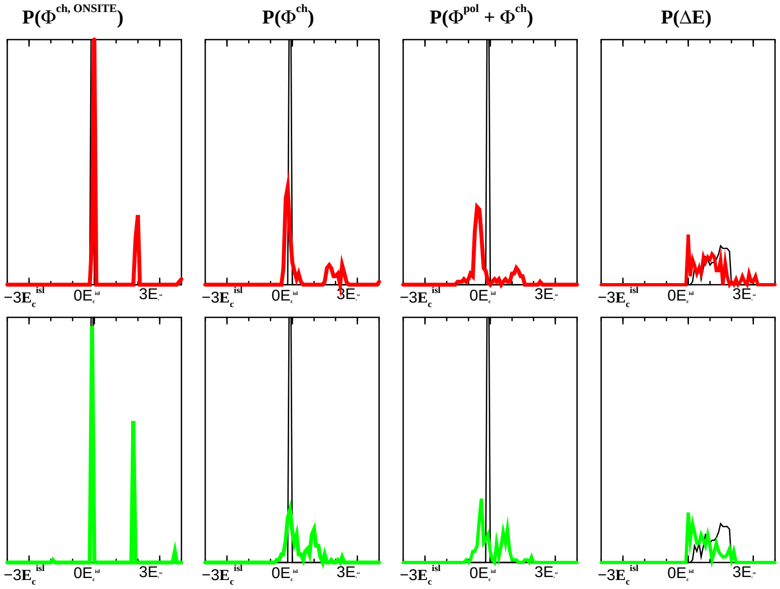

Figure 3.16: *Comparison of* $P(\Phi_i)$ *and* $P(\Delta E_i)$ *across junctions with down-steps* $(\Phi^{dis} < 0)$ *at the threshold voltage.* The thin lines correspond to the distributions of 50-island arrays in the onsite limit. The thick lines in the top (bottom) row correspond to 50-island arrays with $d/r^{isl} = 10$ $(d/r^{isl} = 0.5)$.

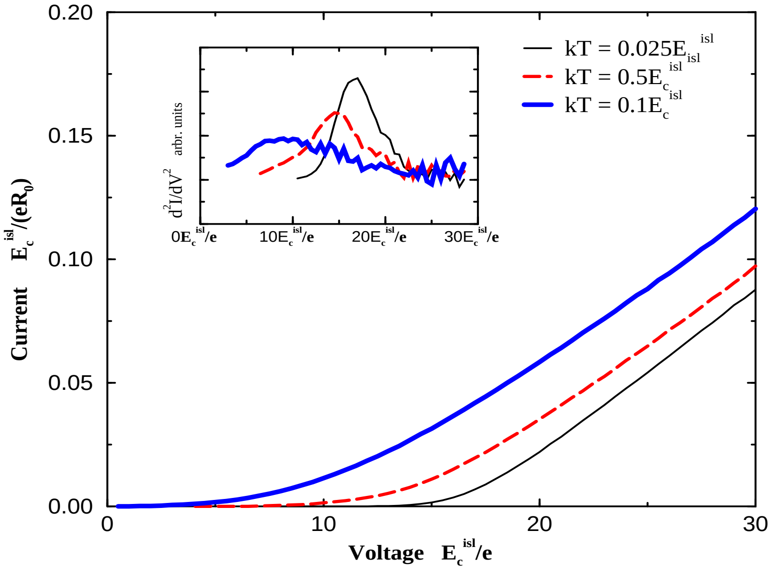

Figure 3.17: *IV curves and thresholds of a 50-island array with disorder at finite temperatures.* The finite temperature threshold occurs at the peak in the second derivative of each IV curves shown in the inset.

See Fig. 3.17. We found for arrays with long range interactions and with disorder that the threshold decreases with increasing temperature. At small temperatures, $kT < 0.1E_c^{isl}$, our thresholds agree with the prediction, Eq. 3.1.2, made by Elteto, et al. [17]. At $T \geq 0.1E_c^{isl}$, the threshold is hard to define using the peak in $\partial^2 I/\partial V^2$. This peak broadens with increasing temperature because the temperatures washes out the transition between the regions above and below the threshold. See Fig. 3.17 and Fig. 3.18. Finite temperature decreases the threshold by relaxing the condition for tunneling events across junctions. When a charge hops across a previously uncharged bulk junction, an electron and a hole forms at the sites on either side of the junction. If this occurs over multiple junctions and the electrons and holes drift apart, they can meet across junctions and eliminate some of potential barriers due to large charging costs and due to disorder.

In the limit of onsite interactions, finite temperatures dramatically change

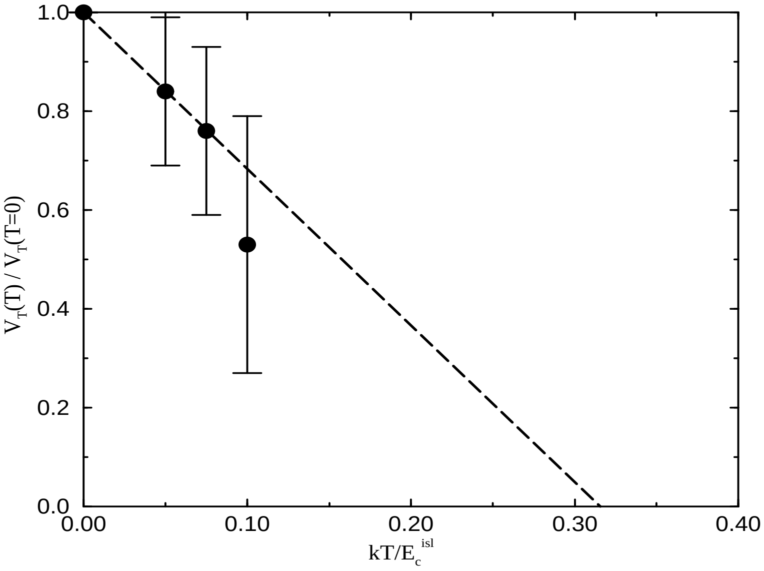

Figure 3.18: *Average finite temperature thresholds versus temperature for 50-island arrays with disorder and spacing,* $d/r^{isl} = 0.5$*.* The closed circles are the average thresholds of 15 arrays. The error bars have lengths equal to the rms fluctuations of the thresholds. Each threshold was determined by locating the peak in $\partial^2 I/\partial V^2$. See Fig. 3.17. The dotted line is the prediction made by Elteto, et al. [17]: $Vt(T)/Vt(T=0) = 1 - 4.8P(0)kT$ where $P(0) = 0.66(E_c^{isl})^{-1}$ for 50-island arrays with $d/r^{isl} = 0.5$.

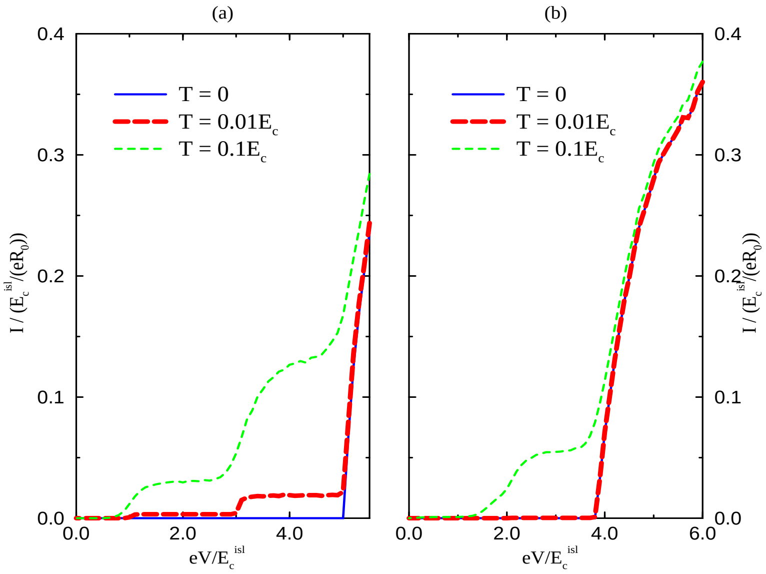

Figure 3.19: *IV curves for a 5-island array without (a) and with (b) charged disorder at several temperatures.*

the IV curves because finite temperature allow hops to occur across bulk junctions that were forbidden at zero temperature. See Fig. 3.19. Steps appear in the IV curves below the zero temperature threshold voltage. The rises in the steps occur at voltages that increase the average charge at the contact islands. These are spaced $2E_c^{isl} = eC_0^{-1}$ apart. The flat regions of the steps occur because the time for a net charge to hop across the array is dominated by multiple hops across the bulk junctions. The rate of hopping across bulk junctions does not directly depend on the applied voltage V because $\Phi_i^{pol} = 0$ across the bulk junctions. In this case, peaks in $\partial^2 I/\partial V^2$ can not be used to define a threshold that decreases slowly with increasing temperature.

3.5 Conclusions

We have determined the threshold dependence on array length in number of nanoparticles, N, and on the biasing asymmetry, α, for arrays with long range interactions and onsite interactions in the presence and absence of disorder.

We have found that the average threshold of disordered arrays (averaged over many configurations of disorder) scales linearly with array length, N, for arrays with onsite interactions and with long range interactions. Our average threshold results for the onsite case agree with Middleton and Wingreen's (MW) results. We used an analogy to the onsite threshold to derive an upper limit for the threshold in the long range case:

$$\langle V_T \rangle = \langle E_i^{e-h} \rangle \langle N_{up} \rangle = \langle E_i^{e-h} \rangle (N/2)$$

where E_i^{e-h} is given by Eq. 2.2.1. Eq. 3.5 reduces to the MW's equation, Eq. 3.1.1, when interactions are extremely short range [35]. When interactions are long range, this expression describes how the slope, $\partial \langle Vt \rangle / \partial N$, decreases as interaction strength increases due to decreasing the spacing between nanoparticles. This upper limit more closely approaches the thresholds we determined numerically than a long screening length estimate for the threshold proposed by MW and another estimate proposed by Elteto, et al. that includes interactions among charges on nearest neighboring nanoparticles [35, 17]. See Table 3.2. Eq. 3.5 overestimates the threshold because it is based on a conservative assumption for how newly injected charges modify the potential gradients across array junctions, i.e. only one newly injected charge resting on an island on one side of a junction modifies the potential gradient across any given junction. In reality, long range interactions allow multiple charges at multiple locations on the array to modify the potential gradients across junctions.

Our numerical results for $\langle V_T(N) \rangle$ at spacings that are comparable to spacings in real experiments ($d/r^{isl} = 0.5$) are in reasonable agreement with experimental measurements of the threshold on 1-D arrays. Our numerical results overestimate the thresholds of quasi-1-D arrays. It is possible for the thresholds of quasi-1-D arrays to be smaller than the thresholds of 1-D arrays because charges can access pathways in these arrays that are absent in the 1-D case that enable them to avoid some barriers to current flow. See Fig. 3.9.

In the absence of disorder, we found that the threshold has a step-like dependence on array length (Fig. 3.3) in the limit of onsite interactions due to two ways to initiate current through arrays with onsite interactions. In one way, current is initiated by the injection of a single charge across one of the contact junctions. The other way requires two charges of opposite sign to be injected through the two opposing contact junctions. These two ways for initiating current cause the thresholds of individual arrays with onsite interactions to fluctuate continuously between two limiting values that are separated by $\Delta V_T = 2E_c^{isl}$ in response to changing a biasing asymmetry factor, α, which describes how the applied voltage, V, is distributed between the source lead, $V_0 = \alpha V$, and the drain lead $V_{N+1} = (1-\alpha)V$. See Fig. 3.2. At zero temperature and in the limit of onsite interactions, the thresholds of arrays without disorder are greater than the thresholds of arrays with disorder because charge gradients must build up across all bulk junctions (junctions between neighboring islands) in the clean case instead of just the bulk junctions with up-steps (junctions with $\Phi^{dis} > 0$) in the disordered case.

Arrays without disorder and with long range interactions have the smallest thresholds because this threshold corresponds to the minimum threshold to allow a charge to hop across a junction when the array is empty of excess charges. For all the spacings we studied, this threshold always occurred across a contact junction because the polarization potential gradient, Φ_i^{pol}, is greatest across the junctions at the edges of the array. As long as interactions among the leads are not too strong, the thresholds in this case increased as the array length increased and as the spacing between islands decreased because these changes cause less of the applied voltage, V, to fall across the contact junctions (Fig. 3.4). In the limit of very large arrays, the threshold saturates to a value that increases as the spacing between nanoparticles decreases. This is in qualitative agreement with the soliton threshold proposed by Likharev, et al. (Eq. 3.1.1); however our results do not quantitatively agree because we do not use the soliton model to derive our inverse capacitance matrices. See Table 3.1.

Increasing the biasing asymmetry factor (increasing $|\alpha - 1/2|$), caused the thresholds of arrays with long range interactions in the absence of disorder to decrease smoothly because these changes cause more of the applied potential to drop across the contact junction that sets the threshold. When the arrays include disorder, varying α causes the thresholds to fluctuate with less regularity than disordered arrays in the onsite case because the long range case allows any junction (instead of just the contact junctions) to house the first tunneling event that initiates the first sequence of hops that transfer charge between the leads. Increasing the range of interactions (by decreasing the spacing between nanoparticles) decreases the dependence of the threshold on the biasing asymmetry factor α.

Finally we examined how temperature affects the thresholds of disordered arrays. As long as the temperature is not too large, $kT < 0.1E_c^{isl}$, we can define a threshold using a peak in the second derivative of the IV curves. In the temperature range where we are able to define a threshold, our results are in good agreement with Elteto, et al.'s model for the finite temperature threshold [17]. See Fig. 3.18.

Arrays with onsite interactions can not be described by this model because of the way temperature affects the local thresholds of these arrays. At zero temperature, charge gradients, $\delta Q_i = -1$, must build across any bulk junctions with up-steps ($\Phi^{dis} \geq 0$) in order to create potential gradients that facilitate current flow that the applied potentials can not directly supply because these potentials drop completely across the contact junctions. Finite temperatures allow charges to hop across the bulk junctions in the absence of these charge gradients. As a result, steps appear in the IV curves at voltages below the zero temperature threshold. See Fig. 3.19. The steps occur at voltages that allow the time-averaged charge at the contacts to increase by one. The flat regions in between the steps are due to current flow that is dominated by the times spent hopping across the bulk junctions; these time are independent of the applied voltage because the applied voltage does not directly drop across the bulk junctions in the onsite limit.

Chapter 4

Low Temperature Transport Characteristics

Charging effects complicate the transport characteristics of nanoparticle arrays. When a small bias is applied to the arrays, the response of the system is determined by the capacitances of the system. At very large applied biases, the resistances of the array junctions determine the transport characteristics. We have found two distinct scaling relationships

$$I \propto (V - V_T)^{\eta} \ ,$$

that correspond to these two regimes. Both regimes have linear scaling, $\eta = 1$. The slope of the resistance regime is related to the total series resistance of the array, $\partial I/\partial V = R_{tot}^{-1}$. The slope of the low voltage regime depends on the resistance and the electrostatic potential drop across one or two junctions that act as bottlenecks at voltages close to threshold. We investigated how these scaling relationships arise from the local responses of the arrays to the applied voltage by calculating how the probability distributions of the hopping energies of array junctions, $P(\Delta E_i)$, and the currents of arrays vary with applied voltage.

Sec. 4.2 and Sec. 4.3 discuss our results for the capacitance and resistance dominated regimes. Sec. 4.4 describes how arrays transition between these two regimes. Sec. 4.1 reviews scaling predictions and scaling measurements from previous works and experiments.

4.1 Background

A variety of scaling forms have been predicted and measured for the IV curves of 1-D nanoparticle arrays. This section reviews these results.

For 1-D arrays, Middleton and Wingreen (1993) predicted that the IV curves would have linear scaling at voltages very close to the threshold and at very large voltages [35]. In both regimes, they predicted that the slope would be given by [1]

$$\frac{\partial I}{\partial V} = \frac{1}{R_0(N+1)} \approx \frac{1}{NR_0} \,.$$

Close to the current, they explained the form of Eq. 4.1 by arguing that the average voltage drop across the junction that determines the current near threshold (the bottleneck) is approximately given $(V - V_T)/N$ [35, 24].

Jha and Middleton (2005) revisited this model in more detail. They determined the scaling exponents of arrays with uniform capacitances (UC) and the new case of disordered capacitances (DC). They analytically argued that the scaling should be linear at the high and low voltage regimes for both UC and DC arrays. Numerically they found for the UC arrays, that the scaling near threshold was linear as long as the arrays were very long, $N > 500$ [24]. For the DC arrays, they numerically found exponents other than $\eta = 1$ at the high and low voltages even in the limit of very long arrays. See Table 4.1. At low voltages, their scaling exponents were depressed by plateau regions in the IV curves.

---

[1] Middleton and Wingreen express the current in terms of the of the reduced voltage, $v = (V - V_T)/V_T$, i.e. $I = (e/(2RC_0)v$ [35]. The derivative of this current with respect to the voltage V along with $V_T = eL/(2C)$ leads to the equivalent expression, Eq. 4.1 The slope is expressed in the form for easier comparison with results that follow in this chapter.

Reichhardt and Reichhardt (2003) measured the scaling exponent of arrays using a model with a $1/r$ interaction between the charges in the islands and a linear drop for the polarization potential [40] . Numerically, they found a deviation from linearity at voltages close to the threshold. At larger voltages, $v > 1$, they found that the IV scales linearly for 1-D arrays. Analytically, they argued that near the threshold, the scaling exponent should be the same as a sliding charge-density wave, $\eta = 1/2$ [20].

Kaplan, Sverdlov, & Likharev (2003) et al. [26] numerically analyzed arrays with charged disorder and with very long soliton lengths and found that the IV scales linearly at voltages near the threshold.

Table 4.1 lists some of the scaling exponents that have been measured in experiments with 1-D and quasi-1-D arrays. This list is typical of the variety of scaling exponents that have been measured on nanoparticle arrays. Measurements of the scaling relationship at voltages close to the threshold rarely found scaling exponents equal to one. Typically this exponent was greater than one. We found that the scaling exponent equals one in regions of voltage that are very close to the threshold. These regions are closer to the thresholds than the regions tabulated here. See Table 4.2.

4.2 Bottleneck Regime

In this section, we show that the current varies linearly with respect to $V - V_T$ for very small $V - V_T$ and that the slope is not inversely proportional to N. The slope is sensitive to the range of Coulomb interactions and to the degree of symmetry between the applied bias voltages on the source and drain leads. This linear dependence extends over several orders of magnitude. However, the linear regime vanishes at voltages small enough that this regime is probably not relevant experimentally.

Reference	Dimension	η	Reduced voltage range
Rimberg, Ho, & Clarke (1995) [42]	1-D	1.36 ± 1	$0.1 < v < 8$
		1	$v > 8$
Bezryadin, Westervelt, & Tinkham (1998) [4]	quasi-1-D	1.03, 2.06, 2.32	$10^{-2} < v < 10^{0}$
Elteto, Lin, & Jaeger (2005) [18]	quasi-1-D	1.5 - 1.8	$0.1 < v < 10$
Jha & Middleton (2005) [24]	1-D (DC, $N \geq 500$)	0.85 ± 0.02	$0.05 < v < 5$
		1.2 ± 0.05	$v > 1$
	1-D (UC, $N > 500$)	≈ 1	$0.05 < v < 5$
	1-D (UC, $N < 500$)	≈ 0.85	$0.05 < v < 5$
		≈ 1.05	$v > 1$

Table 4.1: *Scaling exponents measured on 1-D and quasi-1-D arrays.* The reduced voltage is related to the applied voltage, V, and the threshold voltage, V_T, by $v = (V - V_T)/V_T$. Rimberg, et al.'s arrays consist of Al islands linked by Al/Al$_xO_y/Al$ junction produced by e-beam lithography [42]. Bezryadin, et al.'s arrays consist of 1-D chains of carbon nanoparticles that are occasionally broken up by 2-D clusters of nanoparticles [4]. See Fig. 1.2(b). Elteto, et al.'s arrays are composed of gold nanoparticles that are approximately 60 nanoparticles long and 4 nanoparticles wide [18]. Jha & Middleton (2005) obtained their results numerically. DC (UC) correspond to arrays with random capacitance (uniform capacitances).

		Clean Arrays		Disordered Arrays	
N	Range	$\tilde{V}_{max}$	v_{max}	$\tilde{V}_{max}$	v_{max}
5	$d/r^{isl} = 0.5$	0.002	8×10^{-4}	0.005	2×10^{-4}
5	onsite	0.004	4×10^{-4}	0.01	2×10^{-3}
50	$d/r^{isl} = 0.5$	0.002	1×10^{-4}	0.01	2×10^{-4}
50	$d/r^{isl} = 10$	0.003	3×10^{-5}		
50	onsite	0.03	3×10^{-4}	0.01	2×10^{-4}

Table 4.2: *Approximate sizes of voltage ranges near threshold with linear scaling.* Linear scaling appears for $\tilde{V} = V - V_T < \tilde{V}_{max}$ (in units of E_c^{isl}) or for $v = \tilde{V}/V_T < v_{max}$ (in units of reduced voltage). Linear scaling disappears at voltages smaller than the voltage ranges used to measure the scaling exponents in Table 4.1.

At the threshold voltage, current first begins to flow across arrays at zero temperature. At finite temperature, current can be nonzero at smaller applied biases. When the applied bias reaches the threshold voltage, the energy cost of hopping across one junction, the *bottleneck*, becomes slightly less than 0, $\Delta E_{bn} < 0$. Following a hop across this junction, the injected charge changes Φ_i^{ch} across the other array junctions in such a way that $\Delta E_i < \Delta E_{bn}$ and as a result the injected charge moves quickly across the array. The total time of this sequence of hops is so small compared to the average time associated with the hop across the bottleneck junction that the arrays islands and junctions surrounding the bottleneck junction effectively behave like extensions of the leads that voltage bias the bottleneck junction. When the time to transport a net charge between the leads nearly equals the time to tunnel across the bottleneck, the array current nearly equals the current across the bottleneck junction:

$$I = e\Gamma_{bn} = |\Delta E_{bn}|/(eR_{bn}) \ . \tag{4.1}$$

The I(V) curve in this regime is linear and has a slope that depends on the portion of the potential difference across the bottleneck junction that is directly related to the applied bias voltage, Φ_{bn}^{pol}:

$$\begin{aligned} \frac{\partial I}{\partial V} &= \frac{1}{eR_{bn}} \frac{\partial}{\partial V} |\Delta E_{bn}| \\ &= \frac{1}{eR_{bn}} \frac{\partial}{\partial V} |\Phi_{bn}^{pol}| \\ &= \frac{1}{eR_{bn}} |\Lambda_{bn}| \ . \end{aligned} \tag{4.2}$$

$\Lambda_i = \Phi_i^{pol}/V$ is a negative number between 0 and 1 whose absolute value equals the fraction of the total polarization drop that is distributed over the i-th junction. See Eq. 3.8. The slope of the IV curve in the bottleneck regime, Eq. 4.2, does not equal R_{tot}^{-1} unless the polarization potential drops linearly across the array. In this case, Φ_i^{pol} is constant and $\Lambda_i = -(N+1)^{-1}$ across all the junctions. In general, this is not

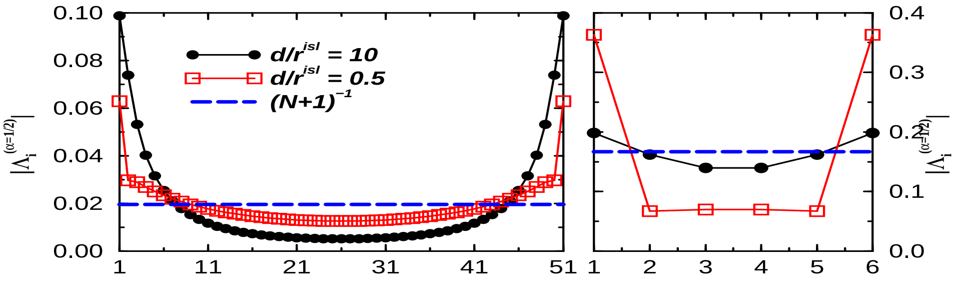

Figure 4.1: Fraction of polarization potential that drops across array junctions, $|\Lambda_i|$, for 50-island and a 5-island arrays that are symmetrically biased.
Λ_i were determined by using Eq. 3.8 with $\alpha = 1/2$.

true because $|\Lambda_i|$ depends on the positions of the junctions and tends to be largest for junctions closest to the leads. Fig. 4.1 shows how $|\Lambda_i|$ compares to $(N+1)^{-1}$ for arrays of length, $N = 5$ and $N = 50$, and spacing, $d/r^{isl} = 0.5$ and 10.

In the bottleneck regime, the position of the bottleneck and the voltage drop across the bottleneck junction is unrelated to the resistances of the array junctions because the charge configuration on the array, Q_i, is nearly static. The array spends most of its time in the bottleneck configuration of charges and the electrostatic potentials due to these charges determine the position and the voltage drop across the bottleneck. The position of the bottleneck is the junction with the minimum ΔE_i when the array is in the bottleneck configuration. The position of the bottleneck is unrelated to the positions of the junctions with the smallest or largest resistance. Earlier we saw evidence of the lack of effect of the resistances on the probability distributions, $P(\Delta E_i)$, leading up to threshold. Fig. 3.11, Fig. 3.13, and Fig. 3.14 all show that the evolution of the hopping energies across junctions leading up to the threshold is independent of the resistances across junctions. The independence of the current on R_i at voltages close to the threshold is also shown in the insets of Fig. 4.9, Fig. 4.10, and Fig. 4.11.

Numerically, we were able to observe the linear scaling of the IV curves down to voltages that are very close to threshold, $\tilde{V} = V - V_T \ll 1$. Starting from voltages very close to the threshold, $\tilde{V} = V - V_T > 10^{-16}$, we observe linear scaling over many orders of magnitude in $\tilde{V}$. The linear scaling disappears when the bottleneck approximation, Eq. 4.1, ceases to provide a good description of the array current. We found that the linear behavior gave way to sublinear behavior at voltages not much larger than the threshold. The sublinear behavior does not constitute a new scaling regime because it does not persist over a large enough voltage interval.

The bottleneck approximation loses validity when tunneling processes, other than the hop across the bottleneck, develop rates with increasing voltage that are comparable to the bottleneck rate when the array is in the bottleneck state. The bottleneck approximation also breaks down when two or more hops among a sequence of hops that transfer a net charge between the leads significantly contribute to the total average time of this sequence. For example, consider the average times associated with two hops among a sequence that transfers charge between the leads. The average time associated with one hop (a hop across the bottleneck) equals $\langle\tau\rangle^{-1} = \Gamma_i = R_i^{-1}\Lambda_i\tilde{V}$ with $\tilde{V} = V - V_T$ and the average time associated with the other hop equals $\langle\tau\rangle^{-1} = \Gamma_j = R_j^{-1}(|\Phi_j^{add}| + \Lambda_j\tilde{V})$ where $|\Phi_j^{add}|$ is a gain in energy that the second junction acquires at the threshold voltage. If these two processes have rates much smaller than the rest of processes in the sequence, the current can be approximated by

$$\begin{aligned} I \sim \frac{1}{\tau_i + \tau_j} &= \frac{R_i^{-1}\Lambda_i\tilde{V}}{1 + \frac{R_i^{-1}\Lambda_i\tilde{V}}{R_j^{-1}\left(|\Phi_j^{add}|+\Lambda_j\tilde{V}\right)}} \\ &\sim R_i^{-1}\gamma_i\tilde{V}\left(1 - \frac{R_i^{-1}\Lambda_i\tilde{V}}{R_j^{-1}\left(|\Phi_j^{add}| + \Lambda_j\tilde{V}\right)}\right) . \end{aligned} \tag{4.3}$$

Eq. 4.3 qualitatively suggests the linear regime will persist over wider voltage ranges for arrays where $|\Lambda_i|$ tend to be more homogeneous. This tends to occur as N and

d/r^{isl} decrease.

Sec. 4.2.1 and Sec. 4.2.2 discuss how the slopes of the IV curves depend on disorder and the biasing asymmetry factor, α, for arrays with long range interactions and arrays with onsite interactions.

4.2.1 Bottleneck regime for arrays with long range interactions

In the absence of disorder, the same junction(s) that set the threshold voltage discussed in Sec. 3.2.2, $V_T = \min(V_i^{th})$, are the bottleneck junction(s). These bottlenecks occur at one or both of the contact junctions because the voltage drops across these junctions tend to be the largest when the array is empty of any excess charge. The behavior of the slopes of I versus $\tilde{V} = V - V_T$ with respect to α, N, and d/r^{isl} are the opposites of the behaviors of the thresholds with respect to the same parameters because $V_T \propto |\Lambda_{bn}|^{-1}$. Increasing N and decreasing d/r^{isl} decreases the slope because these changes reduce the fraction of the polarization potential that drops across the contact junctions. See Fig. 4.2(a).

With the exception of symmetrically biased arrays, biasing the array in a more asymmetric way (increasing $|\alpha - 1/2|$) always increases the slope because this change increases the fraction of the polarization potential that drops across the contact junction that acts as a bottleneck at small voltages. When the ordered array is symmetrically biased ($\alpha = 1/2$), the slope is proportional to $2\Lambda_{bn}^{\alpha=1/2}$ instead of $\Lambda_{bn}^{\alpha=1/2}$ due to the symmetry between the energy costs of hopping across the two contact junctions. Because of this symmetry, the average bottleneck current is given by $I \propto \langle\tau\rangle^{-1} = \sum_i \Gamma_i = (2)|\Delta E_{bn}|$ where the factor of (2) comes from the two contact junctions that each have $\Delta E_1 = \Delta E_{N+1} = \Delta E_{bn}$.

When the array has charged disorder, the bottleneck can occur at junctions other than the contact junctions. Fig. 4.3(a) shows three symmetrically biased arrays with the same length and spacing that each have a different configuration

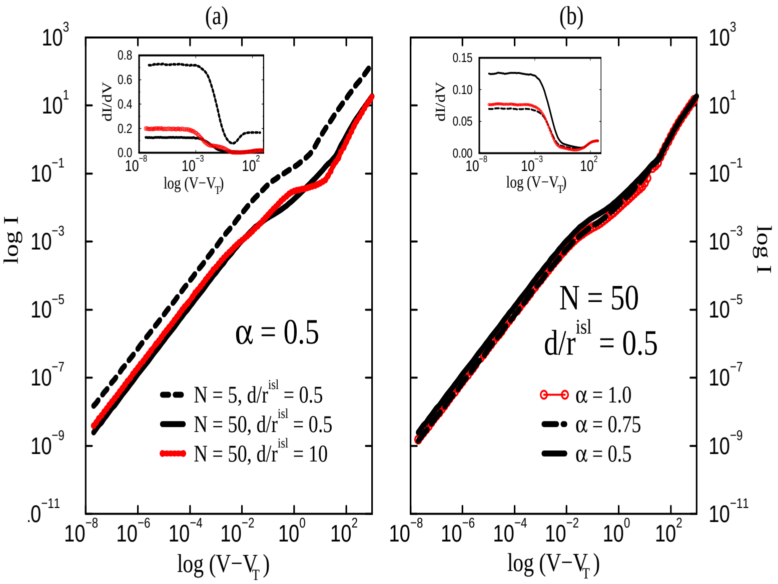

Figure 4.2: *IV and $\partial I/\partial V$ curves of ordered arrays with long range Coulomb interactions.* In Fig. 4.2(a), decreasing N and increasing d/r^{isl} decreases the slope of the IV curves in the region close to the threshold. In Fig. 4.2(b), increasing the biasing asymmetry (increasing $|\alpha - 1/2|$) increases the slope in the low voltage regime with the exception of the perfectly symmetric case which has the largest slope because the symmetry between two bottlenecks doubles the current and its slope in this case.

of disorder, $\{\Phi_i^{dis}\}$. The different values of the slope for these three cases illustrate how different configurations of disorder can position the bottlenecks across different junctions in arrays.

Changing the biasing asymmetry factor, α, changes the slope of the IV curves of disordered arrays. The slope changes because Λ_{bn}^{α} varies with respect to α. In addition, the slope can change if the bottleneck switches to a different junction. Unlike arrays without disorder, the slope of the bottleneck current does not always increase as the voltage becomes more asymmetric (increasing $|\alpha - 1/2|$) because the position of the bottleneck is not fixed. Fig. 4.3(b) gives an example of a disordered array whose slope does not respond to variations in α in a consistent way due to changes in the position of the bottleneck.

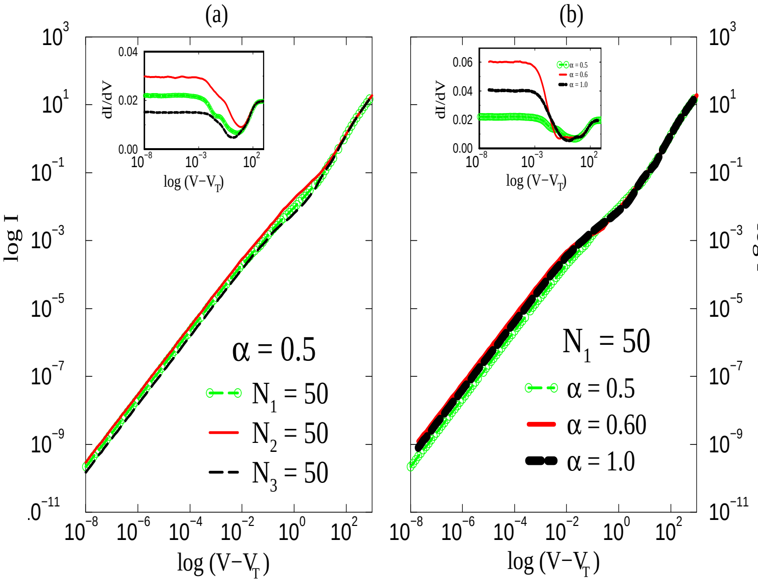

Figure 4.3: *IV and $\partial I/\partial V$ curves of disordered arrays with long range Coulomb interactions.* Fig. 4.3(a) shows how varying the charged disorder configuration, $\{\Phi_i^{dis}\}$ changes the slopes and IV curves of 50-island arrays with spacing, $d/r^{isl} = 0.5$. Near the threshold voltage, changing $\{\Phi_i^{dis}\}$ changes the slope by changing the position of the bottleneck. Fig. 4.3(b) shows how varying only the biasing asymmetry (α) affects a disordered array. Increasing the biasing asymmetry does not always increase the slope of the low voltage regime because changing α can change the position of the bottleneck.

4.2.2 Bottleneck regime for arrays with onsite interactions

For arrays with onsite interactions, the finite-valued slopes of the IV curves at voltages close to thresholds with and without disorder are determined by the voltage drops across either or both of the contact junctions. Regions of the IV curves with zero slope can occur when the average time to transfer a net charge between the leads is dominated by processes that occur at bulk junctions. These flat IV regions are too small to define a scaling regime because they are interrupted regularly by sharp rises in the current that occur at voltages that allow the average amount of charge residing at the contact islands to increase.

In the absence of disorder, we found that the slopes of the IV curves of symmetrically biased arrays depend on whether the arrays have even or odd numbers of islands. When $R_0 = e = 1$, the slopes are given by

$$\frac{\partial I}{\partial V} = \begin{cases} (2)|\Lambda_1^{\alpha=1/2}| = 1 & \text{when } N \text{ is odd} \\ (1)|\Lambda_1^{\alpha=1/2}| = 1/2 & \text{when } N \text{ is even} \end{cases} .$$

This dependence is shown for a few arrays in Fig. 4.4(a). Due to the symmetry between the contact junctions, the average time spent hopping across one of the contact junctions is given by $\tau_{bn} = (\sum_i \Gamma_i)^{-1} = (2|\Delta E_1|)^{-1}$. When N is odd, only one hop across a bottleneck must occur in a sequence of hops that transfer one net charge between the leads. In this case, the bottleneck current approximately equals $I \propto (\tau_{bn})^{-1} = 2|\Delta E_1|$ which leads to the slope above. When N is even, two hops must occur across bottlenecks in each sequence of hops that transfer one charge between the leads because two injected charges must meet in the middle of array in order to overcome all the barriers to current flow. In this case, the bottleneck current is given by $I \propto (2\tau_{bn})^{-1} = |\Delta E_1|$ which leads to the smaller slope for arrays with even N.

When the arrays are disordered and symmetrically biased, potentials due to disorder at the edges of the arrays remove the symmetry between the energies to inject charges at both contact junctions. In this case, the bottleneck occurs at either one junction and the average bottleneck time is given by $\tau_{bn} = (\sum_i \Gamma_i)^{-1} = (|\Delta E_{bn}|)^{-1}$ when $e = R_{bn} = 1$. ΔE_{bn} equals ΔE_1 (ΔE_{N+1}) when the bottleneck occurs at the source (drain) contact junction. Each sequence of hops that transfer charge between the leads has only one hop across a bottleneck so the current approximately equals $I \propto (\tau_{bn})^{-1} = |\Delta E_{bn}|$ which always has the slope, $|\Lambda_1| = |\Lambda_{N+1}| = 1/2$, when the array is symmetrically biased. Fig. 4.5(b) shows how the slope of symmetrically biased disordered arrays is unaffected by N and by different disorder configurations, $\{\Phi_i^{dis}\}$.

Increasing the asymmetry between the potentials at the source and drain leads (increasing $|\alpha - 1/2|$) does not always increase the slope because as α is the varied, the bottleneck currents are alternately determined by the contact junction closest to the source and to the drain. The slopes equal $\Lambda_1 = \alpha$ and $\Lambda_{N+1} = 1 - \alpha$ when the bottleneck occurs at the contact closest to the source and drain respectively. The factors of 2 that appeared in the slopes of symmetrically biased arrays without disorder do not affect the slopes when $\alpha \neq 1/2$ because differences between Λ_1 and Λ_{N+1} remove the symmetry between the energy costs of injecting charges through either contact junction. Fig. 4.4(b) and Fig. 4.5(b) show how the slopes near threshold vary for ordered and disordered arrays in response to changing α. Both figures show how the slope changes gradually over ranges of α that correspond to only one contact junction and change abruptly between values of α that switch the position of the bottleneck from one contact junction to the other contact junction.

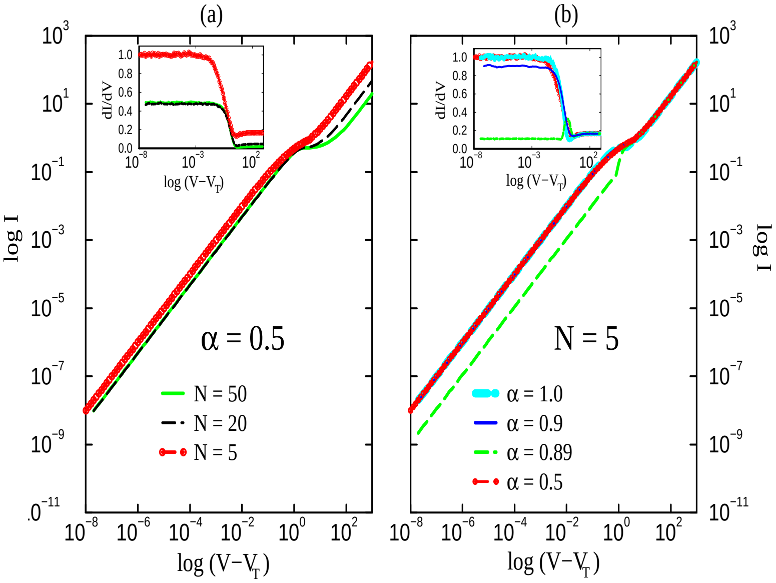

Figure 4.4: *IV and $\partial I/\partial V$ curves for arrays without disorder in the limit of onsite interactions.* In Fig. 4.4(a), the slope of the IV curves of symmetrically biased arrays near their thresholds equals $|\Lambda_1| = 1/2$ when N is even and $2|\Lambda_1| = 1$ when N is odd. The slope is halved when N is even because charges need to cross two bottlenecks (instead of one) before a net charge can be transferred between the leads at these small voltages. Fig. 4.4(b) shows how the slope near the threshold varies both smoothly and abruptly as the biasing asymmetry factor α is varied. The slope varies smoothly with α when modifying α only changes the potential drop across a bottleneck whose position is fixed at either one of the contact junctions. The slope varies abruptly when changing α changes the position of the bottleneck from one contact junction to the other contact junction.

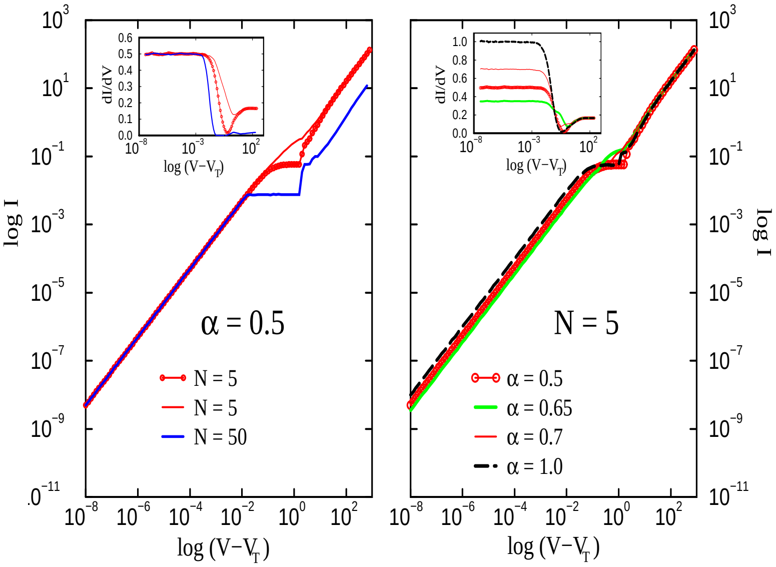

Figure 4.5: *IV and $\partial I/\partial V$ curves of disordered arrays in the onsite limit.* Fig. 4.5(a) shows the IV and $\partial I/\partial V$ curves of several symmetrically biased arrays:two 5-island arrays with different disorder configurations and a 50-island array. Comparing their slopes near the thresholds shows the independence of the slope on N and $\{\Phi_i^{dis}\}$ when arrays are disordered and symmetrically biased. Fig. 4.5(b) shows how varying the biasing asymmetry (α) alone affects a disordered array. Just as in arrays without disorder, Fig. 4.4(b), the slopes vary smoothly and abruptly with α because varying α can modify the potential drops across the bottleneck(s) and also change the position of the bottleneck from one contact junction to the other contact junction.

4.3 Linear Resistance regime

At large enough voltages, we found that the IV curves of 1-D nanoparticle arrays are linear and the slope of the curves is determined by the total series resistance of the array junctions, $\partial I/\partial V = (R_{tot})^{-1}$. In this limit, the energy to hop across each array junction, ΔE_i, is proportional to the resistance across each junction, R_i. We observed how interaction strengths and the resistances affect the transition to the linear resistance regime by plotting how the currents, $I(V)$, and the distributions of tunneling energies, $P(\Delta E_i(V))$, evolve with increasing voltage for arrays with different interaction strengths and with two different types of resistance configurations. We compared the characteristics of arrays with resistances that are all equal to arrays with resistances that are all equal except for one large resistance in the middle of the array. Both cases have the same total resistance, $R_{tot} = (N+1)R_0$, and have resistances equal to

$$R_i = [a + \delta_{i,k}(R - a)]R_0 \tag{4.4}$$

where $a = \frac{N+1-R}{N}$ and $R = 1$ when all the resistances are equal and $R = 30$ for the arrays with the large resistor. The two cases are easy to compare and the difference between them is an idealization of resistance fluctuations that occur in experimentally realized arrays that have the same gap width between the leads but have slight differences in the spacings between particles. This section discusses the form of the IV curves in the linear resistance regime and the shapes of the $P(\Delta E_i)$ distributions in this regime for these two cases. The following section discusses the transition to this regime.

At very large applied voltages, the energy to hop across each junction, ΔE_i, is approximately given by [2]

$$\Delta E_i = E_i^{e-h} + \Phi_i \approx E_i^{e-h} + \Phi_i^{pol} + \Phi_i^{ch} \tag{4.5}$$

and the tunneling rate, Γ_i is approximately given by [3]

$$\Gamma_i \approx \frac{|\Delta E_i|}{e^2 R_i} \ .$$

Although ΔE_i does not depend directly on R_i, the dependence of the tunneling rates, Γ_i, on R_i enable the resistances to determine the time-averaged values of the hopping energies. The resistances can only affect the contributions to ΔE_i due to the excess charges on the array, Φ_i^{ch}, because this is the only term that varies with time when the applied bias voltage is fixed. Due to charge conservation, the time-averaged current through each junction equals the average array current, I:

$$< I_i >= e < \Gamma_i >= I \ . \tag{4.6}$$

Because the array is voltage-biased, the potentials at the leads, V_0 - $V_{N+1} = V$, are related by

$$\begin{aligned} V_0 + \sum_{i=1}^{N} \left(\Phi_i^{ch} + \Phi_i^{pol} \right) &= V_{N+1} \\ \sum_{i=1}^{N} \left(\Phi_i^{ch} + \Phi_i^{pol} \right) &= V_{N+1} - V_0 = -V \ . \end{aligned} \tag{4.7}$$

We can solve for a set of array hopping energies ΔE_i with tunneling rates that satisfy current conservation, Eq. 4.6,

---

[2] At large voltages, disorder can be ignored because $\Phi_i^{dis} \ll \Phi_i^{ch} + \Phi_i^{pol}$.

[3] The orthodox tunneling rate approximately reduces to the zero temperature expression, Eq. 4.3, when the voltages make the magnitudes of the tunneling energies fairly large compared to the thermal energy, $|\Delta E_i| \gg kT$.

$$e < \Gamma_i > \approx \frac{|\Delta E_i|}{eR_i} = \frac{|\Phi_i| - E_i^{e-h}}{eR_i} = I^0. \tag{4.8}$$

Solving Eq. 4.8 and Eq. 4.7 simultaneously for Φ_i, and substituting these values into ΔE_i leads to the following values for ΔE_i and I^0:

$$\Delta E_i = -I^0 R_i \tag{4.9}$$

where

$$I^0 = \frac{V - V^0}{\sum_{i=1}^{N+1} R_i} \tag{4.10}$$

and

$$V^0 = \sum_{i=1}^{N+1} E_i^{e-h} . \tag{4.11}$$

V^0 is called the offset voltage. The offset voltage is the voltage at which $I^0 = 0$ and it is almost always greater than the threshold voltage. [4] At large voltages, the IV curves approach the linear resistance form, Eq. 4.10, and the average hopping energies are given by Eq. 4.9.

The only part of the linear resistance current, I^0, that depends on the capacitances of the junctions is the offset voltage, V^0. The dependence of I^0 on the capacitances can be removed by normalizing the current and the voltage by the offset voltage:

$$i^0 = \frac{v - 1}{\sum_{i=1}^{N+1} R_i} \tag{4.12}$$

where $i^0 = I^0/V^0$ and $v = V/V^0$. Fig. 4.6 shows the normalized $i - v$ curves for arrays with onsite interactions and with long range interactions ($d/r^{isl} = 10$ and $d/r^{isl} = 0.5$) with resistances given by Eq. 3.14 with $R = 1$ and $R = 30$. At large

---

[4] The only case when $V^0 = V_T$ is when interactions are onsite and there is no disorder. In this case, all the junctions are up-steps ($\Phi_i^{dis} = 0$) and $V_T = \sum_{i=1}^{N+1} E_i^{e-h} = V^0$.

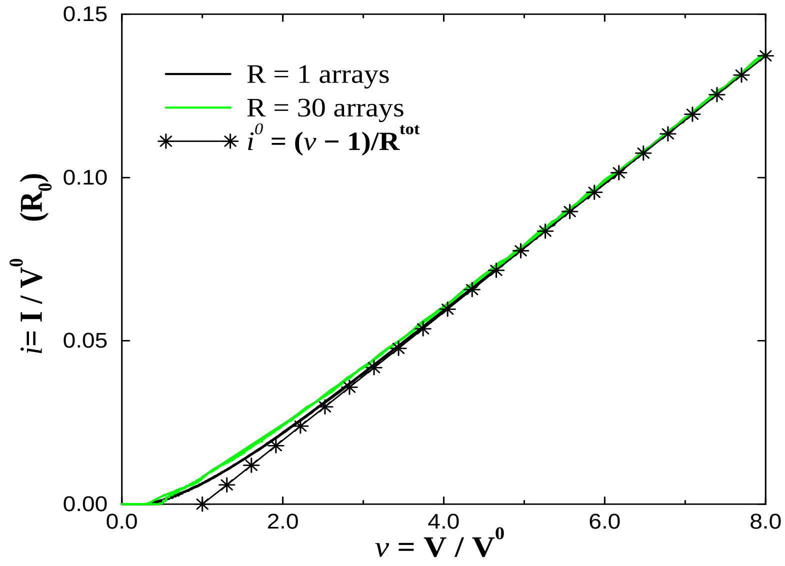

Figure 4.6: *Normalized $i - v$ curves of 50-island arrays.* The resistances of the junctions are described by Eq. 3.14. At large voltages, the $i - v$ curves of arrays with onsite and long range ($d/r^{isl} = 10$ and $d/r^{isl} = 0.5$) interactions are the same and approach the linear resistance form for the current (i^0). The curves due to arrays with different interactions are not distinguished by color or line style because they overlap.

voltages, the normalized $i - v$ curves for the arrays in Fig. 4.6 all overlap because they share the same total resistance. Inserting a large resistance in the middle of the arrays causes the $i - v$ curves to approach the linear resistance current i^0 at larger voltages than the arrays with equal resistance junctions.

Fig. 4.7 shows $P(\Delta E_i)$ at applied voltages that are multiples of the offset voltage, V^0, for arrays that all have equal junction resistances, $R_i = R_0$, and different ranges of interactions. All the arrays reached the limit described by Eq. 4.9 by $V \approx 2V^0$. When the arrays reach this limit, the distributions of tunneling energies are centered at $\Delta E = I^0 R_0$ because all the array junctions have the same resistance. Due to the dependence of V^0 on the excitonic energies, E_i^{e-h}, arrays with stronger interactions (smaller spacing d/r^{isl}) reach the linear resistance regime at smaller applied voltages. See Fig. 4.9, Fig. 4.10 and Fig. 4.11.

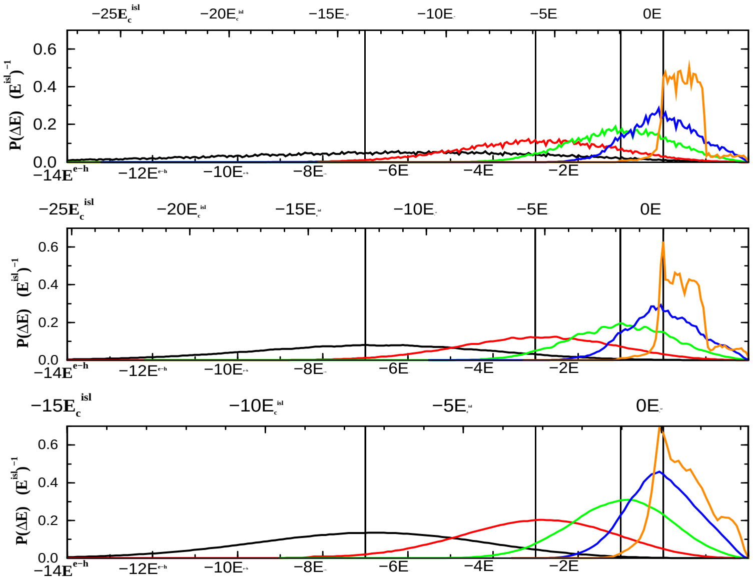

Figure 4.7: *Probabibility distribution of bulk junction hopping energies for 50-island arrays with equal junction resistances $R_i = R_0$.* The top, bottom and middle panels correspond to arrays with onsite interactions and with long range interactions and spacings, $d/r^{isl} = 10$ and $d/r^{isl} = 0.5$, respectively. The applied voltages for $P(\Delta E_i)$ in all the panels from left to right equal $(8, 4, 2, 1, 0.5)V^0$. V^0 equals $100.04E_c^{isl}$, $91.73E_c^{isl}$, and $55.94E_c^{isl}$ in the top, middle, and bottom arrays. When the distributions are centered at the guidelines, drawn for each voltage at $\Delta E_i = I^0 R_i$, the arrays are in the linear resistance regime. The x-axes are labeled in units of $E_c^{isl} = 1/2C_0$ and in units of $E^{e-h} = \sum_{i=1}^{N+1} E_i^{e-h}/(N+1)$.

Fig. 4.8 shows how the tunneling energies, $P(\Delta E_i)$, evolve with voltage for arrays with one large resistor in the middle of the array. In the linear resistance regime, these distributions have two peaks that correspond to the two resistance values, Eq. 4.4, in these arrays, located at $\Delta E = I^0(a) = 0.42R_0$ and $\Delta E = I^0(R-a) = (30-0.42)R_0$. The distributions approached the linear resistance values of ΔE_i at larger voltages than the equal resistance arrays, $V \approx 8V^0$. Fluctuations in the junction resistances can prolong the transition to the linear resistance regime. This transition is discussed in the next section.

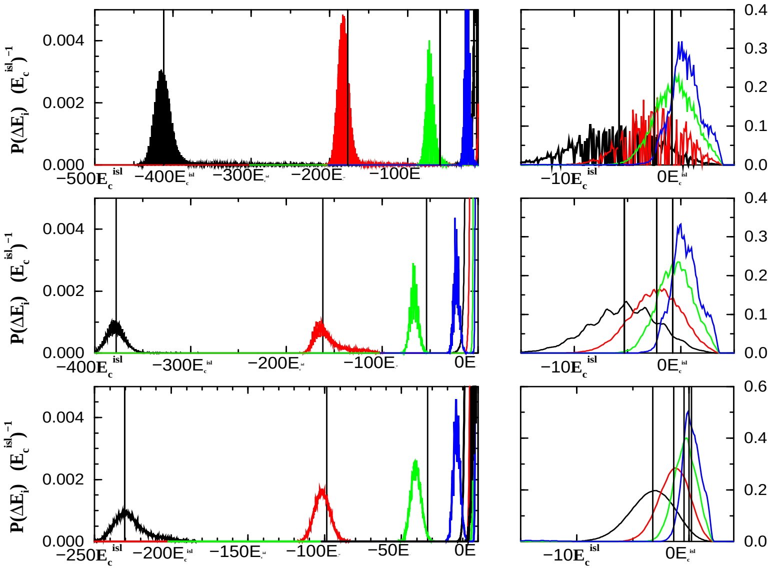

Figure 4.8: *Probability distribution of bulk junction hopping energies for 50-island arrays with unequal junction resistances (Eq. 3.14 with $R = 30$).* The top, bottom and middle panel correspond to arrays with onsite interactions and with long range interactions and spacings, $d/r^{isl} = 10$ and $d/r^{isl} = 0.5$, respectively. The applied voltages for $P(\Delta E_i)$ in all the panels from right to left equal $(8,4,2,1)V^0$. V^0 equals $100.04E_c^{isl}$, $91.73E_c^{isl}$, and $55.94E_c^{isl}$ in the top, middle, and bottom panels. The left and right panels focus on the part of $P(\Delta E_i)$ due to the junction with large resistances and the junctions with small resistances respectively. When the distributions are centered at the guidelines, drawn for each voltage at $\Delta E_i = I^0 R_i$, the arrays are in the linear resistance regime.

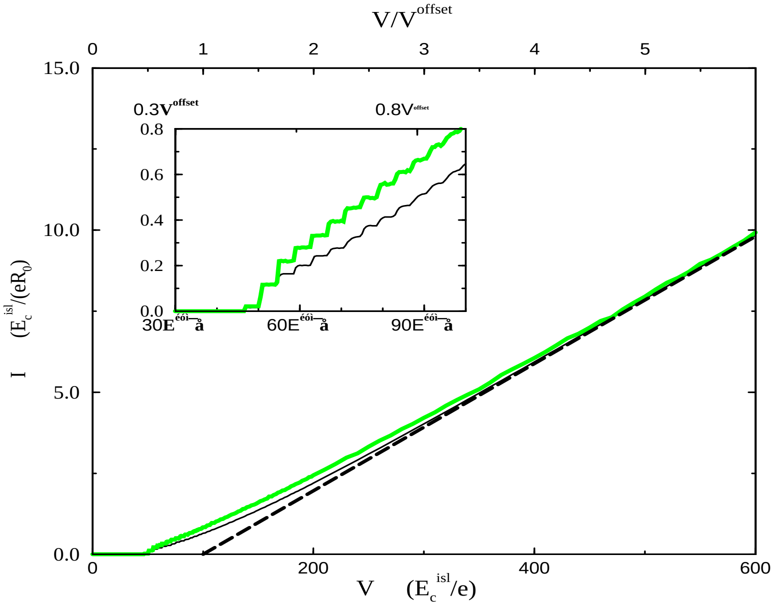

Figure 4.9: *IV curves for 50-island arrays with onsite interactions interactions and equal and unequal junction resistances.* The arrays with thin (thick) lines have junction junction resistances described by Eq. 3.14 with $R = 1$ ($R = 30$). The dashed line is a guideline that shows the form of the IV curves in the linear resistance regime (see Eq. 4.8).

4.4 Intermediate regime

At voltages in between the two linear regimes at high and low voltages, the current depends on the applied voltage in two different ways. At voltages close to the threshold, the current has a step-like dependence on the applied voltage. At larger voltages, the current depends more smoothly on V and approaches the linear resistance current I^0 from above ($I > I^0$). The following section compares how arrays with equal resistances and arrays with all equal resistances except for one large resistance in the middle of the arrays transition between the two linear regimes.

At voltages larger than yet extremely close to the threshold, the current is dominated by one or two processes (bottlenecks). Sec. 4.2 discussed how this leads to linear IV scaling behavior. Above the bottleneck regime, the current is dominated by multiple processes that are slow in the sense that the energies of these processes

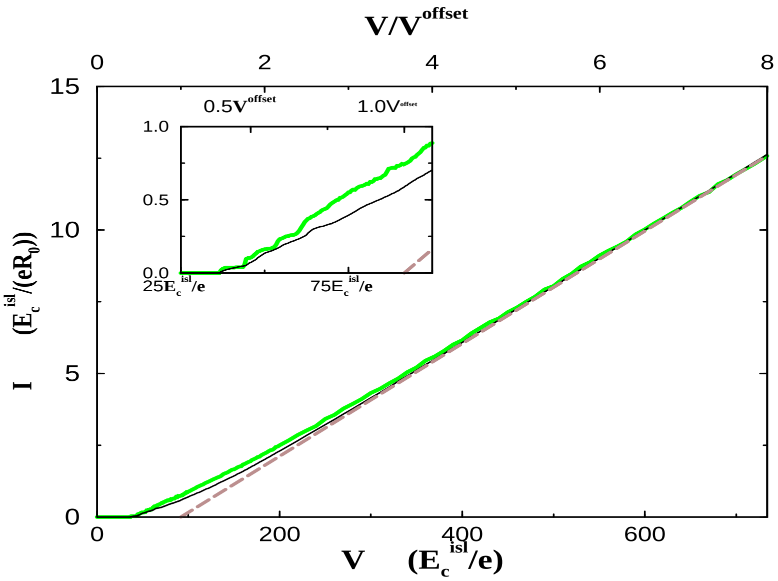

Figure 4.10: *IV curves for 50-island arrays with long range interactions ($d/r^{isl} = 10$) and equal and unequal junction resistances.* The arrays with thin (thick) lines have junction junction resistances described by Eq. 3.14 with $R = 1$ ($R = 30$). The dashed line is a guideline that shows the form of the IV curves in the linear resistance regime (see Eq. 4.8).

have values associated with small tunneling rates, $-\delta < \Delta E_i < 0$ where δ is a small number. When the current is dominated by slow steps the slope of the IV curves is a time-weighted average of the set of Λ_i/R_i that correspond to the slow steps. $\Lambda_i = \Phi_i^{pol}/V$ is the fraction of the total applied voltage V that drops across the i-th junction. Λ_i/R_i is the voltage derivative of the hopping energy of a junction, $\partial\Delta E_i/\partial V$, when the potential gradient of the junction due to charges on the array are only weakly dependent on the applied voltage, $\partial\Phi_i^{ch}/\partial V \approx 0$.

Arrays with onsite interactions have well-defined steps because $\Lambda_i = 0$ across the bulk junctions. In the bottleneck regime, there is still linear scaling for arrays with onsite interactions because the polarization potential gradient is finite across the contact junctions, $\Lambda_1 \neq 0$ and $\Lambda_{N+1} \neq 0$. At voltages above the bottleneck regime, processes that move charge over the bulk junctions begin to dominate current flow. As a result, the IV curves have flat regions (regions with $\partial I/\partial V = 0$) that

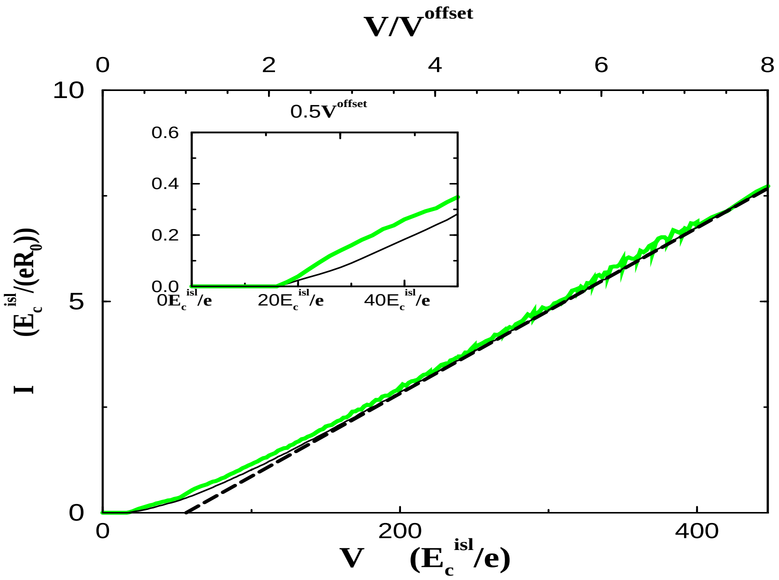

Figure 4.11: *IV curves for 50-island arrays with long range interactions ($d/r^{isl} = 0.5$) and equal and unequal junction resistances.* The arrays with thin (thick) lines have junction junction resistances described by Eq. 3.14 with $R = 1$ ($R = 30$). The dashed line is a guideline that shows the form of the IV curves in the linear resistance regime (see Eq. 4.8).

are broken up by regularly spaced jumps in current that are spaced $2E_c^{isl}$ apart. See inset of Fig. 4.9. The current rises abruptly at voltages that allow the average charge that resides on the contact islands to increase by one (sometimes two if the array is symmetrically biased). Increasing the numbers of charges at the edges of the arrays increases the sizes of the charge gradients across the bulk junctions that create potential drops that drive current through the bulk junctions.

When interactions are long range, the current can have step-like features at voltages immediately above the threshold. See insets of Fig. 4.10 and Fig. 4.11. These features are not as well defined and regular as they are in the onsite case, but they can be understood in terms of the onsite case. The slopes of the flatter regions of the IV curves do not equal 0 when there are long range interactions because $\Phi^{pol} \neq 0$ across all junctions. The slope can be depressed when the current is dominated by slow steps that occur across junctions with small Φ_i^{pol}. The edges of the steps are not as well defined as they are in the onsite case because increasing the applied voltage always increases the sizes of the potential drops across all junctions because Φ_i^{pol} is finite across all junctions.

Fig. 4.7 shows how the tunneling energies of arrays with onsite and long range interactions evolve at voltages above the bottleneck regime. At the smallest displayed voltages, $V = 0.5V^0$, the tunneling energy probability distributions, $P(\Delta E_i)$, have shoulders that just extend into the region of energies that allow tunneling events, $\Delta E_i < 0$. The probabilities embedded in this distribution are time-averaged when charges are not stationary. See Sec. 6.3. This means that regions of energy that are both negative and have large $P(\Delta E_i)$ values contribute most to the average tunneling rates across junctions. When the distributions have shoulders that just lean into small negative values of ΔE_i, then the current is dominated by processes with small tunneling rates (slow steps). At the next displayed voltages, $V = V^0$, the shoulders disappear. The distributions have large probabilities associated with a larger range of energies with finite tunneling rates. These shapes indicate that slow steps no longer dominate current flow. As result, the step-like features in the IV curves are absent at these voltages. See Fig. 4.9, Fig. 4.10, and Fig. 4.11.

Introducing a large resistor in the middle of the array while holding the total resistance constant increases the current because the slow steps occurs across the junctions with smaller resistance, $a = 0.42R_0 < R_0$. Although the current is larger, the step-like features are more defined and persist over a wider range of voltages than the arrays without the large resistor. The slow step region is prolonged because the uneven set of resistances favor tunneling events that create an uneven set of voltage drops (uneven Φ_i^{ch}) across the array junctions. Most of the applied voltage drops across the junction with the large resistance. The slow steps occur across the remaining junctions that have much smaller voltage drops. It takes larger applied voltages to drive the tunneling energies across all junctions to levels that support large tunneling rates. Fig. 4.8 shows how the tunneling energies across the junctions with the smaller resistance cluster around energies associated with smaller rates. At voltages as large as $V = V^0$, all the distributions still have shoulders near $\Delta E_i = 0$ that indicate that slow steps still continue to strongly influence the current.

At larger voltages, the current varies smoothly with applied voltage and has a slope that approaches the linear resistance slope, $\partial I / \partial V = (R_{tot})^{-1}$. The current in this region is always greater than the linear resistance current, I^0, because of fluctuations in the tunneling energies due to moving charges. Recall that the total voltage drop is distributed over the junctions in the following way,

$$\sum_{i=1}^{N+1} \left(\Phi_i^{ch} + \Phi_i^{pol} \right) = V_{N+1} - V_0 = -V$$

at all instances. When the voltage is fixed, Φ_i^{pol} does not vary in time. However each time charges move, Φ_i^{ch} changes across individual junctions and redistributes the total applied voltage across junctions in ways that allow current to flow. The contributions of excess charges to the potential gradients enable the threshold voltages to occur at values smaller than the offset voltages. These contributions also create the large spreads in the energy values shown in the $P(\Delta E_i)$ distributions. Due to current conservation, the $P(\Delta E_i)$ distributions tend to peak at values for the energy that lead to equal current values through all junctions, $\Delta E_i = I^0 R_i$. The actual average current, I is related to the distributions by,

$$I = e \langle \Gamma_i \rangle \propto - \int_{-\infty}^{0} \Delta E_i P(\Delta E_i) d(\Delta E_i) \; .$$

The actual mean of the energies in $P(\Delta E_i)$ is close to $\Delta E_i = -I^0 R_i$ at nearly all voltages. However the mean of the energies that contribute to the current, Eq. 4.4, is smaller than mean of the entire distribution and this leads to larger currents,

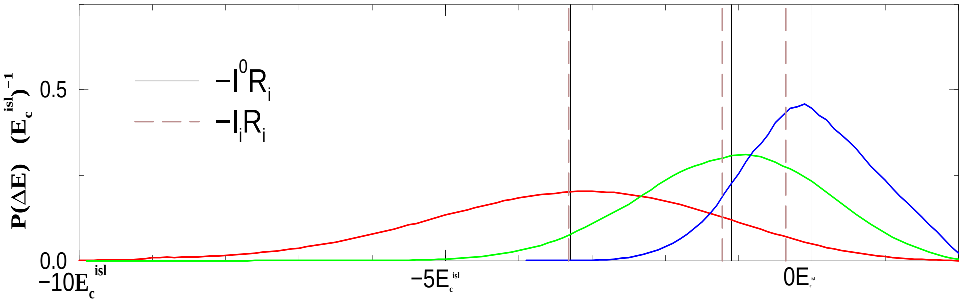

Figure 4.12: *Evolution of* $P(\Delta E_i)$ *at intermediate voltages for a 50-island array with spacing* $d/r^{isl} = 0.5$. The applied voltages of the distributions from left to right are $(4,\ 2,\ 1)V^0$ where $V^0 \approx 55.94E_c^{isl}$. The solid guidelines show the predicted mean for ΔE_i in the linear resistance regime. The dashed guidelines show the effective tunneling energy, Eq. 4.4 associated with the actual current flow through the arrays.

$I > I^0$. At large enough applied voltages, the two means are nearly equal and the array current equals the linear resistance current. Fig. 4.12 shows how these two means approach each other as the applied voltage increases for an array with equal junction resistances.

When one of the resistances in the bulk of the array is much larger than the others, the current approaches the linear resistance current, I^0, at larger voltages. The average energy of the probability distributions associated with the junctions with smaller resistance $\Delta E_{i \neq k} = 0.42R_0$ are still well described by $\Delta E_i = -I^0 R_i$ when $V > V^0$ (Fig. 4.8). The peaks of the distribution due to the large resistance junction $R_k = 30R_0$ occur at values smaller than $\Delta E_k = -I^0 R_k$ and they approach these values when V is very large. Again, the actual current is larger than I^0 until the current approaches I^0 because of fluctuations in the tunneling energies due to moving charges on the array. The junctions whose potentials are most affected by these fluctuations are the junctions with small resistance because the voltage drops across these junctions tend to be smaller than the voltage drops across junctions with larger resistances. At voltages less than $8V^0$, the average energy associated with finite tunneling rates, $\langle \Delta E_i < 0 \rangle$, tends to be smaller than the average over

Range	$\langle V_T\rangle/E_c^{isl}$	$2V^0/E_c^{isl}$	$8V^0/E_c^{isl}$	$v_{min,1}$	$v_{min,2}$
onsite	49.84	200.08	800.32	~ 3	~ 15
$d/r^{isl} = 10$	42.96	183.46	733.84	~ 3	~ 16
$d/r^{isl} = 0.5$	19.78	111.88	447.52	~ 5	~ 22

Table 4.3: *Approximate minimum voltages for the linear resistance regimes of 50-island arrays with varied interaction strengths.* $v_{min,1}$ and $v_{min,2}$ are the reduced voltages, $v = (V - V_T)/V_T$, associated with $2V^0$ and $8V^0$. These values approximate the minimum voltages required to reach the linear resistance regime for arrays with equal resistances and for arrays with equal resistances except for one large resistance in the middle of the array.

all tunneling energies $\langle \Delta E_i\rangle \approx -I^0 R_i$ because a large part of the distributions correspond to tunneling energies that forbid hops ($\Delta E_i > 0$). At very large voltages ($V = 8V^0$), the fraction of $P(\Delta E_i)$ due to positive energies becomes small enough that the array current can approach I^0. As the array current approaches I^0, the peak in $P(\Delta E_i)$ due to the junction with large resistance approaches its linear resistance value.

4.5 Conclusions

We have numerically measured two linear scaling regimes that occur at very small and very large voltages. The voltage ranges for these two regimes do not coincide with the voltage ranges typically used to characterize the IV characteristics of experimentally realized arrays.

The linear scaling of the low voltage regime is due to the current-voltage characteristics of a single junction, the bottleneck, that dominates current flow at these voltages. The slope of the bottleneck current is set by the resistance and the polarization potential gradient across the bottleneck junction, $\partial I/\partial V = \Lambda_{bn}/R_{bn}$. The slope of the IV curve is unrelated to the series resistance of the 1-D system because the threshold voltage and the bottleneck regime is primarily an electrostatic effect. Coulomb blockade suppresses the motion of charges enough that the time-averaged potential gradients across the array junctions nearly equal the electrostatic potential gradients due to the leads and the static configuration of charges prior to a hop across the bottleneck. The bottleneck approximation is valid at voltages very close to the thresholds of both 1-D and 2-D arrays. In the latter case, the approximation is valid when charges move along a single 1-D path that spans the 2-D arrays. We found that the voltages at which this approximation breaks down are close enough to the threshold that this regime may be experimentally irrelevant. For all the arrays we modeled, the linear scaling vanishes at voltage values, Table 4.2, too small to lie within the ranges of reduced voltages typically used to measure the scaling of the IV curves of arrays in experiments, Table 4.1.

At very large voltages, the IV curves are linear and described by

$$I^0 = \frac{V - V^0}{\sum_{i=1}^{N+1} R_i}$$

where the offset voltage is given by

$$V^0 = \sum_{i=1}^{N+1} E_i^{e-h} = \sum_{i=1}^{N+1} \left(\frac{1}{2}(C_{i,i}^{-1} + C_{i-1,i-1}^{-1}) - C_{i,i-1}^{-1} \right) .$$

Eq. 5.1.3 arises from current conservation among the currents through each junction and the average current through the entire array. The offset voltage sets the scale of voltages large enough for the linear resistance regime to be valid at small temperatures. We found that arrays with uniform resistances reach this regime at $V > 2V^0$ and arrays with uniform resistances except for one larger resistance in the middle of the array did not reach this regime until $V > 8V^0$. This suggests that as the length of the array increases and fluctuations in the junction resistance increases, the voltages required to reach this regime increase. For arrays with 50 islands, we found that the linear resistance regime began at reduced voltage values, Table 4.3, larger than the typical reduced voltages used to measure IV scaling exponents in experiments, Table 4.1.

We found that the range of reduced voltages used to measure the scaling exponents of IV curves in experiments coincides with an intermediate regime in between the linear bottleneck and the linear resistance regimes. The features of this regime include a step-like dependence of the current on small voltages followed by a smooth transition down to the currents described by the linear resistance IV relationship, Eq. 5.1.3. The size of this transitional regime decreases as the range of interactions increase and increases as the resistances become less homogeneous. The delay in reaching the standard form for the IV curves is caused by large variations in the potential gradients caused by excess charges moving among the nanoparticles. It is possible that the wide variations in the measured scaling exponents are due to the particulars of arrays transitioning between regimes where the current is controlled by Coulomb blockade to currents that are controlled by dynamic effects.

Chapter 5

Summary and Outlook

5.1 Summary

5.1.1 Models of Nanoparticle Arrays

We developed a realistic model for the interactions among charges residing on a 1-D array of nanoparticles sandwiched between two voltage-biased leads. We wrote the free energy of this system of charges using an inverse capacitance matrix that includes the nanoparticles and the leads and treating the leads as real (not ideal) voltage sources. We defined a new time scale in order to separate the work done by the battery from the work done by charges in our system.

We wrote the tunneling energies to hop across junctions in terms of potential gradients that separate the contributions due to the applied voltage values, V_0 and V_{N+1}, and the contributions due to the charges on the array, $\{Q_i\}$. The polarization potential gradient, Φ_i^{pol}, only depends on the applied voltage values and describes the polarization of the junctions by the leads biased at V_0 and V_{N+1} in the absence of excess charges on the nanoparticles, Eq. 2.4. The charged potential gradient, Φ_i^{ch} includes all the potential gradients across junctions due to excess charges on the nanoparticles, Eq. 2.2.1. Terms that describe the fluctuations in the potentials at the source and drain leads are included in Φ_i^{ch}. The inclusion of these terms leads to a renormalization of the interactions among the charges on the array that describes how these interactions are changed by induced charges on the leads. Modeling the potential gradients in this way enabled us to study how the voltage drops across junctions without making any simplifying assumptions about how the applied voltage distributes itself across junctions.

We modeled charged disorder by simulating the annealing of the system to a global electrostatic equilibrium state while both leads were grounded. We used the charges associated with this equilibrium state to define the potentials at each nanoparticle due to random charged background disorder, ϕ_i^{dis}. The properties of the global equilibrium state set natural limits on the disorder potentials, ϕ_i^{dis}, and on the disorder potential gradients, Φ_i^{dis}. See Eq. 2.7 and Eq. 2.8. Our description of the Coulomb interactions among the annealing charges led to correlations among the disorder potentials.

5.1.2 Thresholds of Nanoparticle Arrays

We have determined the threshold dependence on array length in number of nanoparticles, N, and on the biasing asymmetry, α, for arrays with long range interactions and onsite interactions in the presence and absence of disorder.

We found that the average threshold of disordered arrays (averaged over many configurations of disorder) scales linearly with array length, N, for arrays with onsite interactions and with long range interactions. Our average threshold results for the onsite case agree with Middleton and Wingreen's (MW) results. We used an analogy to the onsite threshold to derive an upper limit for the threshold in the long range case:

$$\langle V_T \rangle = \langle E_i^{e-h} \rangle \langle N_{up} \rangle = \langle E_i^{e-h} \rangle (N/2)$$

where E_i^{e-h} is given by Eq. 2.2.1. Eq. 5.1.2 reduces to MW's equation, Eq. 3.1.1, when interactions are extremely short range [35]. When interactions are long range, this expression describes how the slope, $\partial\langle Vt\rangle/\partial N$, decreases as interaction strength increases due to decreasing the spacing between nanoparticles. Eq. 5.1.2 more closely approaches the thresholds we determined numerically than other analytical predictions for the thresholds of arrays with long range iteractions. See Table 3.2. By studying how distributions of tunneling energies, $P(\Delta E_i)$, evolve as voltages approach the threshold, we were able to verify that Eq. 5.1.2 overestimates the threshold because it is based on a conservative assumption for how newly injected charges modify the potential gradients across array junctions. The assumption is that only one newly injected charge resting on an island on one side of a junction modifies the potential gradient across any given junction. In reality, long range interactions allow multiple charges at multiple locations on the array to modify the potential gradients across junctions.

Our numerical results for $\langle V_T(N)\rangle$ at spacings that are comparable to spacings in real experiments ($d/r^{isl} = 0.5$) are in reasonable agreement with experimental measurements of the threshold on 1-D arrays. Our numerical results overestimate the thresholds of quasi-1-D arrays. It is possible for the thresholds of quasi-1-D arrays to be smaller than the thresholds of 1-D arrays because charges can access pathways in these arrays that are absent in the 1-D case that enable them to avoid some barriers to current flow. See Fig. 3.9.

In the absence of disorder, we found that the threshold has a step-like dependence on array length (Fig. 3.3) in the limit of onsite interactions due to two ways to initiate current through arrays with onsite interactions. In one way, current is initiated by the injection of a single charge across one of the contact junctions. The other way requires two charges of opposite sign to be injected through the two opposing contact junctions. These two ways for initiating current cause the thresholds of individual arrays with onsite interactions to fluctuate continuously between two limiting values that are separated by $\Delta V_T = 2E_c^{isl}$ in response to changing a biasing asymmetry factor, α, which describes how the applied voltage, V, is distributed between the source and drain leads,

$$\begin{aligned} V_0 &= \alpha V \\ V_{N+1} &= (1-\alpha)V \; . \end{aligned} \tag{5.1}$$

See Fig. 3.2. At zero temperature and in the limit of onsite interactions, the thresholds of arrays without disorder are greater than the thresholds of arrays with disorder because charge gradients must build up across all bulk junctions (junctions between neighboring islands) in the clean case instead of just the bulk junctions with up-steps (junctions with $\Phi^{dis} > 0$) in the disordered case.

Arrays without disorder and with long range interactions have the smallest thresholds because this threshold corresponds to the minimum voltage that allows a charge to hop across a contact junction into an array with no excess charges. As long as interactions among the leads are not too strong, this threshold increases as the array length increases and also increases as the spacing between islands decreases because these changes decrease the fraction of the applied voltage that drops across the contact junctions (Fig. 3.4). In the limit of very large arrays, this threshold saturates to a value that increases as the spacing between nanoparticles decreases. This is in qualititative agreement with the soliton threshold proposed by Likharev, et al. (Eq. 3.1.1); however our results do not quantitatively agree because we do not use the soliton model to derive our inverse capacitance matrices. See Table 3.1. Increasing the biasing asymmetry factor (increasing $|\alpha - 1/2|$ in Eq. 5.1) causes the thresholds of clean arrays with long range interactions to decrease smoothly because these changes cause more of the applied potential to drop across the contact junction that sets the threshold.

When the arrays include disorder, varying α causes the thresholds to fluctuate with less regularity than disordered arrays with onsite interactions because the long range interactions allow any junction (instead of just the contact junctions) to house the first tunneling event that initiates the first sequence of hops that transfer charge between the leads. Increasing the range of interactions (by decreasing the spacing between nanoparticles) decreases the dependence of the threshold on the biasing asymmetry factor α.

Finally we examined how temperature affects the thresholds of disordered arrays. As long as the temperature is not too large, $kT < 0.1E_c^{isl}$, we can define a threshold using a peak in the second derivative of the IV curves. In the temperature range where we are able to define a threshold, our results are in good agreement with Elteto, et al.'s model for the finite temperature threshold [17]. See Fig. 3.18.

Arrays with onsite interactions can not be described by this model because of the way temperature affects the local thresholds of these arrays. At zero temperature, charge gradients, $\delta Q_i = -1$, must build across any bulk junctions with up-steps ($\Phi^{dis} \geq 0$) in order to create potential gradients that facilitate current flow that the applied potentials can not directly supply because these potentials drop completely across the contact junctions. Finite temperatures allow charges to hop across the bulk junctions in the absence of these charge gradients. As a result, steps appear in the IV curves at voltages below the zero temperature threshold. See Fig. 3.19. The steps occur at voltages that allow the time-averaged charge at the contacts to increase by one. The flat regions in between the steps are due to current flow that is dominated by the times spent hopping across the bulk junctions; these times are independent of the applied voltage because the applied voltage does not directly drop across the bulk junctions in the onsite limit.

5.1.3 Dynamics of Nanoparticle Arrays

We have numerically measured two linear scaling regimes that occur at very small and very large voltages. The voltage ranges for these two regimes do not coincide with the voltage ranges typically used to characterize the IV characteristics of experimentally realized arrays.

The linear scaling of the low voltage regime is due to the current-voltage characteristics of a single junction, the bottleneck, that dominates current flow at these voltages. The slope of the bottleneck current is set by the resistance and the polarization potential gradient across the bottleneck junction, $\partial I/\partial V = |\Lambda_{bn}|/R_{bn}$ where $\Lambda_{bn} = \Phi_{bn}^{pol}/V$. The slope of the IV curve is unrelated to the series resistance of the 1-D system because the threshold voltage and the bottleneck regime is primarily an electrostatic effect. Coulomb blockade suppresses the motion of charges enough that the time-averaged potential gradients across the array junctions nearly equal the electrostatic potential gradients due to the leads and the static configuration of charges prior to a hop across the bottleneck. The bottleneck approximation is valid at voltages very close to the thresholds of both 1-D and 2-D arrays. In the latter case, the approximation is valid when charges move along a single 1-D path that spans the 2-D arrays. We found that the voltages at which this approximation breaks down are close enough to the threshold that this regime may be experimentally irrelevant. For all the arrays we modeled, the linear scaling vanishes at voltage values, Table 4.2, too small to lie within the ranges of reduced voltages typically used to measure the scaling of the IV curves of arrays in experiments, Table 4.1.

At very large voltages, the IV curves are linear and described by

$$I^0 = \frac{V - V^0}{\sum_{i=1}^{N+1} R_i}$$

where the offset voltage is given by

$$V^0 = \sum_{i=1}^{N+1} E_i^{e-h} = \sum_{i=1}^{N+1} \left(\frac{1}{2}(C_{i,i}^{-1} + C_{i-1,i-1}^{-1}) - C_{i,i-1}^{-1} \right) .$$

Eq. 5.1.3 arises from current conservation among the currents through each junction and the average current through the entire array. The offset voltage sets the scale of voltages large enough for the linear resistance regime to be valid at small temperatures. We found that arrays with uniform resistances reach this regime at $V > 2V^0$ and arrays with uniform resistances except for one larger resistance in the middle of the array did not reach this regime until $V > 8V^0$. This suggests that as the length of the array increases and fluctuations in the junction resistance increases, the voltages required to reach this regime increase. For arrays with 50 islands, we found that the linear resistance regime began at reduced voltage values, Table 4.3, larger than the typical reduced voltages used to measure IV scaling exponents in experiments, Table 4.1.

We found that the range of reduced voltages used to measure the scaling exponents of IV curves in experiments [18, 39, 4, 2, 42] coincides with an intermediate regime in between the linear bottleneck and the linear resistance regimes. The features of this regime include a step-like dependence of the current on small voltages followed by a smooth transition down to the currents described by the linear resistance IV relationship, Eq. 5.1.3. The size of this transitional regime decreases as the range of interactions increase and increases as the resistances become less homogeneous. The delay in reaching the standard form for the IV curves is caused by large variations in the potential gradients caused by excess charges moving among the nanoparticles. It is possible that the wide variations in the measured scaling exponents are due to the particulars of arrays transitioning between regimes where the current is controlled by Coulomb blockade to currents that are controlled by dynamic effects.

5.2 Future Work

Our research does not address the dimensionality of many nanoparticle systems (e. g. quasi-1-D and 2-D systems) and it does not include all the types of disorder seen in experiments. More types of structural disorder can be included by including more variations in the junction resistances and by expanding the inverse capacitance calculations to include spheres arranged in quasi-1-D and 2-D arrangements. In principle, the inverse capacitance matrices of these higher-dimension systems can be used to rewrite the potential gradients in our model due to the applied voltages, Φ_i^{pol}, due the charges on the array, Φ_i^{ch}, and due to charged disorder,Φ_i^{dis}. Separating the potential gradients using these expressions may help to untangle the effects due to applied voltages, accumulated charge gradients, and charged disorder in these systems.

This work focused primarily on the zero temperature behavior of 1-D arrays. Finite temperatures wash out Coulomb blockade effects at low voltages. We began to characterize these effects by studying the peaks in the IV curves at small finite temperatures. These peaks are quickly washed out at small temperatures. The finite temperature low voltage characteristics of these systems can be further studied by studying the temperature dependence of the zero-bias conductance, $G_0(T)$. Studying this quantity can teach us if long range interactions and sequential tunneling can lead to effects that are similar to variable range hopping effects. Kaplan,et al. (2003) studied the density of states and the zero bias conductance of 1-D systems [26] using numerical simulations of sequential tunneling through systems with interactions described by the soliton model with very large screening lengths. They found a Coulomb gap in the density of states, a feature shared by the Efros-Schlovskii model for variable range hopping. However, they did not find the Efros Schlovski dependence in the conductance, $G_0(T) \propto \exp(-(T_0/T)^{1/2}$; instead they found an Arrhenius dependence, $G_0(T) \propto \exp(-U_0/(k_B T))$.

This work included structural disorder in a very simple way. We compared the behavior of systems with homogeneous resistances to systems with homogeneous resistances except for one large resistance in the middle of the array. We were able to see that this change had no effect on the zero temperature threshold because this is an electrostatic effect. This work can be extended by studying how introducing fluctuations in the resistance affect the finite temperature thresholds. Cordan et al. (2000) [9] studied how the dependence of the threshold on temperature is affected by variations in the spacings between nanoparticles, but they did not include charged disorder in their model. It would be interesting to check how structural disorder and charged disorder affect this relationship because both types of disorder affect the thresholds of arrays in experiments.

Finally, it would be interesting to see how including a more realistic model of structural disorder would affect the scaling relationships of the IV curves. When we introduced a single large resistance in the middle of the arrays, we found that this increased the voltage at which arrays reached the linear resistance regime. In actual experiments, large fluctuations in the junction resistances are unavoidable because the tunneling resistance is exponentially related to the distance between nanoparticles. It would be interesting to check how varying the tunneling resistances in this way affects the size of the transition regime between the linear regimes at low and high voltages. It is possible that this regime is large enough to explain why arrays in experiments [18, 39, 4, 2] sometimes do not reach the linear IV behavior that is the expected relationship at large voltages because it is a consequence of current conservation.

Chapter 6

Appendix

6.1 Monte Carlo Simulations of Transport in Nanoparticle Arrays

This section outlines the numerical algorithm we used to model the motion of charges through 1-D nanoparticle arrays. We conducted Monte Carlo simulations driven by the orthodox tunneling rate expression,

$$\Gamma_i^{\pm} = \frac{1}{e^2 R_T} \frac{\Delta E_i^{\pm}}{1 - exp(\Delta E_i^{\pm}/k_B T)} \ , \tag{6.1}$$

where $\Delta E_i^{\pm}$ is the energy for a charge to hop to the right (left) between neighboring conductors indexed i and $i-1$,

$$\Delta E_i^{\pm} = E_i^{e-h} \pm \Phi_i^{pol} \pm \Phi_i^{ch} \pm \Phi_i^{dis} \ .$$

Eq. 6.1 is discussed in detail in Sec. 2.2.

We numerically determined the time evolution of the state of an array of nanoparticles sandwiched between two large metallic leads biased at potentials, V_0 and V_{N+1}. The state of an array consists of the set of charges $\{Q_i\}$ that occupy the array islands and the leads. The array island charges, indexed $i = 1, 2, \ldots, N$, take on integer values because the charges are localized on the dots and can only change in integer increments of the charge of an electron, e. The charge of the islands is modified when an electron or a hole tunnels between two adjacent sites. The charges of the source and drain leads, Q_0 and Q_{N+1}, take on any real value because they are modified discretely via the tunneling of charges or continuously via the charging of the leads by a battery. The charges that maintain the applied potentials, V_0 and V_{N+1}, at the source and drain leads are given by

$$Q_0 = C^2_{gen}\left[C^{-1}_{N+1,N+1}V_0 - C^{-1}_{N+1,0}V_{N+1} - \sum_{i=1}^{N} Q_i\left(C^{-1}_{N+1,N+1}C^{-1}_{i0} - C^{-1}_{N+1,0}C^{-1}_{i,N+1}\right)\right] \tag{6.2}$$

$$Q_{N+1} = C^2_{gen}\left[C^{-1}_{0,0}V_{N+1} - C^{-1}_{N+1,0}V_0 - \sum_{i=1}^{N} Q_i\left(C^{-1}_{00}C^{-1}_{iN+1} - C^{-1}_{N+1,0}C^{-1}_{i0}\right)\right] \tag{6.3}$$

with

$$C^2_{gen} = \left[C^{-1}_{00}C^{-1}_{N+1,N+1} - (C^{-1}_{N+1,0})^2\right]^{-1}$$

The derivation of these expresssion was discussed in Sec. 2.2.

To determine the evolution of the system of charges, $\{Q_i\}$, and to calculate all quantities that depend on $\{Q_i\}$, we performed N_{eq} iterations to equilibrate the system. N_{eq} is a number much greater than one. We performed these iterations to remove the sensitivity of calculated quantities to initial condictions. Following these iterations, we performed N_{evol} iterations while keeping track of the evolution of our state as a function of time $\{Q_i(t)\}$. N_{evol} is a number much greater than N_{eq}. The major steps of each iteration are as follows:

1. Rank all possible tunneling events.

2. Select a tunneling event and let the system evolve in time.

3. Reset the charge on the leads.

Step 1: Rank all possible tunneling events.

We calculated the tunneling rate for every possible tunneling event using Eq. 6.1. The set of possible tunneling events includes right- and leftward hops across all $N+1$ junctions in the array. We ranked each process using its relative tunneling probability,

$$\Gamma_i^{\pm,rel} = \frac{\Gamma_{i,d}^{\pm}}{\Gamma_{tot}} \ , \tag{6.4}$$

where

$$\Gamma_{tot} = \sum_{i=0}^{N+1} \Gamma_i^{\pm} \ . \tag{6.5}$$

We recorded the rankings on a number line between 0 and 1, divided into intervals with widths equal to the relative tunneling probabilities, $\{\Gamma_i^{\pm,rel}\}$.

Step 2: Select a tunneling event and let the system evolve in time.

We choose a tunneling event by using a random number generator (RNG) to select one bin from the number line generated in the previous step that corresponds to a specific tunneling processs. We let the the charge state evolve to reflect the process selected in this step, $\{Q_i\} \to \{Q_i\}'$. We calculate the time step, Δt, associated with this change by using the RNG to select a probability between 0 and 1, P_{stay}, and the following expression, [1]

$$\Delta t = -\frac{\ln(P_{stay})}{\Gamma_{tot}} \ . \tag{6.6}$$

When the numerical run is in equilibration mode, we only record the new state $\{Q_i\}'$. When the numerical run is in calculation mode, we update the time that has elapsed from the beginning of the simulation by adding Δt to a total time, t_{tot}. In addition, we track the evolution of the charge state, $\{Q_i\}$, and update the number of charges that have arrived at the drain, Q_{drain}, if the selected process results in a charge hopping on to or off of the drain lead. After N_{evol} iterations, we use Q_{drain} and t_{tot} to calculate the average current [2] ,

---

[1] Eq. 6.6 comes from the probability for a state to remained uncharged in a time, Δt: $P_{stay} = \exp(-\Gamma_{tot}\Delta t)$.

$$I = \frac{Q_{drain}}{t_{tot}} . \tag{6.7}$$

Step 3: Reset the leads.

The potentials at the source and drain leads fluctuate away from their applied values, V_0 and V_{N+1}, every time the charge state of the array changes. Prior to the next hop, we model the restoration of these potentials to their applied values by a battery by resetting the charges on the source and drain using Eq. 6.2 and Eq. 6.3.

6.2 Methods to Calculate the Inverse Capacitance Matrix

6.2.1 Image Charges Method

The method of images is based on the relation between charges and potentials in capacitively coupled conductors. The charge Q_α induced on a conductor in the presence of N equipotentials at potentials V_β is given by the capacitance matrix $C_{\alpha\beta}$

$$Q_\alpha = \sum_{j=\beta}^{N} C_{\alpha\beta} V_\beta \tag{6.8}$$

The inverse capacitance matrix which enters the free energy, Eq. 2.2.1, is the inverse of the capacitance matrix $C_{\alpha\beta}$. We have calculated the capacitance matrix using some properties of spheres and the fact that the charge in a conductor α produced by a unity potential in a conductor β is equal to the capacitance matrix element $C_{\alpha\beta}$.

---

[2] We check the current values by calculating the currents through multiple junctions. We calculate these currents by tracking the net charges that pass through junctions other than the contact junction closest to the drain and dividing this net charge by t_{tot}.

We have obtained $C^{-1}_{\alpha\beta}$ inverting $C_{\alpha\beta}$. The method of images [46] is the placement of imaginary charges inside the spheres at positions that make the potential everywhere on the surface of the conductor equal a constant.

To determine the positions of the image charges, we exploit two properties of spheres. First, the center of the sphere is equidistant from all points on the surface of the sphere. Using this property, the surface of a sphere of radius R can be set to a potential V by placing an image at the center of the sphere of charge $q = VR$. Second, for every point outside a sphere there is a point inside the sphere for which the ratio of the distances between these two points and any point on the surface of the sphere is a constant. From here it follows that if a charge q_R is located at the outside point, at a distance d_c from the center, an image charge q_I placed at the inside a distance R^2/d_c from the center on the radial line, with charge

$$q_I = -q_R \frac{R}{d_c} \tag{6.9}$$

will set the potential to zero everywhere on the surface of the sphere. We determine the $(N+2) \times (N+2)$ capacitance matrix, column by column, by determining the set of image charges that sets the potentials of the spheres to $V_\alpha = \delta_{\alpha\beta}$. The capacitance matrix elements $C_\alpha \beta$ are given by the sum of all the charges in sphere α. To set the potential of the β sphere, with radius R_β to one, we place a charge with magnitude R_β at the center of this sphere x_β. The remaining spheres are grounded by placing images inside each sphere with charges

$$q_\nu = -\frac{R_\nu q^{old}}{|x_{q_{old}} - x_\nu|} \tag{6.10}$$

at positions

$$x_{q_\nu} = x_\nu + \frac{R_\nu^2}{x_{q_old} - x_\nu} \; . \tag{6.11}$$

Here q^{old} and $x_{q_{old}}$ are the value and the position of the charge which creates the inhomogeneous potential that we want to compensate and R_ν and x_ν are the radius and position of the center of the sphere to which we add the image charge q_ν. These image charges are added to all the spheres except the one in which q_{old} is placed. The charges that have been added generate new inhomogeneous potentials at the rest of the spheres and have to be compensated following the same method. This process repeats iteratively for all the charges added to all the spheres. During each iteration n, the number of new images required to compensate the potential of the other spheres approximately equals $(N+1)^n$. We eliminate some of the images by discarding images with a magnitude that is smaller than a suitable cutoff value, q_{cutoff}. We required q_{cutoff} to be small enough that the relative diffferences between the matrix elements generated with the cutoff value q_{cutoff} and by a larger cutoff value $q'_{cutoff} = 10q_{cutoff}$ are less than one percent.

The method of images can be used to determine the capacitance matrix for any geometric configuration of spheres. Although the algorithm for generating images is straightforward, the number of images required to calculate a column $C_{\alpha\beta}$ makes the numerical implementation of this technique nontrivial. While computer memory problems can be solved, the computation time is too large to tackle those cases with very large arrays and electrodes and small distance between conductors.

6.2.2 High-order multipoles method

Following Wehrli, et al. [49], the energy of the system, given by

$$F = \frac{1}{2} \sum_{\alpha,\beta=0}^{N+1} Q_\alpha C^{-1}_{\alpha\beta} Q_\beta \ , \tag{6.12}$$

can be rewritten in terms of the higher-order multipolar charges induced by the charges on the conductors as

$$F = \frac{1}{2} \sum_{\alpha,\beta,l,m,l',m'} Q^{\alpha,*}_{l,m} G^{\alpha\beta}_{l,m,l',m'} Q^{\beta}_{l'm'} \ . \tag{6.13}$$

Here Greek indices denote the conductors, l and l' denote the order of the multipole, and $m = -l, \ldots, l$ and $m' = -l', \ldots, l$ denote the azimuthal number. This matrix G is hermitian with respect to the exchange of α, l, m and β, l', m'. Using the linear response form for the induced multipoles, the higher-order multipolar charges, $Q^{\alpha}_{l,m}$, can be expressed in terms of the (monopolar) charges on the conductors $Q_{\gamma} = Q^{\gamma}_{00}$, as

$$Q^{\alpha}_{l,m} = \sum_{\gamma} \Gamma^{\alpha\gamma}_{l,m} Q_{\gamma} \ . \tag{6.14}$$

Substituting (6.14) into (6.13) and comparing it with (6.12), the inverse capacitance matrix can be expressed as

$$C^{-1}_{\gamma\eta} = \sum_{l,m,l',m',\alpha,\beta} G^{\alpha\beta}_{l,m,l,m'} \Gamma^{\alpha\gamma *}_{l,m} \Gamma^{\beta\eta}_{l',m'} \ . \tag{6.15}$$

The induced multipolar charge is found by minimizing the free energy. Separating the monopolar contribution $(l, m = 0)$ in the expression of the free energy, and minimizing the latter with respect to $Q^{\alpha}_{l,m}$, we obtain

$$\mathbf{Q_A} = -\hat{G}^{-1}_{AB} \hat{G}_{B0} \mathbf{Q_0} \ . \tag{6.16}$$

Here $A = l, m$ and $l \neq 0$, correspondingly B, and the equation is written in vectorial and matrix notation. Once this expression is substituted into the free energy, the inverse capacitance can be written in terms of the $\hat{G}$ matrices

$$\hat{C}^{-1} = \hat{G}_{00} - \hat{G}_{0A} \hat{G}^{-1}_{AB} \hat{G}_{B0} \tag{6.17}$$

The order of approximation in this method is the number of the highest multipoles l, l' included. Matrix $\hat{G}_{00}$ has dimension $N_s \times N_s$ with N_s the total number of conductors. Matrices $\hat{G}_{0A}$ and $\hat{G}_{A0}$ are $N_s \times (N_s N_{totalmulti})$ and $(N_s N_{totalmulti}) \times N_s$ respectively, and matrix $\hat{G}_{AB}$ has dimension $(N_s N_{totalmulti}) \times (N_s N_{totalmulti})$. $N_{totalmulti}$ is the maximum number of multipolar terms considered. Formally it is

$$N_{totalmulti} = \sum_{l=1,l_{max}} (2l+1) \tag{6.18}$$

with l_{max} is the order of the maximum multipole included in the approximation. However the symmetries of the problem can help us to reduce it as the $\hat{G}_{AB}$ elements corresponding to certain m_l can be seen to vanish by symmetry. In particular in the case of azimuthal symmetry, considered in the text, only $m = 0$ gives non-zero values and the number of terms included can be reduced to $N_{totalmulti} = l_{max}$. Depending on the geometry of the conductors it can be convenient to use different numbers of l_{max} for different conductors. In particular in the case of an array of small islands sandwiched by two large electrodes, it is better to use a larger number of multipoles at the electrodes.

The expression for $G^{\alpha\beta}_{lm}$ follows from the decomposition of $1/|\mathbf{a} - \mathbf{b} - \mathbf{R}|$, with $\mathbf{a}$, $\mathbf{b}$ and $\mathbf{R}$ three points in space and depends on the geometry of the conductors. For $\alpha \neq \beta$

$$\begin{aligned} G^{\alpha\beta}_{l_1 m_1 l_2 m_2} = & \left[\frac{(l_1 + l_2 - m_1 - m_2)!(l_1 + l_2 - m_1 + m_2)!}{(l_1 + m_1)!(l_1 - m_1)!(l_2 + m_2)!(l_2 - m_2)!}\right]^{1/2} \\ & (-1)^{l_2 + m_2} I_{l_1 + l_2 + m_1 - m_2}(x_\beta - x_\alpha) \end{aligned} \tag{6.19}$$

where $I_{l,m}$ are the irregular solid spherical harmonics

$$I_{lm}(\mathbf{r}) = \frac{1}{r^{l+1}} \sqrt{\frac{4\pi}{2l+1}} Y_{lm}(\Omega) \tag{6.20}$$

The sign of $G^{\alpha\beta}_{l_1m_1l_2m_2}$ depends not only on l_2 and m_2, but also on the order $\alpha\beta$ or $\beta\alpha$ through the dependence of $I_{l_1+l_2+m_1-m_2}(x_\beta - x_\alpha)$.

For the case of a sphere α with radius R_α, $G^{\alpha\alpha}_{l_1,m_1,l_2m_2}$ is given by

$$G^{\alpha\alpha}_{l_1m_1l_2m_2} = \delta_{m_1m_2}\delta_{l_1l_2}\frac{1}{R_\alpha}^{2l_1+1} \tag{6.21}$$

The case of spheres on a row is especially simple. In this case we have azimuthal symmetry what means that all terms involving $m \neq 0$ should vanish. Thus at order l_{max} we have just $N_{totalmulti} = l_{max}$. This allows us to go to reasonably high orders. We can eliminate the indexes m_1, m_2 from the matrix G. Together with the diagonal terms $G^{\alpha\alpha}$ calculated above, and using

$$Y_{l0} = \sqrt{\frac{4\pi}{2l+1}}P_l(cos\theta) \tag{6.22}$$

and $P_l(1) = 1$ and $P_l(-1) = (-1)^l$ the equations are greatly simplified. Thus,

$$\begin{aligned} G^{\alpha\beta}_{l_1,l_2} &= \frac{(l_1+l_2)!}{l_1!l_2!}(-1)^{l_1}\frac{1}{r^{l_1+l_2+1}_{\alpha\beta}}, \text{ if } x_\beta > x_\alpha \\ G^{\alpha\beta}_{l_1,l_2} &= \frac{(l_1+l_2)!}{l_1!l_2!}(-1)^{l_2}\frac{1}{r^{l_1+l_2+1}_{\alpha\beta}}, \text{ if } x_\beta < x_\alpha \end{aligned} \tag{6.23}$$

for $\alpha \neq \beta$. Here $r_{\alpha\beta}$ is the distance between the centers of the spheres α and β. The diagonal of G_{0A} and G_{A0} are zero and $G^{\alpha\beta}_{0A} = G^{\beta\alpha}_{A0}$. Note that

$$G^{\alpha\alpha}_{00} = \frac{1}{R_\alpha} \tag{6.24}$$

and

$$G^{\alpha\beta}_{00} = \frac{1}{r_{\alpha\beta}} \; . \tag{6.25}$$

The zero-order aproximation recovers our expectation for the case of far-apart spheres. As spheres come closer, higher order terms become more and more important. This is reasonable taking into account that the interaction between two multipolar charges $Q^{\alpha}_{l_1 m_1}$ and $Q^{\beta}_{l_2 m_2}$ decays as $r^{l_1+l_2+1}_{\alpha\beta}$. The correction to the inverse capacitance due to the higher order multipoles is given by $-\hat{G}_{0A}\hat{G}^{-1}_{AB}G_{B0}$.

6.3 Methods for Calculating Probability Distributions

When the charges on the array are static, the configuration-averaged probability distribution of the tunneling energies is the same as the time-averaged distributions of the tunneling energies. In this case, the probability distribution can be determined numerically using the following formulas

$$P(\Delta E_i - \delta/2 < \Delta E < \Delta E_i + \delta/2) = p_i/\delta$$

where

$$p_i = \lim_{\sum N_i \to \infty} \frac{N_i}{\sum N_i} .$$

p_i is the probability that a tunneling energy lies within an energy interval $\Delta E = \Delta E_i \pm \delta/2$. N_i is the number of times an energy value falls within this interval. When energy values of arrays are static with respect to time, Eq. 6.3 and Eq. 6.3 can be used to find the probability distributions of energies due to multiple configurations (due to disorder) of arrays with multiple junctions. In this case, $\sum N_i = N_{junc} \times N_{conf}$.

When the charges on the array move, the energies of the junctions vary in time. In this case, we can still use Eq. 6.3 and Eq. 6.3 except that N_i is redefined as:

$$N_i = \sum_{j=1}^{N_{conf}} P_j$$

where

$$P_j = \lim_{\sum t_i \to \infty} \frac{t_i}{\sum t_i} .$$

P_j is the fraction of time that the energies of junctions lies within the energy interval, $\Delta E = \Delta E_i \pm \delta/2$. t_i is the total time that junctions have energy values within the energy interval. When the arrays are stationary, Eq. 6.3 and Eq. 6.3 reduce to the stationary definition of N_i because P_j equals 1 or 0 and N_i is the number of times that the set of energies falls within the interval $\Delta E = \Delta E_i \pm \delta/2$.

Bibliography

[1] A. N. Aleshin, H. J. Lee, S. H. Jhang, H. S. Kim, K. Akagi, and Park Y. W. Coulomb-blockade transport in quasi-one-dimensional polymer nanofibers. *Phys. Rev. B*, 72(15):153202, Oct 2005.

[2] M. G. Ancona, W. Kruppa, R. W. Rendell, A. W. Snow, D. Park, and J. B. Boos. Coulomb blockade in single-layer au nanocluster films. *Phys. Rev. B*, 64(3):033408–1–033408–4, Jun 2001.

[3] C. A. Berven and M. N Wybourne. Effect of self-capacitance on the tunneling thresholds in linear arrays of nanoparticles. *App. Phys. Lett.*, 78(24):3893–3895, Jun 2001.

[4] A. Bezryadin, R. M. Westervelt, and M. Tinkham. Self-assembled chains of graphitized carbon nanoparticles. *App. Phys. Lett.*, 74(18):2699–2701, May 1998.

[5] C. T. Black, C. B. Murray, R. L. Sandstrom, and S. Sun. Spin-dependent tunneling in self-assembled cobalt-nanocrystal superlattices. *Science*, 290:1131–1134, Nov 2000.

[6] N.K. Chaki and K.P. Vijayamohanan. Temperature-induced phase transitions of the ordered superlattice assembly of au nanoclusters. *Jour. of Phys. Chem. B*, 109(7):2552–2558, Feb 2005.

[7] W. Chen, H. Ahmed, and K. Nakazoto. Coulomb blockade at 77 k in nanoscale metallic islands in lateral nanostructure. *App. Phys. Lett.*, 66(24):3383 –3384, 1995.

[8] A. S. Cordan, A. Goltzene, Y. Herve, M. Mejias, C. Vieu, and H Launois. Electron transport in metallic dot arrays: Effect of a broad dispersion in the tunnel junction dimensions. *Journal of App. Phys.*, 84(7):3756–3763, Oct 1998.

[9] A. S. Cordan, Y. Leroy, A. Goltzene, A. Pepin, C. Vieu, and H Launois. Temperature behavior of multiple tunnel junction devices based on disordered dot arrays. *Journal of App. Phys.*, 87(1):345–352, Jan 2000.

[10] P. Delsing. *Single charge tunneling: Coulomb blockade phenomena in nanostructures*, chapter One-dimensional arrays of small tunnel junctions, pages 249 – 274. Plenum Press, 1992.

[11] P. Delsing, T. Claeson, K. K. Likharev, and L. S. Kuzmin. Observation of single-electron-tunneling oscillations. *Phys. Rev. B*, 42(12):7439 – 7449, Oct 1990.

[12] M. H. Devoret and H. Grabert. *Single charge tunneling: Coulomb blockade phenomena in nanostructures*, chapter Introduction to single charge tunneling, pages 1–20. Plenum Press, 1992.

[13] P. A. M. Dirac. The quantum theory of the emission and absorption of radiation. *Proc. of the Roy. Soc. of London A*, 114(767):243 – 265, Mar 1927.

[14] C. Doty. *Electronic transport, self-assembly, and electroluminescence of nanocrystal superlattices.* PhD thesis, The University of Texas of Austin, 2003.

[15] R.C. Doty, H.B. Yu, C.K. Shih, and B.A. Korgel. Temperature-dependent electron transport through silver nanocrystal superlattices. *Jour. of Phys. Chem. B*, 105(35):8291 – 8296, Sep 2001.

[16] A. L Efros. Coulomb gap in disordered systems. *J. Phys. C.*, 8(11):2021 – 2029, 1976.

[17] K. Elteto, E. G. Antonyan, T. T. Nguyen, and H.M. Jaeger. Model for the onset of transport in systems with distributed thresholds for conduction. *Phys. Rev. B*, 71(6):064206–1 – 064206–13, Feb 2005.

[18] K Elteto, X. M. Lin, and H. M. Jaeger. Electronic transport in quasi-one-dimensional arrays of gold nanocrystals. *Phys. Rev. B*, 2005.

[19] Michael M. Fogler, Sergey V. Malinin, and Thomas Nattermann. Coulomb blockade and transport in a chain of one-dimensional quantum dots. *Phys. Rev. Lett.*, 97(9):096601, Sep 2006.

[20] G. Gruner. The dynamics of charge-density waves. *Rev. Mod. Phys.*, 60(4):1129 – 1181, Oct 1988.

[21] A. E. Hanna and M Tinkham. Variation of the coulomb staircase in a two-junction system by fractional electron charges. *Phys. Rev. B*, 44:5919 – 5922, 1991.

[22] G. Y. Hu and R. F. O'Connell. Exact solution for the charge soliton in a one-dimensional array of small tunnel junctions. *Phys. Rev. B*, 1994.

[23] G. L. Ingold and Yu. V. Nazarov. *Single charge tunneling: Coulomb blockade phenomena in nanostructures*, chapter Charge tunneling rates in ultrasmall junctions, pages 21–108. Plenum Press, 1992.

[24] Shantenu Jha and A. Alan Middleton. Effect of disorder on electron transport in arrays of quantum dots. *Los Alamos pre-print archives*, cond-mat/0511094, 2005.

[25] S.D. Jhaveri, D.A. Lowy, E.E. Foos, A.W. Snow, M.G. Ancona, and L.M. Tender. Ion-induced discrete charging of immobilized water-soluble gold nanoclusters. *Chem. Com.*, 14:1544–1545, 2002.

[26] D.M. Kaplan, V. A. Sverdlov, and K.K. Likharev. Coulomb gap, coulomb blockade, and dynamic activation energy in frustrated single-electron arrays. *Phys. Rev. B*, 68(4):045321–1 – 045321–6, Jul 2003.

[27] D.M. Kaplan, V.A. Sverdlov, and K.K. Likharev. Shot noise in frustrated single-electron arrays. *App. Phys. Lett.*, 83(13):2662–2664, Sept 2003.

[28] Takeshi Kawae, Takashi Yasuda, Satoshi Awaji, Kensuke Nakajima, Takeshi Hatano, and Tsutomu Yamashita. Characteristics of charging effect in one-dimensional array of $Bi_2Sr_2CaCu_2O_{8+\delta}$ intrinsic josephson junctions. *Japanese Jour. of App. Phys.*, 44(24):L766 – L769, 2005.

[29] Y. Leroy, A. S. Cordan, and A. Goltzene. Variance analysis of the coulomb blockade parameters in nanometer-size disordered arrays. *Journal of App. Phys.*, 90(2):953–357, Jul 2001.

[30] K. K. Likharev. Correlated discrete transfer of single electrons in ultrasmall tunnel junctions. *IBM J. Res. Develop.*, 32(1):144–158, Jan 1988.

[31] K. K. Likharev. Single-electron devices and their applications. *Proc. of the IEEE*, 87(4):606 – 632, Apr 1999.

[32] K. K. Likharev, N. S. Bakhvalov, G. S. Kazacha, and S. I. Serdyukova. Single-electron tunnel junction array: An electrostatic analog of the josephson transmission line. *IEEE Trans. of Magn.*, 25(2):1436 – 1439, Mar 1989.

[33] K. A. Matsuoka and K. K. Likharev. Shot noise of single-electron tunneling in one-dimensional arrays. *Phys. Rev. B*, 1998.

[34] J. A. Melsen, Ulrik Hanke, H.-0. Muller, and K.-A. Chao. Coulomb blockade thresshold in inhomogeneous one-dimensional arrays of tunnel junctions. *Phys. Rev. B*, 55(16):10638 – 10642, Apr 1997.

[35] A. Alan Middleton and Ned S. Wingreen. Collective transport in arrays of small metallic dots. *Phys. Rev. Lett.*, 71(19):3198 – 3201, Nov 1993.

[36] R. Parthasarathy. *Electronic transport in arrays of gold nanocrystals.* PhD thesis, The University of Chicago, June 2002.

[37] R. Parthasarathy, X. M. Lin, K. Elteto, T.F. Rosenbaum, and H.M. Jaeger. Percolating through networks of random thresholds: Finite temperature electron tunneling in metal nanocrystal arrays. *Phys. Rev. Lett.*, 92(7):076801–1 – 076801–4, Feb 2004.

[38] A. Pepin, C. View, M. Mejias, Y. Jin, F. Carcenac, J. Gierak, L. Couraud, H. Launois, A. S. Cordan, Y. Leroy, and A. Goltzene. Temperature evolution of multiple tunnel junction devices made with disordered two-dimensional arrays of metallic islands. *App. Phys. Lett.*, 74(20):3047 – 3049, May 1999.

[39] Parthasarathy R., X. M. Lin, and H.M Jaeger. Electronic transport in metal nanocrystal arrays: The effect of structural disorder on scaling behavior. *Phys. Rev. Lett.*, 87(18):186807–1 – 186807–4, Oct 2001.

[40] C. Reichhardt and C.J.O. Reichhardt. Temperature and ac effects on charge transport in arrays of metallic dots. *Phys. Rev. B*, 68(16):165305, Oct 2003.

[41] R.W. Rendell, M. G. Ancona, W. Kruppa, E.E. Foos, A.W. Snow, D. Park, and J.B. Boos. Electron transport in nanocluster films with random voids. *IEEE Trans. of Nano.*, 2(2):75 – 81, Jun 2003.

[42] A. J. Rimberg, T. R. Ho, and John Clarke. Scaling behavior in the current-voltage characteristic of one- and two-dimensional arrays of small metallic islands. *Phys. Rev. Lett.*, 74(23):4714–4717, Jun 1995.

[43] F. Ruffino, G. Piro, A. M.and Piccitto, and M. G. Grimaldi. Electronic collective transport in disordered array of c49-phase tisi2 nanocrystals in si. *Journal of App. Phys.*, 101(2):024316–1 – 024316–6, Jan 2007.

[44] J. L. Sample, K. C. Beverly, P. R. Chaudhari, J. R. Heath, and R. D. Levine. Imaging transport disorder in conducting arrays of metallic quantum dots: An experimental and computational study. *Advanced Materials.*, 14(2):124 –127, 2002.

[45] Ping Sheng, B. Abeles, and Y. Arie. Hopping conductivity in granular metals. *Phys. Rev. Lett.*, 31(1):44–47, Jul 1973.

[46] W. R. Smythe. *Static and dynamic electricity.* McGraw-Hill, 1950.

[47] M Stopa. Coulomb staircase and wigner crystalline states in single-electron tunneling through one-dimensional arrays. *Phys. Rev. B*, 64:193315–1–193315–4, Oct 2001.

[48] T. S. Tighe, M. T. Tuominen, J. M. Hergenrother, and M. Tinkham. Measurements of charge soliton motion in two-dimensional arrays of ultrasmall josephson junctions. *Phys. Rev. B*, 47(2):1145–1148, Jan 1993.

[49] S. Wehrli, E. Koch, and M Sigrist. Field doping of C_60 crystals: Polarization and stark splitting. *Phys. Rev. B*, 68:115412, 2003.

[50] C. B. Whan, J. White, and T. P. Orlando. Full capacitance matrix of coupled quantum dot arrays: Static and dynamical effects. *App. Phys. Lett.*, 68:2996 –2998, 1996.

Vita

Janice Adona Trinidad was born on June 19, 1976 in Brooklyn, New York to Eden Adona Trinidad and Andres Jaime Burgos Trinidad. Janice graduated from Mother Seton Regional High School in Clark, New Jersey in May 1994. She graduated suma cum laude ad honorum from Fordham University with a Bachelor of Science degree in physics in May 2000. In August 2000, she began graduate studies in the physics department at the University of Texas at Austin. While conducting research with Dr. Elena Bascones and Dr. Allan Macdonald, she developed a love for communicating science to students of all ages. In May 2007, she earned her high school science certification through the UTeach program and was hired as a science teacher by Steven Zipkes, the principal of Manor New Tech High School.

Permanent Address: 10050 Great Hills Trail Apt. 1605
Austin, TX 78759

This dissertation was typeset with LaTeX 2_ε[3] by the author.

---

[3] LaTeX 2_ε is an extension of LaTeX. LaTeX is a collection of macros for TeX. TeX is a trademark of the American Mathematical Society. The macros used in formatting this dissertation were written by Dinesh Das, Department of Computer Sciences, The University of Texas at Austin, and extended by Bert Kay, James A. Bednar, and Ayman El-Khashab.